NREL/TP-411-7190 • UC Category: 1262 • DE95000215

Research on Stable, High-Efficiency Amorphous Silicon Multijunction Modules

Final Subcontract Report
1 January 1991 – 31 August 1994

S. Guha
United Solar Systems Corporation
Troy, Michigan

NREL technical monitor: W. Luft

National Renewable Energy Laboratory
1617 Cole Boulevard
Golden, Colorado 80401-3393
A national laboratory of the U.S. Department of Energy
Managed by Midwest Research Institute
for the U.S. Department of Energy
under contract No. DE-AC36-83CH10093

Prepared under Subcontract No. ZM-1-19033-2

October 1994

NOTICE

Available to DOE and DOE contractors from:
Office of Scientific and Technical Information (OSTI)
P.O. Box 62
Oak Ridge, TN 37831
Prices available by calling (615) 576-8401

Available to the public from:
National Technical Information Service (NTIS)
U.S. Department of Commerce
5285 Port Royal Road
Springfield, VA 22161
(703) 487-4650

Printed on paper containing at least 50% wastepaper and 10% postconsumer waste

DISCLAIMER

Portions of this document may be illegible electronic image products. Images are produced from the best available original document.

Preface

This Final Subcontract Report covers the work performed by United Solar Systems Corp. for the period 1 January 1991 to 31 August 1994 under DOE/NREL Subcontract Number ZM-1-19033-2. The following personnel participated in the research program.

A. Banerjee, E. Chen, R. Clough, T. Glatfelter, S. Guha (Principal Investigator), G. Hammond, K. Hoffman, M. Hopson, N. Jackett, M. Lycette, J. Noch, T. Palmer, K. Parker, I. Rosenstein, D. Wolf, X. Xu, J. Yang and K. Younan.

The small-angle X-ray scattering experiments reported in Section 3 were carried out at the Colorado School of Mines by D. L. Williamson, S. J. Jones and Y. Chen, and we thank them for this collaborative effort.

We would like to thank V. Trudeau for preparation of this report.

Table of Contents

		Page
Preface		i
Table of Contents		ii
List of Figures		iv
List of Tables		vii
Executive Summary		1
Section 1	**Introduction**	3
Section 2	**Optical Modeling**	4
	Introduction	4
	Modeling and Measurement Tools	4
	Analysis of Textured Substrate Performance	5
	Spectral Response and Reflection of Textured Solar Cells	6
	Calculation versus Measurement	11
	Additional Observations	15
Section 3	**Materials and Cell Research**	13
	Introduction	13
	Microvoids and a-Si Alloy Cell Performance	16
	Microvoids and a-SiGe Alloy Cell Performance	19
	Correlation Between Film Property and Cell Performance	27
	Effect of High Hydrogen Dilution on a-Si Alloy Cells	31
	Effect of High Hydrogen Dilution on a-SiGe Alloy Cells	38
	Thermal Annealing Study	39
	Optimization and Stability of Component Cells in Multijunction Structure	40
	Stability Study on Double-junction Cells	42
	Cell Stability Under Different Light Spectrum and Temperature	45

		Page
Section 4	**Large-area Deposition and Module Research**	**49**
	Introduction	49
	Small-area Component Cells	49
	Tunnel-junction Studies and Multijunction Cells	53
	Uniformity Studies	59
	Module Results	59
	Module Stability	68
	Module Reliability Studies	71
Section 5	**Outdoor Efficiency Measurement**	**72**
Section 6	**Conclusions and Future Directions**	**84**

List of Figures

		Page
1.	Representation of the structure of solar cells fabricated on textured substrates used in this study.	7
2.	Enhancement Factor versus Wavelength of incident light for 3 a-Si:H solar cells. Calculations and experimental data are included on this chart. The representations are described in the text.	8
3.	Enhancement Factor versus Wavelength of incident light for a-Si:H and a-Si:Ge:H solar cells. Calculations and experimental data are included on this chart. The representations are described in the text.	9
4.	Spectral Response versus Wavelength of incident light. The curves labeled Line 5491 and Line 5496 are obtained from measurements. The third curve is due to a calculation using an ideal textured substrate.	10
5.	Spectral response and reflection spectra of solar cells made on specular (labeled "spec") and textured ("tex") silver-coated substrates, with and without ZnO buffer layers.	12
6.	Spectral Response versus Wavelength of incident light for an a-Si:H solar cell. Measured data are represented by the diamond. The 6 curves are calculations using indicated back surface losses.	13
7.	Global Reflection versus Wavelength of incident light for the solar cell of Fig. 5. Measured data are represented by the solid line. The symbols represent calculations using the same back surface losses as in Fig. 5.	14
8.	SAXS data for a-Si alloy films grown at different deposition rates compared to data from a crystalline Si wafer. The intensity has been normalized and corrected for substrate effects according to the procedure in ref. 16. $h=4\pi\sin\theta/\lambda$, where $\lambda=0.154$ nm and 2θ is the scattering angle. The solid lines are drawn to connect the data points.	18
9.	SAXS data from the sample grown at 1.35 nm/sec mounted in two orientations relative to the X-ray beam.	19
10.	Initial and light-degraded efficiencies of a-Si alloy solar cells as a function of deposition rate.	20
11.	Initial solar cell performance and microvoid density as function of germanium content.	25
12.	Fractional degradation of solar cell performance and microvoid density as a function of germanium content.	26

		Page
13.	Initial and light-degraded efficiencies of single-junction solar cells as a function of bandgap of the intrinsic layer.	29
14.	Normalized efficiency versus light-soaking time for the four *p i n* cells.	32
15.	Initial J-V characteristic of a thin *p i n* cell with hydrogen dilution.	33
16.	(a) Quantum efficiency, and (b) the ratio of quantum efficiency in degraded state for the a-Si:H cells deposited at 175 °C.	35
17.	(a) Quantum efficiency, and (b) the ratio of quantum efficiency in degraded state for the a-Si:H cells deposited at 300 °C.	36
18.	Saturation in light-induced degradation of component cells.	41
19.	Spectrum of the metal arc lamp source and global AM1.5 simulator.	46
20.	Degradation of double-junction cells after light soaking under the metal arc lamp and global AM1.5 simulator.	47
21.	Degradation of triple-junction cells after light soaking under metal arc lamp (M) and global AM1.5 simulator (S).	48
22.	J-V characteristics and Q curve of the top component cell of a triple-junction structure.	50
23.	J-V characteristics and Q curve of the middle component cell of a triple-junction structure.	51
24.	J-V characteristics ad Q curve of the bottom component cell of a triple-junction structure.	52
25.	V_{oc} and FF of *n-i-p* and NIPN devices as a function of *p* layer thickness.	54
26.	J-V characteristics of NIPN devices using (a) type A films and (b) type B films.	56
27.	J-V characteristics and Q curve of a double-junction device.	57
28.	J-V characteristics and Q curve of a triple-junction device.	58
29.	V_{oc} contour plot of a triple-junction cell over 1 ft x 1 ft area.	60
30.	FF contour plot of a triple-junction cell over 1 ft x 1 ft area.	61
31.	J_{sc} contour plot of a triple-junction cell over 1 ft x 1 ft area.	62
32.	Efficiency contour plot of a triple-junction cell over 1 ft x 1 ft area.	63
33.	V_{oc} contour plot of a double-junction cell over 1 ft x 1 ft area.	64

		Page
34.	FF contour plot of a double-junction cell over 1 ft x 1 ft area.	65
35.	J_{sc} contour plot of a double-junction cell over 1 ft x 1 ft area.	66
36.	Efficiency contour plot of a double-junction cell over 1 ft x 1 ft area.	67
37.	Initial module efficiency as a function of month and year.	69
38.	Double-junction module efficiency as a function of one-sun exposure time.	70
39.	Progress of outdoor module efficiency versus time. Bars indicate range of efficiencies for several panels.	73
40.	Plot of the ratio of outdoor to indoor module efficiency versus time of year. Squares represent control sample 1, stars control sample 2, and dots individual test modules.	74
41.	Output of a control module evaluated on the United Solar simulator versus time.	75
42.	Comparison of the quantum efficiency of a single a-Si:Ge device (□) used in spectral mismatch calculation to the envelope a double junction device (●).	77
43.	Plot of the ratio of outdoor to indoor module efficiency versus time of year. Solid dots represent as measured, and open dots represent spectral corrected outdoor measurements.	78
44.	Comparison of the measured and curve fit spectral irradiance measured outdoors.	79
45.	Plot of the standard spectrum and the prevailing spectrum taken in April of 1992.	81
46.	Plot of the standard spectrum and the prevailing spectrum taken in December of 1992.	82

List of Tables

		Page
1.	Thickness Measurements using Infrared Interference.	6
2.	Material Properties and Cell Performance for Samples Prepared at Two Different Deposition Rates.	22
3.	Measured Properties for the a-$Si_{1-x}Ge_x$:H Films.	23
4.	Properties of a-SiGe Alloys with Different Ge Content.	28
5.	Performance of Single-junction a-SiGe Alloy solar Cells before and after Light Soaking for 600 Hours under One-sun Illumination at 50 °C.	30
6.	Solar Cell Performance for the Four *p i n* Devices.	32
7.	CPM Data on High and Low Hydrogen Dilution Films.	37
8.	SAXS Data on High and Low Hydrogen Dilution Films	37
9.	Hydrogen Dilution Effect on a-SiGe Cells.	38
10.	Annealing Behavior of Degraded a-Si:H and a-SiGe:H Alloy Solar Cells.	39
11.	Present Status at United Solar of Typical Initial and Degraded Cell Parameters for Component Cells Degraded and Measured under Conditions Described in the Text.	40
12.	Initial and Stabilized Photovoltaic Characteristics of Various Dual-gap, Double-junction Devices.	43
13.	Initial and Stabilized Photovoltaic Characteristics of a Dual-gap, Double-junction 0.25 cm^2 Device with Profiled Bandgap in the Bottom Cell.	44
14.	Characteristics of Double-junction (L5023) and Triple-junction (L6064) a-Si Alloy Solar Cells Both in Original and Degraded States (at 30 and 50 °C, respectively).	45
15.	Summary of Cell Characteristics of the Component Cells of a Triple-junction Structure under AM1.5 Illumination.	53
16.	Summary of Initial Double-junction Module Results as Measured by NREL.	59
17.	Summary of Triple-junction Module Results as Measured by NREL.	68
18.	The J-V Parameters for Two Modules Measured before and after 50 Thermal Cycles and 20 Humidity Freeze Cycles.	71
19.	Effect of Reference Device on Outdoor Efficiency Correction.	80

Executive Summary

Objectives

The principal objective of this program is to conduct research on semiconductor materials and non-semiconductor materials to enhance the performance of multibandgap, multijunction, large-area amorphous silicon-based alloy modules. The goal for this program is to demonstrate stabilized module efficiency of 12% for multijunction modules of area greater than 900 cm^2.

Approach

Double-junction and triple-junction cells are made on Ag/ZnO back reflector deposited on stainless steel substrates. The top cell uses a-Si alloy; a-SiGe alloy is used for the *i* layer in the middle and the bottom cells. After evaporation of antireflection coating, silver grids and bus bars are put on the top surface, and the panel is encapsulated in an ethylene vinyl acetate (EVA)/Tefzel structure to make a one-square-foot monolithic module.

Status/Accomplishments

- Detailed optical modeling studies have been conducted to identify parasitic optical losses in solar cells on textured back reflectors.

- Using a combination of small-angle X-ray scattering and infrared absorption measurements on a-Si alloy films and efficiency measurements on cells, we find that there is a correlation between the microstructure of the films and cell performance. Both the initial and the stabilized performance of solar cells deteriorate when the microvoid density in the films becomes larger. However, no clear correlation is observed for a-SiGe alloy.

- An investigation of film property and cell performance using a-SiGe alloys with different germanium contents shows that there is no good correlation between defect density measured by the constant photocurrent method and cell performance.

- The annealing kinetics of the metastable defects is found to depend on the density of microvoids in the films. With increasing microvoid density, some light-induced defects are created which are harder to be annealed.

- We find that using high hydrogen dilution, a-Si and a-SiGe alloy cells exhibit improved performance in both initial and light-soaked states.

- We have studied the stability of various dual-bandgap, double-junction cells in terms of the bandgaps of the bottom cells and the current mismatch between the component cells. Using a bandgap-profiled bottom cell and optimized current mismatch, we have achieved active-area (0.25 cm^2) efficiency of 11.16% as measured using a single-source simulator after 600 h one-sun 50°C illumination. **This is the highest stabilized small-area efficiency reported for a-Si alloy solar cells.**

- Component cells in a multijunction structure have been optimized to obtain higher stabilized efficiencies under the relevant light spectrum.

- A large number of multibandgap, multijunction modules have been made with aperture area larger than 900 cm^2 showing initial efficiencies higher than 11%. The highest initial efficiency of our modules as measured by NREL is 11.8%. **This is the highest efficiency confirmed by NREL for any thin-film module.** A triple-junction module showed a stabilized efficiency of 10.2% after 1000 h of one-sun light soaking. **This is the highest stabilized efficiency for a one-square-foot a-Si alloy module confirmed by NREL.**

Section 1

Introduction

The research program is directed toward advancing our understanding of amorphous silicon alloys and other relevant non-semiconductor materials for use in large-area multijunction modules. An important thrust of the program is on performance of modules after long-time light exposure; therefore, study of light-induced degradation forms an important part of the program. The goal of this program is to demonstrate a stable, aperture-area efficiency of 12% for a two-terminal, multi-bandgap, multijunction module of aperture area of at least 900 cm^2.

The program is divided into three tasks. Task 1, semiconductor materials research, is directed toward depositing, optimizing and characterizing of suitable amorphous silicon alloy materials and cell structures over 900 cm^2. Task 2, non-semiconductor materials research, involves investigating suitable back reflectors and antireflection coatings and also encapsulants for the modules. Task 3, module research, is directed toward fabricating modules involving grid patterning, cell isolation and interconnect, and encapsulation.

In this report, we outline the progress made toward the program goal in the different task areas. In Section 2, we describe results from our optical modeling work where we analyze the effect of light-trapping on quantum efficiency and short-circuit current density of cells deposited on textured back reflector. Comparing the results of the modeling with experimental data, we show that parasitic optical loss (probably associated with the textured silver/zinc oxide back reflector) limits the gain in short-circuit current density that could be achieved from light trapping. In Section 3, we discuss the results of fundamental studies on materials and cells in which the a-Si intrinsic layers are deposited at different rates. We demonstrate that the microstructure of the material has profound influence on cell efficiency and stability. For a-SiGe:H alloys, on the other hand, no definitive correlation was observed between microvoid density and solar cell performance. We also investigate film properties using constant photocurrent method and do not observe correlation with corresponding solar cell performance for a-SiGe alloys. Hydrogen dilution in the fabrication of a-Si and a-SiGe alloys has been extensively studied. We observe that high hydrogen dilution improves solar cell performance in both the initial state and the light-soaked state. We also investigate the stability of the component cells in a multijunction structure and discuss an optimized cell design using a double-junction structure which gives a stable active area (0.25 cm^2) efficiency of 11.2%. We have also carried out light-soaking experiments for multijunction devices using different light-source spectra at different temperatures. In Section 4, we discuss the status of our large-area deposition work. Significant progress has been made on the performance of component cells which resulted in higher efficiency for double-junction modules and triple-junction modules. **The highest stabilized efficiency for a one-square-foot module is 10.2%. This is the highest stabilized efficiency for a-Si alloy modules as confirmed by NREL.** This section discusses various relevant experiments that have led to this achievement. In Section 5, we discuss outdoor efficiency measurements and point out measurement deficiencies under certain conditions. We find that spectral correction is essential in performing outdoor measurements. Summary of the work and future directions are outlined in Section 6.

Section 2

Optical Modeling

Introduction

Previously, we formulated a method which can characterize the thickness, index of refraction and optical absorption of the individual layers comprising a complete solar cell.[1,2] This procedure is based on coherent optics; therefore it is unable to accurately model solar cells grown on textured substrates. Of course, textured and reflection enhanced substrates are desirable for amplifying the short-circuit current. In this section, we will convey the progress that has been made to optically characterize solar cells fabricated on textured substrates.

The work on specular substrates revealed unexpected parasitic optical absorptions.[2] While these losses were of small consequence for cells grown on flat substrates, it is probable that their influence is greater on light scattering surfaces. In the present effort, we have been able to estimate the effect of parasitic losses for solar cells made on light trapping (i.e., textured) substrates. We have also been able to represent the positive impact that a so-called "perfect" substrate would have in conjunction with our solar cells. These ideas will be presented here. We have also made some preliminary efforts to match measured spectral response and reflection data to calculations, which will also be outlined herein. In addition, certain questions related to the measurements and calculations described in this chapter can be formulated. These represent unknowns and anomalies that will be considered for speculation and future efforts.

Modeling and Measurement Tools

As was true for specular modeling, we would like to use standard solar cell optical measurements to interface calculations to real data. This includes spectral response and reflection spectra. Reflection measurements are more difficult when using scattered light. Thus, we designed and built a large area integrating sphere detector in order to accurately measure the absolute reflection as a function of the wavelength of the incident light. This is coupled to a spectral response system, sharing the monochromator and much of the optical apparatus with it. Measurements of highly diffuse calibration reflection standards reveal that it accurately measures the reflection ±0.5% over each band of the whole measured spectrum range (350 - 950 nm). We have also constructed an apparatus that is capable of measuring reflected light as a function of scattering angle. These measurements are obtained using a He-Ne laser at 633 nm.

There exist two FORTRAN 77 compiled computer programs that were used in this study. The first program was formulated at United Solar and is based on the coherent optics algorithm mentioned above. Its foundation has been described in detail before.[1,2] Briefly, this program uses a simplex optimization routine to adjust the optical constants of individual layers in a solar cell stack in order to iteratively match measured spectral response and reflection spectra. It will be referred to in this report as QFIT. The second computer program was developed at Georgia Tech Research Institute. A description of the principles of this algorithm are also in the literature.[3] In short, it is a Monte Carlo ray tracing program that can numerically simulate the light trapping due to various textures on the top and/or bottom surfaces of a solar cell. It will be referred to in this text as TEXTURE.

Analysis of Textured Substrate Performance

A "figure of merit" that can be used to assess the performance of a light trapping system is the enhancement factor (E.F.). The E.F. is defined as the increase in the effective absorption due to light trapping. It has been shown that when light within a material is randomized, there is a thermodynamic limit for the absorption increase[4] that is

$$\text{E.F. (max.)} = 4 \times n^2, \tag{1}$$

where n is the refractive index. For the case of amorphous silicon based solar cells this number is about 50 in reddish light. For amorphous silicon-germanium alloy solar cells E.F. (max.) is approximately 60. In general, there are two factors that tend to prevent a solar cell designer from obtaining the theoretical limit of Eq. (1): 1) Parasitic optical losses and 2) non-randomized photons. The first item encompasses several causes including, but not necessarily limited to, absorption from the semiconductor dopant layers, absorption in the metal oxide layers (refer to Fig. 1), interface absorption, and, possibly, absorption due to the geometry of the texturing.[5] Lack of light randomization could arise from "imperfect" texturing of the substrate. In our laboratory, we often can measure a specular component in our textured substrates. Also, we have seen coherent structure in the spectra due to light scattering angle.

Figure 2 illustrates some analysis of the light trapping on amorphous silicon based solar cells. This is a plot of calculated and measured E.F. for 3 sets of cells whose intrinsic layer thicknesses were nominally 230, 460, & 920 nm, a 1:2:4 ratio. The curves marked "Actual Cell Data" were obtained in the following manner. Each of the three cells was deposited using identical conditions onto both bare stainless steel and textured substrates. The intrinsic layer thickness differences were obtained by varying the deposition time of the intrinsic layer using the 1:2:4 ratio. The textured substrates consist of stainless steel coated with silver and then subsequently zinc oxide via sputtering. The silver and zinc oxide deposition conditions were adjusted to achieve certain desirable texturing that empirically resulted in maximizing the solar conversion efficiency. The spectral response and reflection versus wavelength of the cells deposited on bare steel were obtained and the cells were modeled using QFIT. Thus, the absorption coefficients of the intrinsic layers were gleaned. The effective absorption coefficients were acquired from the spectral response of cells deposited onto textured substrates. The ratio of these absorption values to the absorption values from the QFIT simulation is the E.F.

TEXTURE calculated enhancement factors for the 3 cells under two separate conditions: 100% back surface reflection and 90% back surface reflection. The textured case was simulated by using pure Lambertian scattering at both the top and bottom surfaces. Incidentally, in other studies we found that either surface may be specular and achieve the same results, which implies that one Lambertian surface is able to completely randomize the light. The absorption values of the intrinsic layer used in this calculation were made to be the same as those calculated with QFIT. The results of these efforts for each of the 3 cells are plotted in Fig. 2. The outcome of Eq. (1) is also plotted in the figure for comparison.

Some tentative observations and conclusions can be made by putting Fig. 2 under scrutiny. A small total parasitic loss in the light trapping system can cause a large drop in the E.F.; Fig. 2 reveals that a 10% optical loss reduces the E.F. about 50%. The E.F. of United Solar's cells are much smaller than the theoretical values. This may indicate that there is considerable scope for improvement. The decrease in the E.F. of the actual data at higher wavelengths is not completely understood. It may be due to the fact that the absorption values obtained from QFIT at long wavelengths is somewhat incorrect. The spectral response at these wavelengths is very small (less than 1%) so that the semiconductor model inside the QFIT engine may not be able to accurately determine the absorption. Also, the reader may have noticed that the 100% texture calculation is lower than $4xn^2$ at the lower wavelength region of Fig. 2. This is

because Eq. (1) is valid when the light is uniformly absorbed, which is not true unless the absorption coefficient is reasonably small.

Figure 3 depicts again some of the curves from Fig. 2 but includes similar data for an amorphous silicon-germanium alloy solar cell. The intrinsic layer of the a-Si:Ge cell has a bandgap of 1.43 eV. The values of E.F. for this cell when compared to an a-Si cell are higher. This is true for both data and calculation. Eq. (1) indicates that the higher E.F. for the germanium case is to be expected. Fig. 3 only includes the 100% reflection case for clarity.

While the portrayal of the E.F. effects reveal much about what is going on optically, the solar cell designer needs to know the "bottom line". What is the effect on Jsc, the short circuit current? Figure 4 illustrates the answer. The silicon-germanium alloy cells from Fig. 3 are depicted here anew. The figure shows the measured spectral response of the cell on bare steel, the cell on the textured substrate, and the TEXTURE calculation of this cell without losses. Integration of these curves with respect to the AM1.5 Global Standard Solar Insolation demonstrates that the gain due to the present substrate is about 5.5 mA/cm^2. The additional gain that is apparently theoretically possible is 4.5 mA/cm^2!

Spectral Response and Reflection of Textured Solar Cells

Effect of Texture and Zinc Oxide

The issue of deposited optical thickness was studied to determine the effect of texture. The role of ZnO as an interface barrier between the a-Si and Ag was also investigated. Banerjee and Guha[6] report the results of earlier work on these and related issues.

Three substrates were prepared, each having a section of specular silver (Ag-sp) and a section textured silver (Ag-tex). One of the substrates was coated with thin ZnO. An identical a-Si:H solar cell was deposited on the ZnO substrate as well as one other (Line #6485 and Line #6499). A solitary intrinsic layer was deposited onto the remaining substrate (Line #6484). The silver texture used in this work was made by slow rate deposition at high temperature in order to achieve a highly textured surface. The degree of specularity using our He-Ne laser method has been determined to be about 20% which is comparable to measurements made on standard BRs.

The measured thicknesses gleaned from infrared interference fringes are detailed in Table 1. This table shows that the texturing reduced the optical thickness by 6-9%.

Table 1. Thickness Measurements using Infrared Interference.

Line 6484 sp	intrinsic layer	550 nm
Line 6484 tex	intrinsic layer	504 nm
Line 6485 sp	solar cell	566 nm
Line 6485 tex	solar cell	535 nm

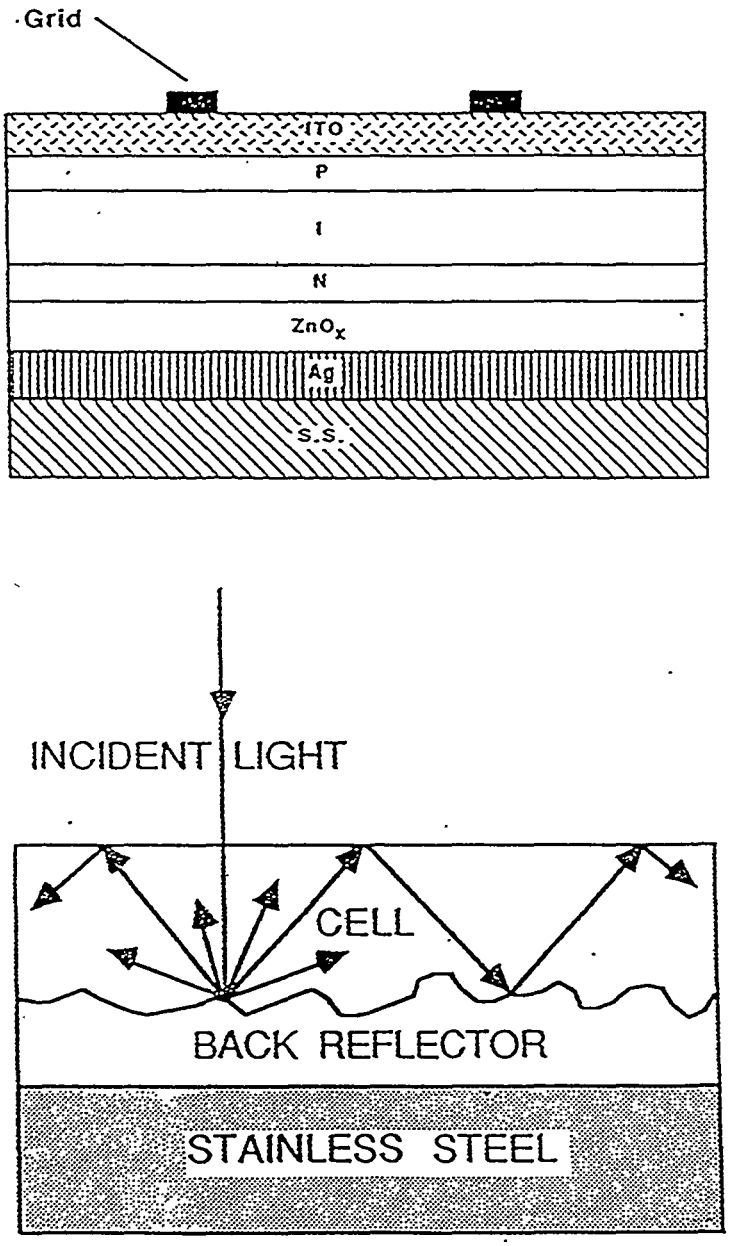

Figure 1. **Representation of the structure of solar cells fabricated on textured substrates used in this study.**

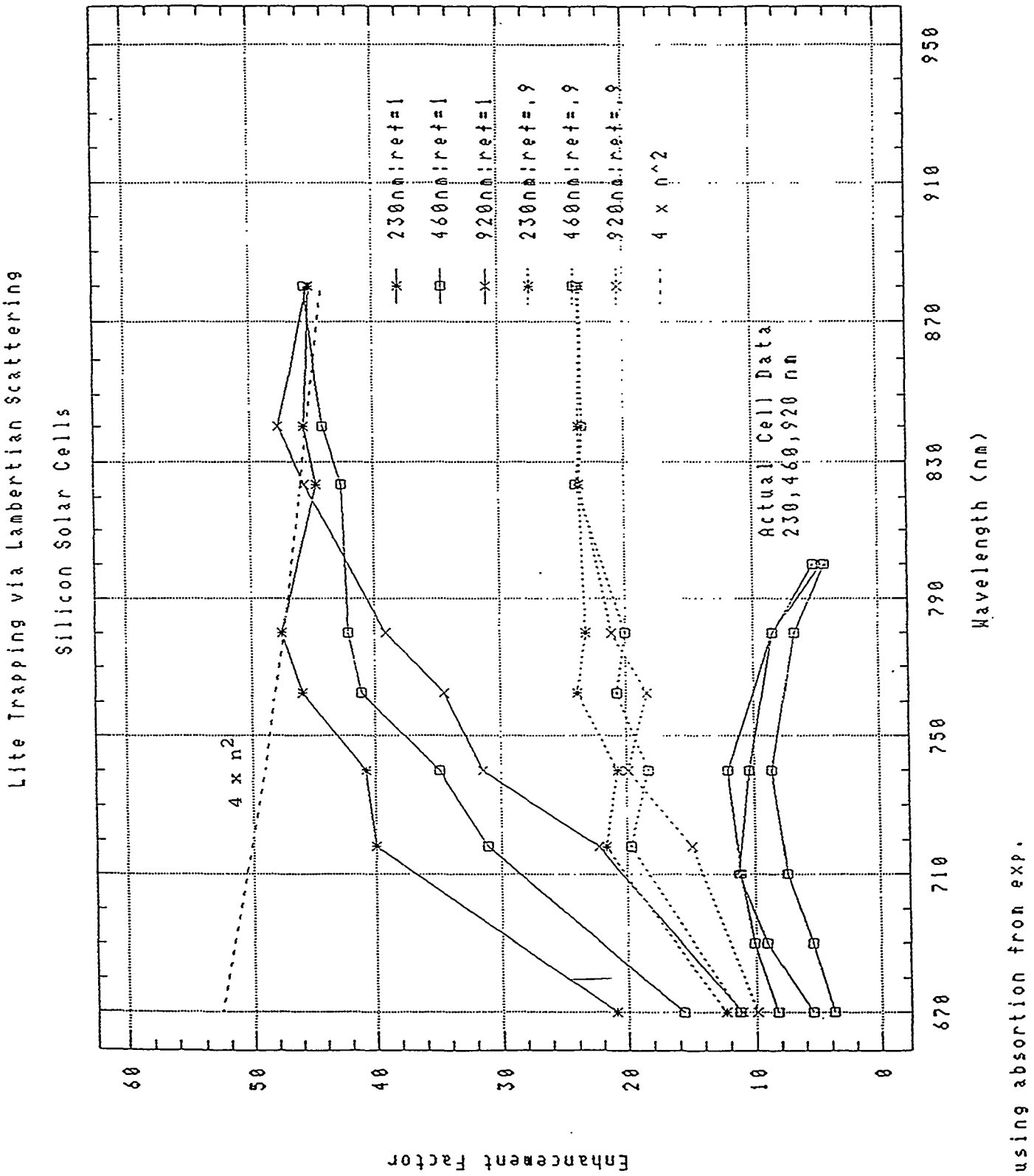

Figure 2. **Enhancement Factor versus Wavelength of incident light for 3 a-Si:H solar cells. Calculations and experimental data are included on this chart. The representations are described in the text.**

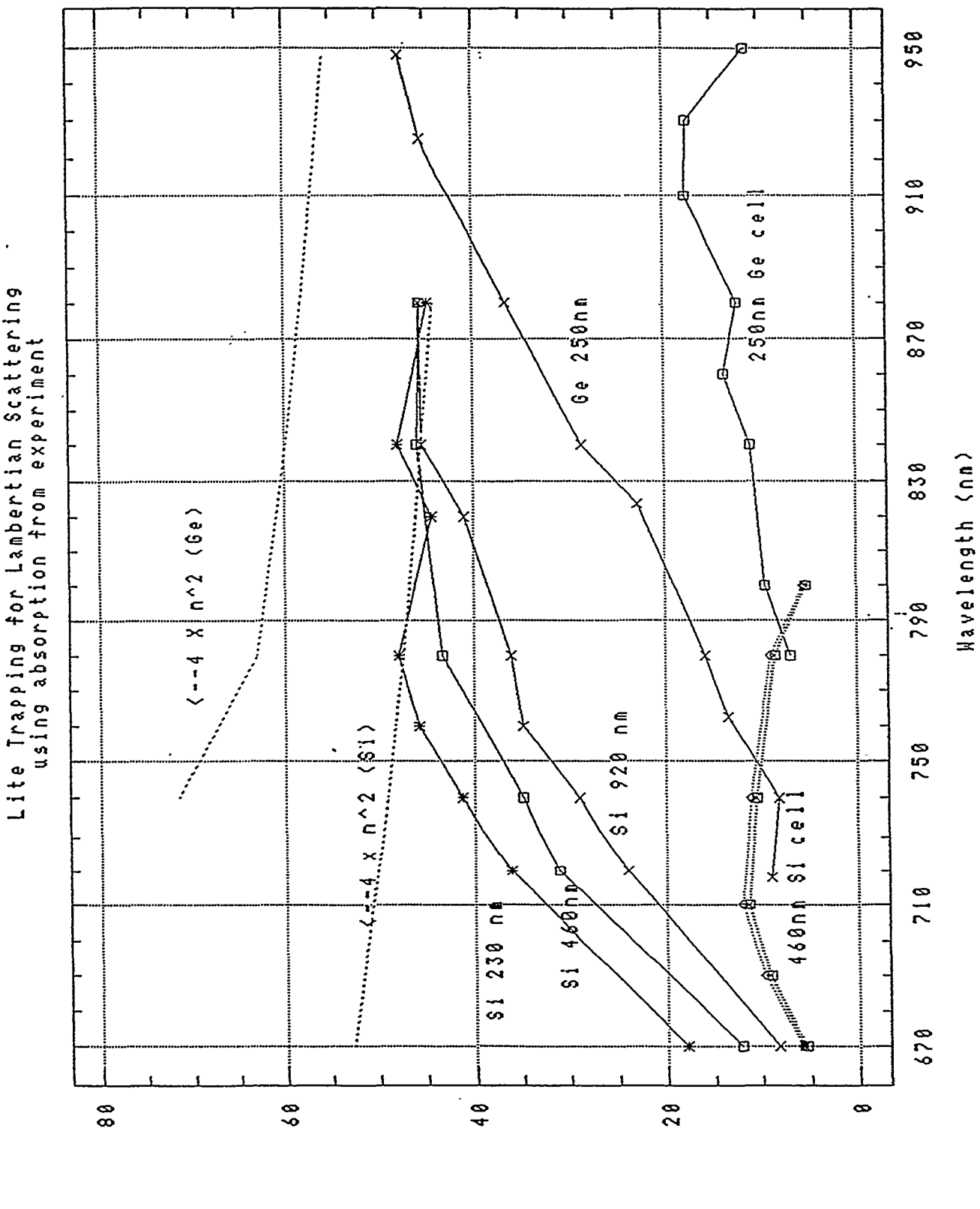

Figure 3. **Enhancement Factor versus Wavelength of incident light for a-Si:H and a-Si:Ge:H solar cells. Calculations and experimental data are included on this chart. The representations are described in the text.**

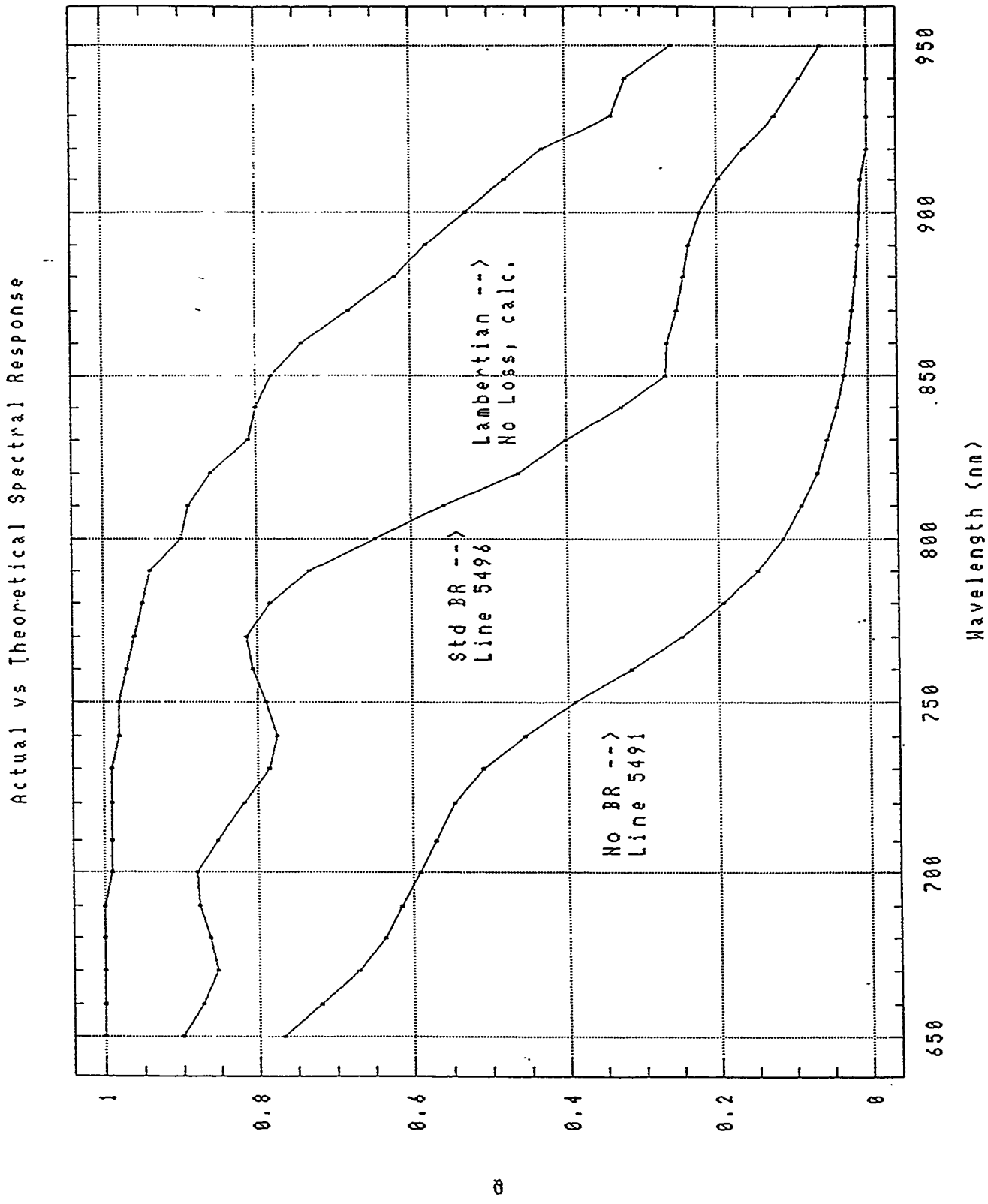

Figure 4. Spectral Response versus Wavelength of incident light. The curves labeled Line 5491 & Line 5496 are measurements. The third curve is due to a calculation using an ideal textured substrate.

Spectral responses and reflection spectra of the solar cells made in this effort were also measured. Fig. 5 represents these measurements. Several conclusions can be obtained from this illustration:

1. Lower values of the red light response were obtained for those samples which did not have ZnO. The red and infrared reflection was also lower without ZnO indicating a parasitic optical loss. Apparently this is due to the a-Si/Ag interface. The ZnO repairs (at least in part) the deleterious optical effect of this interface.

2. The blue response of the textured cells was enhanced due to the fact that the blue reflection was lower for the textured cells. This property was offset for the textured cell with ZnO by a mysterious top surface absorption which was present even though this cell shared its *p* layer and ITO with the other cells shown.

3. The textured cells gave higher quantum efficiency because there was increased red light response. These cells also exhibited lower reflection spectra in the red and, particularly, in the infrared (where there is no spectral response).

4. The best cell (textured with ZnO) was considerably poorer in red response to our silicon solar cells made on standard BR. This signifies that the silver texturing used in this study was not as effective as that of our standard BR, despite the fact that the specularity measurement indicated otherwise.

Calculation versus Measurement

An attempt has been made to calculate both the spectral response and the global reflection for a certain solar cell fabricated on a textured substrate. The only adjustable parameter varied to fit the data was the parasitic optical loss. The specular component of the textured substrate was measured prior to the semiconductor depositions. The measurement was performed with a detector situated normal to a reflected laser spot. The detector subtended a very small area, less than 0.01% of the total hemisphere. The incident light struck the sample about 6° from the perpendicular normal. The resulting value of 20.7% specularity was used in the calculations represented in the discussion following to weight the specular against the textured components of the spectral response and reflection. The thicknesses and optical constants for each layer of the solar cell were obtained using QFIT from an identical cell deposited on bare stainless steel. QFIT was then used to recalculate the spectral response and reflection spectra of this cell while inserting silver and zinc oxide layers into the modeled optical stack (as in Fig. 1). The optical constants for the silver were obtained previously from ellipsometry. The indices of refraction for the zinc oxide came from ellipsometry also, but the extinction coefficient was artificially inserted to correspond to certain back surface parasitic losses. During the recalculation, the thickness of the intrinsic layer was adjusted so that the calculated maxima and minima in the reflection spectra matched the measured maxima and minima of the textured solar cell. This had the effect of adjusting the deposition thickness of the flat case to correspond to the textured case. In this instance, it was found that the intrinsic layer is optically 20% thinner when deposited on this particular textured substrate than when it was deposited on the flat stainless steel substrate. When these adjustments were completed, the result represents the specular component of the modeled solar cell.

The textured component of the spectral response and reflection for this solar cell under consideration was made using TEXTURE. The intrinsic layer optical constants were obtained from QFIT as described above. TEXTURE repeated these calculations for several back surface parasitic losses, corresponding to the losses used for the specular situation. Finally, the specular component of both the reflection and spectral response were weighted at 20.7%, while the textured elements were weighted at 79.3%. The weightings correspond to the measured specularity of the base substrate. The resulting spectral response curves for these calculations are plotted in Fig. 6 with the actual measured data. Similarly, the reflection calculations and data are represented in Fig. 7.

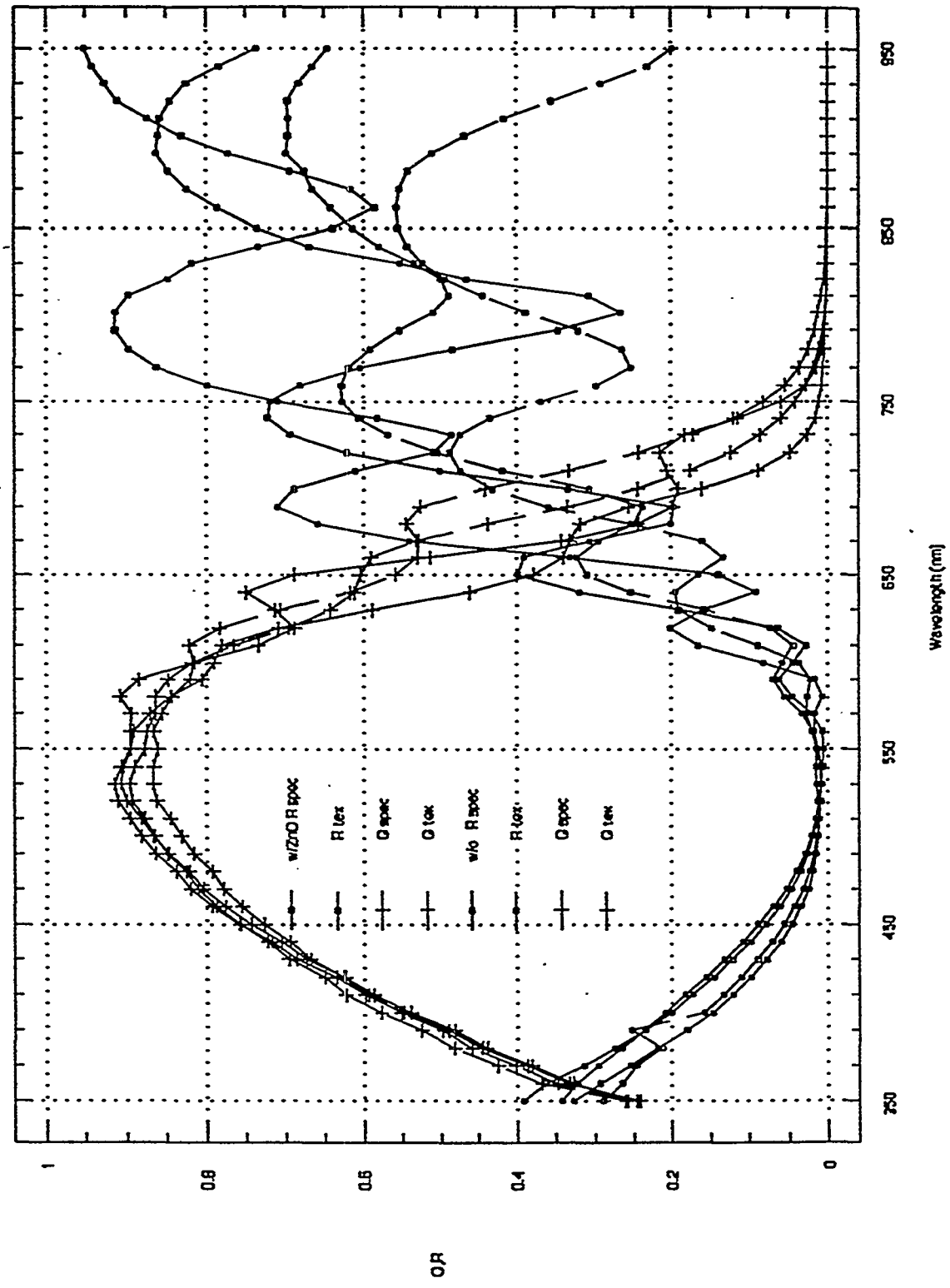

Figure 5. Spectral response and reflection spectra of solar cells made on specular (labeled "spec") and textured ("tex") silver-coated substrates, with and without ZnO buffer layers.

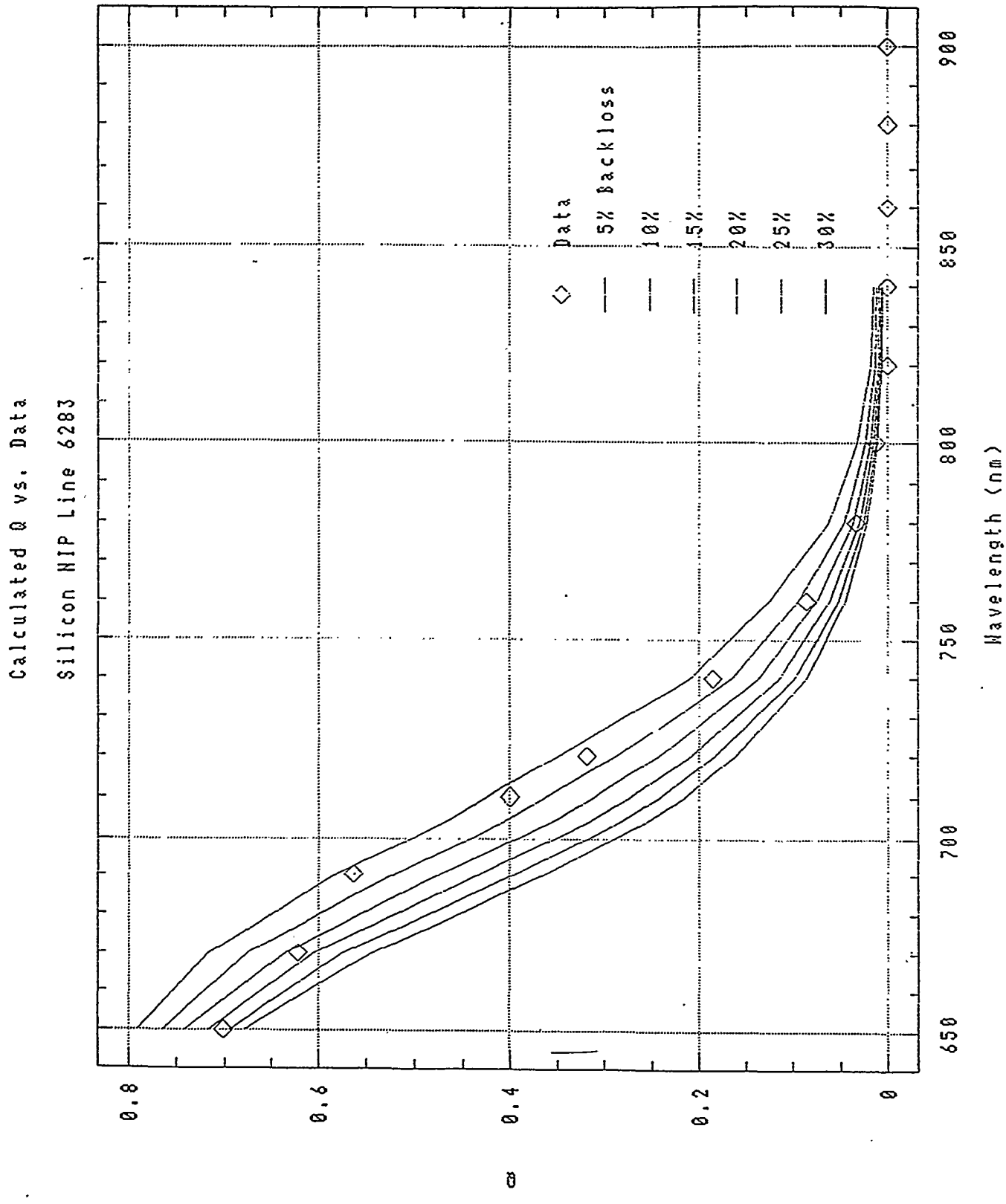

Figure 6. Spectral Response versus Wavelength of incident light for an a-Si:H solar cell. Measured data is represented by the diamond. The 6 curves are calculations using indicated back surface losses.

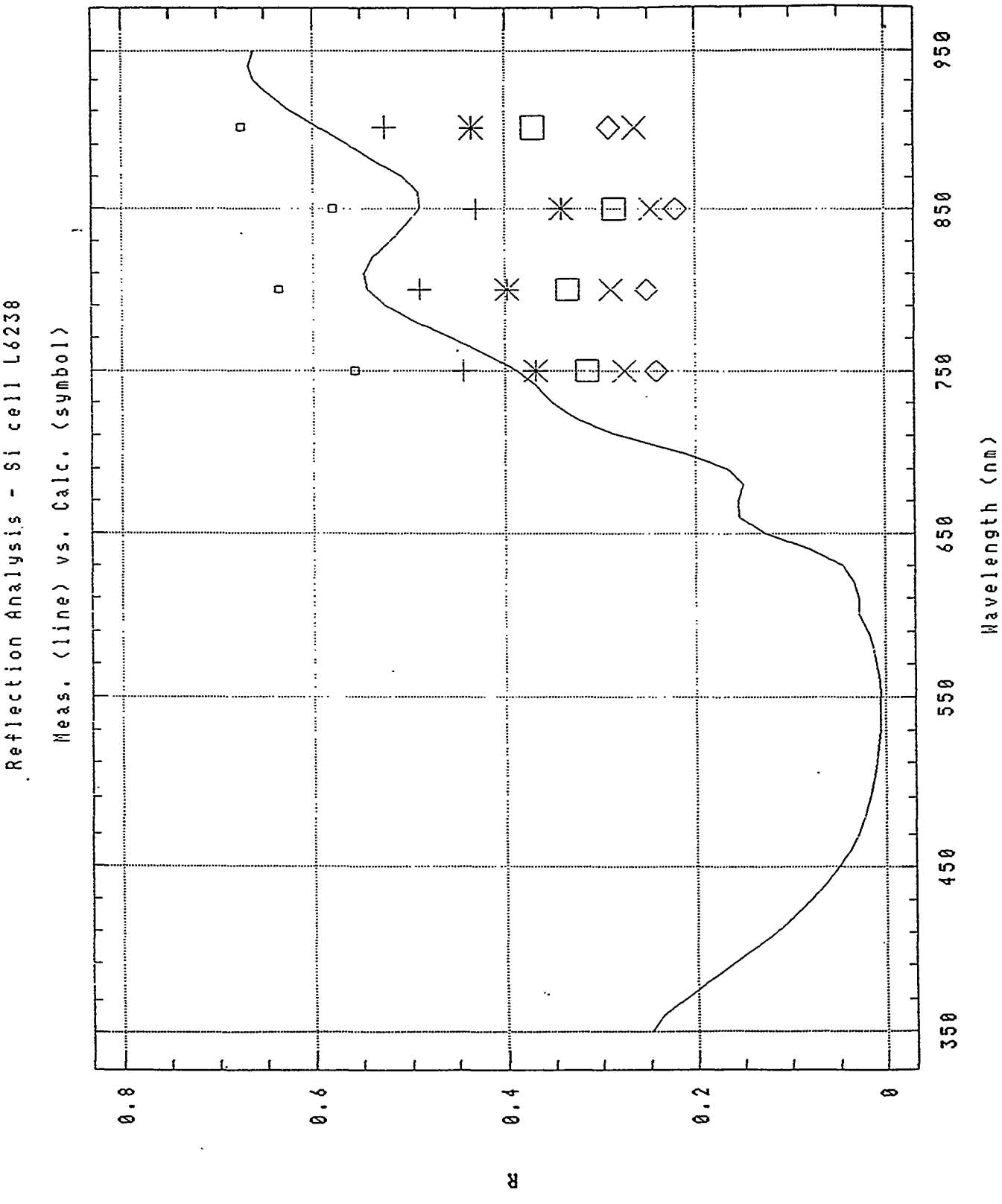

Figure 7. **Global Reflection versus Wavelength of incident light for the solar cell of Fig. 5. Measured data is represented by the solid line. The symbols represent calculations using the same back surface losses as in Fig. 5.**

Both Figs. 6 and 7 indicate a good fit with a parasitic absorption of about 10%. The structure in the spectral response data of Fig. 6, presumably due to coherence, was not emulated in the calculations. This suggests that a significant portion of the scattered light is coherent. Measurement of the reflection versus scattering angle for this substrate does, in fact, have structure at angles less than 30^0. On the other hand, the structure of the reflection revealed in Fig. 7 seems to be modeled well. Unfortunately, this modeling attempt does not clearly answer the question of whether or not this light trapping technology can be simulated using geometric optics.

Additional Observations

Reflection measurements of solar cells on textured substrates have raised some problematic issues. This is particularly so in view of the fact that our laboratory's global reflection measurement apparatus has been improved. For example, the textured substrates typically have reflection values of only 90%, despite the fact that the silver base has been measured repeatedly to be about 98% and the metal oxide is found to have very little absorption. Another example, the sum of the spectral response and reflection (and the reflection in the near infra-red) is about 70% at best. Where is the missing light? A substrate was made as part of this effort that had a specular component of 0% and a measured reflection of about 90%, but the resulting solar cells had inferior spectral responses. This appears anomalous when compared to some of the other evidence. The testimony of the work reported in this section seems to point towards the possibility that a large amount of light is lost due to parasitic optical absorption. However, many attempts at isolating such losses have not born fruit. We plan to continue these efforts until a thorough understanding of the light trapping system is realized and the consequential improvement in solar cell performance is realized.

Section 3

Material and Cell Research

Introduction

In this section, we present results on research conducted on materials and cells. In order to obtain a basic understanding of the origin of as-grown and light-induced defects in a-Si alloy films and cells, we have investigated correlation between microstructure of the material and cell performance where the microstructure was altered by changing the deposition rate of the intrinsic layer. We find a correlation in that both the initial and the stabilized performance of solar cells deteriorate when the microvoid density in the films becomes larger. However, no clear correlation is observed for a-SiGe alloys.

We have also studied the effect of high hydrogen dilution on a-Si and a-SiGe alloy cells and found that cells fabricated using high hydrogen dilution give rise to better performance. Optimization of component cells have led to a stabilized double-junction cell efficiency of greater than 11%.

Light-soaking experiments have been conducted for multijunction cells under a metal arc lamp and a global AM1.5 source. Although the spectra of the two sources are quite different, we find the degradation of the cells to be quite similar. The effect of light-soaking temperature will also be discussed

Microvoids and a-Si Alloy Cell Performance

Light-induced degradation of hydrogenated amorphous silicon (a-Si:H) alloy materials and devices has been the subject of intensive studies.[7] It is generally agreed that recombination of excess electron-hole pairs generated by illumination creates metastable defects in the bulk of the material.[8] The defect states reduce the mobility-lifetime product of electrons and holes and causes degradation of solar cell performance. The origin of the metastability is not quite understood, and the list of causes includes[9] hydrogen, impurities like C, O, or N, microvoids due to inhomogeneous growth, weak bonds or a combination of these.

Using small-angle X-ray scattering (SAXS) measurement, it has been demonstrated[10,11] that even in the best quality material, microvoids of typical diameter 1.0 nm exist, occupying a volume fraction of about 1%. The void density is typically larger for poorer quality material.[12] In order to correlate the microvoid density in the material with the initial and light-degraded performance of solar cells, we have fabricated single-junction *p i n* solar cells in which the intrinsic layer has different microvoid density caused by changes in the deposition rate. The results are given in this report.

Single-junction *p i n* solar cells were grown by the rf glow-discharge technique on stainless steel substrates kept at 300 °C. Details of deposition parameters are given elsewhere.[13] The intrinsic layer was grown using a disilane-hydrogen mixture, and the dilution of the mixture and rf power density were changed to obtain deposition rates between 0.14 and 1.35 nm/sec. The thicknesses of the *i* layers were kept constant at ~ 420 nm. The deposition conditions for the doped layers were kept the same for all the samples. The top contact was made using thermally evaporated indium tin oxide (ITO). Cell performance was measured under global AM1.5, red, and blue illumination.

Samples consisting of only the *i* layer, typically 1 μm thick, were deposited separately on crystalline silicon wafers for infrared (IR) measurements and on thin, iron-free, high-purity Al foils for SAXS measurements. The deposition conditions were nominally identical to those used to produce solar cells. Details of the SAXS experimental methods have been discussed elsewhere.[14]

Figure 8 shows the SAXS data for three samples prepared with different deposition rates where the natural log of the normalized scattering intensity[14] is plotted versus the magnitude of the scattering vector h and compared to the SAXS signal from a 70 μm crystalline Si wafer (polished on both sides). There is a clear systematic increase in the SAXS signal with increasing deposition rate. Above about 2 nm^{-1} the SAXS intensity is essentially angle independent for the 0.14 and 0.62 nm/sec deposition rates, and we believe this is due primarily to Laue monotonic scattering[15] by the Si-H alloy matrix which should increase with increasing H content. This accounts for most of the difference between the crystalline Si and the two lower deposition rate a-Si:H films above h=2 nm^{-1}. The film grown with the highest rate clearly shows angular dependence in the SAXS up to the largest angles. After correcting for the angle-independent contribution for all three samples, we estimate the volume fraction of voids (V_f) assuming a simple two-phase system (voids and matrix) as described in detail elsewhere.[12,14] We find similar values of V_f of 1 ± 0.5% for the samples prepared with 0.14 and 0.62 nm/sec deposition rates and 4 ± 1% for the one deposited with the 1.35 nm/sec rate.

In order to explore the shape and orientation characteristics of the voids, the sample with the largest void-fraction was measured at a tilt angle of 45°, and the results are compared to the non-tilted data in Fig. 9. The data are identical within experimental error, and this demonstrates that the voids are of spherical shape or, if non-spherical, randomly oriented throughout the sample.[12]

The sample with the large void fraction was also analyzed to extract the approximate void size distribution by fitting a superposition of SAXS curves due to a few distinct spherical microvoid diameters and adjusting the sizes and volume fractions to give a good fit. We estimate that about 80% of the void volume is due to diameters of 0.9 nm with most of the remainder less than 10 nm in diameter. The very small voids account for most of the increase in V_f compared to the two films prepared at the lower deposition rates.

The initial and light-degraded (after 600 h one-sun, 50 °C, open-circuit condition illumination) performances of the solar cells as a function of *i* layer deposition rate are shown in Fig. 10. The initial efficiency is found to decrease above deposition rates of ~ 0.35 nm/sec. The light-degraded efficiency shows a systematic, continuous decrease as the deposition rate is increased. It is interesting to note that at a deposition rate of 0.14 nm/sec, the relative degradation is only 12.5% whereas at 1.35 nm/sec, the relative degradation is 43%. We should mention that since the samples are deposited on stainless steel, both the initial and final efficiencies are lower than those on an optimized back reflector. A reference cell of the same thickness deposited on Ag/ZnO back reflector at a deposition rate of 0.14 nm/sec has an initial efficiency of 11% and degrades by about 30% under the same light-soaking condition. Since photon absorption is enhanced with a back reflector, the generation rate of carriers is larger, and this results in a higher degradation.

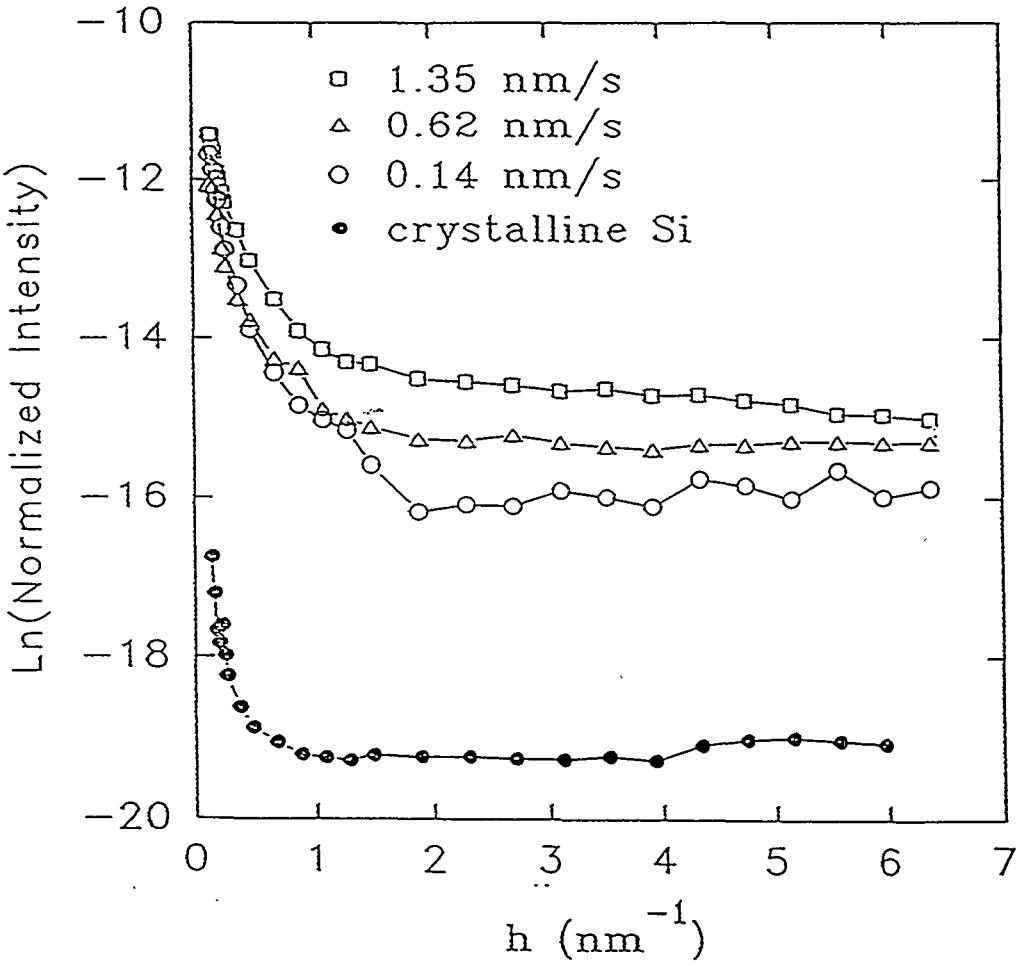

Figure 8. **SAXS data for a-Si alloy films grown at different deposition rates compared to data from a crystalline Si wafer. The intensity has been normalized and corrected for substrate effects according to the procedure in ref. 16. $h=4\pi\sin\theta/\lambda$, where $\lambda=0.154$ nm and 2θ is the scattering angle. The solid lines are drawn to connect the data points.**

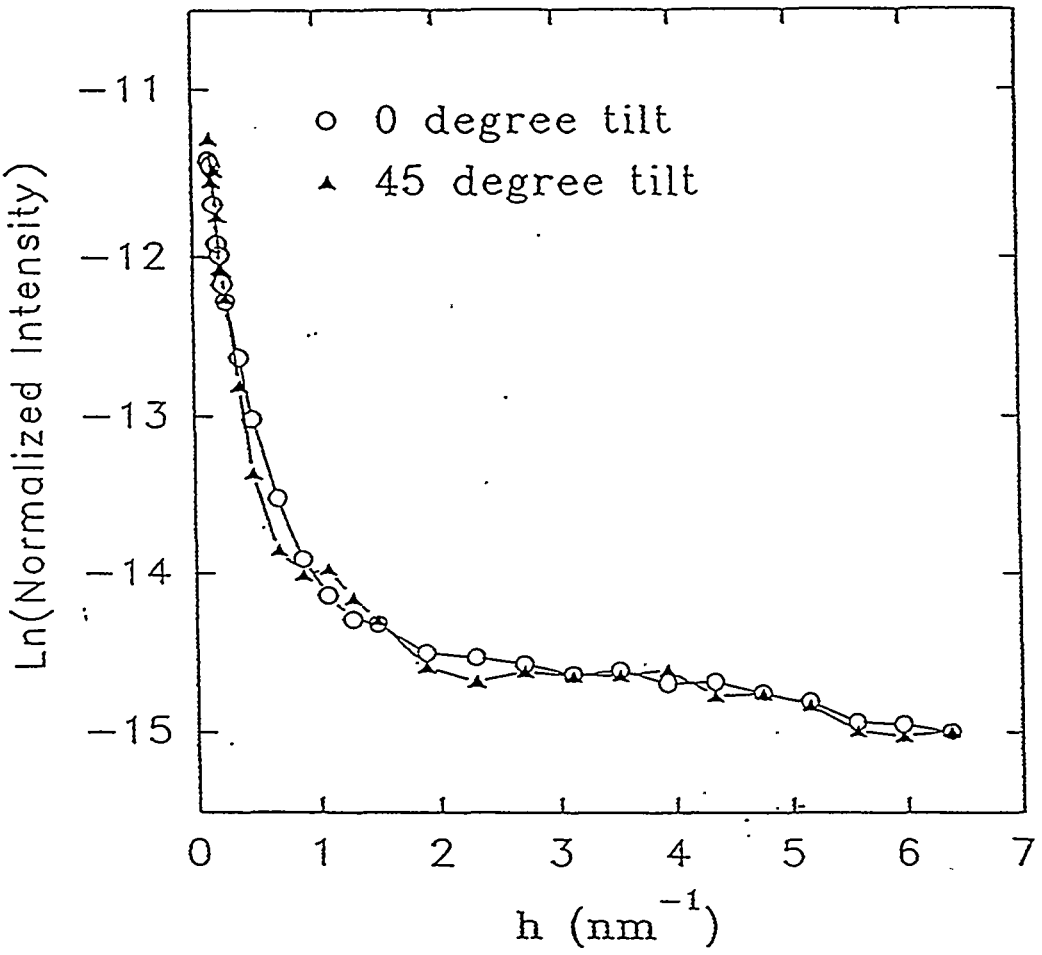

Figure 9. **SAXS data from the sample grown at 1.35 nm/sec mounted in two orientations relative to the X-ray beam.**

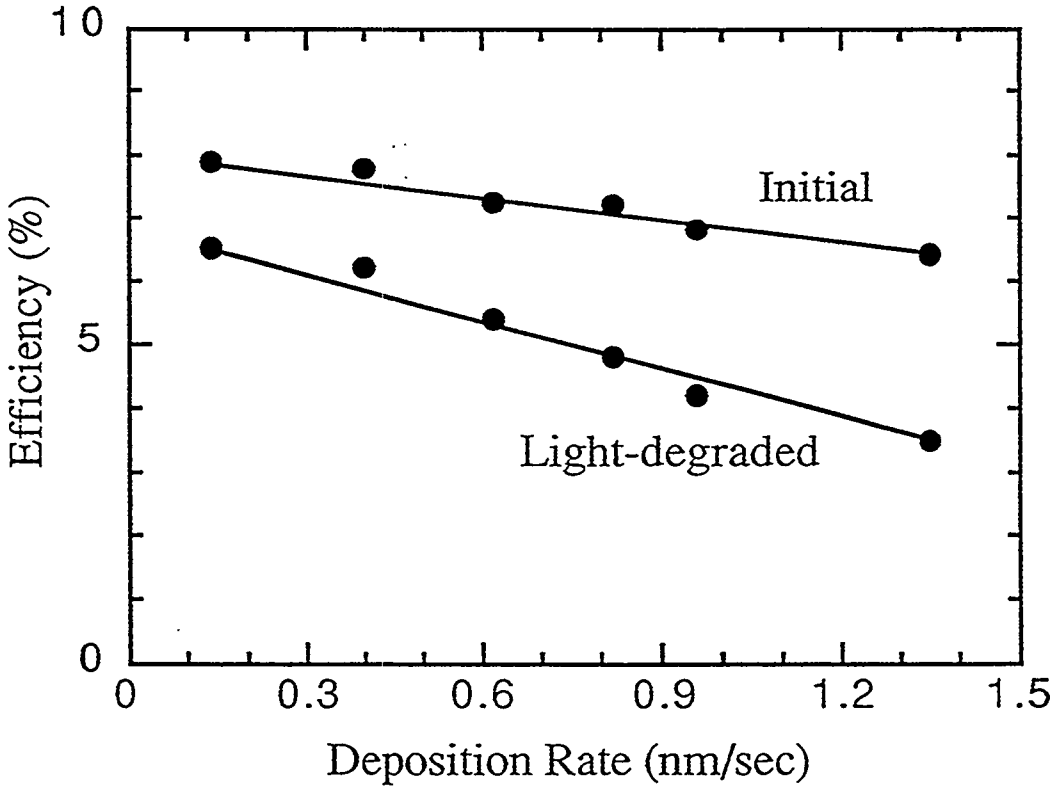

Figure 10. **Initial and light-degraded efficiencies of a-Si alloy solar cells as a function of deposition rate.**

Since increasing deposition rate leads to higher void density, the results indicate an enhancement in degradation of solar cells with the *i* layers having more microstructure. This is consistent with earlier results[16] which showed an increase in light-induced sub-bandgap absorption in films that showed more microstructure as determined by the ratio of infrared absorption at wave numbers 2070 cm^{-1} and 2000 cm^{-1}. For our films deposited at 0.14 nm/sec, the hydrogen content is 8% whereas that for the deposition rate of 1.35 nm/sec is 12%. The ratio of the microstructure fraction, R, as defined by $R = I_H(2070)/[I_H(2000) + I_H(2070)]$ increases from 8.4% to 18.4% in these two films. $I_H(2000)$ and $I_H(2070)$ are the integrated infrared absorption due to the stretching mode bonds at 2000 cm^{-1} and 2070 cm^{-1}, respectively.[17] It should be pointed out that although R increases from 8.4% to 18.4% as the deposition rate is raised from 0.14 nm/sec to 1.35 nm/sec, C_H (2000), which is the concentration of hydrogen bonded in the Si-H monohydride mode at 2000 cm^{-1}, remains constant at around 6.4%. This suggests that, at least in these films, the degradation process is not associated with the isolated Si-H bonds in the dense amorphous matrix. It also suggests that the increased angle-independent SAXS contribution with increasing deposition rate (proposed above to be the Laue monotonic scattering from increased H in the a-Si:H matrix) is not due to increased numbers of isolated Si-H bonds but rather to bonds associated with the 2070 cm^{-1} mode.

Our results, showing increased light-degradation in materials with larger void-fraction and microstructure fraction, do not support the suggestion by Matsuda et al.[18] that material with increased microstructure may be more stable. Their conclusion was based on photoconductivity measurements on materials deposited from Xe-diluted silane mixtures. The dangling bond density, both in the initial and light-degraded state, was, however, found to be higher for films with poorer microstructure. As we shall discuss below, this is in agreement with our solar cell results.

We should mention that our results show a decrease both in the initial and degraded performance of the solar cells with increase in the density of microvoids whereas the results of Bhattacharya and Mahan[16] showed no change in the initial quality of the film as determined by sub-bandgap absorption even when R was as high as 50%. The sensitivity in measurement of solar cell efficiency, of course, is much better than that in defect density estimation from sub-bandgap absorption. The deterioration of the material quality as a function of increased microstructure is evident from Table 2 where we have tabulated results from both microstructure and solar cell measurements for samples prepared at a deposition rate of 0.14 nm/sec and 1.35 nm/sec. The fill factor under red and blue illumination is determined by the collection length of the photo-generated carriers which, in turn, is governed by the defect density. A clear correlation between both initial and light-degraded defect density and void density is apparent. Since dangling bonds are the predominant defect centers in a-Si:H films, these results are in agreement with those reported in Ref. 18. We would like to point out that although we see a correlation between deposition rate and void density, these results should be considered only to depict the trend under certain deposition parameters. With different gas mixtures or at a different substrate temperature, it may be possible to get a lower void density even at a higher deposition rate.

In conclusion, by a combination of IR and SAXS measurements on films and efficiency measurements of solar cells, we see a correlation between microstructure and solar cell performance. With increasing microvoid density and microstructure fraction, both the initial and light-degraded solar cell performance are found to deteriorate.

Table 2. Material Properties and Cell Performance for Samples Prepared at Two Different Deposition Rates.

Deposition rate	0.14 nm/sec	1.35 nm/sec
Void fraction	1%	4%
Predominant void diameter	-	0.9 nm
Hydrogen content	8%	12%
Microstructure fraction (R)	8.4%	18.4%
C_H (2000)	6.4%	6.3%
Initial efficiency	7.85%	6.31%
Degraded efficiency	6.53%	3.5%
Initial red fill factor	0.67	0.52
Degraded red fill factor	0.52	0.43
Initial blue fill factor	0.73	0.67
Degraded blue fill factor	0.67	0.40

Microvoids and a-SiGe Alloy Cell Performance

We have previously observed[19] a correlation between microvoids and cell performance in a-Si alloys. It has been recently reported[20] that there is a sharp increase in the microvoid density of a-SiGe alloys as the Ge content increases beyond 20%. In order to determine if the observed poorer quality of a-SiGe alloys is related to this poorer microstructure, we have prepared a systematic set of samples of various Ge contents for studies and solar cell characterization.[21]

Details of SAXS measurements and interpretation have been reported earlier.[14] In Table 3, we show the properties of a-SiGe alloy films with different Ge content (X) and optical gap (E_0) prepared at different substrate temperatures (T_s). Q_0 is a measure of the microvoid density as obtained from the SAXS data.[19] Q_{45} is the corresponding value with the sample tilted 45° with respect to the incident beam.

A significant increase in SAXS is seen as the Ge content increases beyond 20%. Below 20%, the Q_0 values are comparable to those for device-quality a-Si alloy. From measurements made with samples tilted with respect to the incident beam, the increase in scattering beyond 20% Ge content is attributed to the appearance of elongated low density regions in the film, modeled as ellipsoidal microvoids, which may be related to columnar growth. From Table 3, we also find that for the high Ge content samples, SAXS increases as the substrate temperature increases from 350 to 400 °C. This is contrary to what one observes in a-Si alloys.

Table 3. Measured Properties for the a-$Si_{1-x}Ge_x$:H Films.

Sample	X	E_o (eV)	T_s (°C)	Q_0 (10^{-6} nm^{-2})	Q_0/Q_{45}	Laue Monotonic Intensity (10^{-7} nm^{-2})	Film Density (g/cc)	Density Deficiency (%)
4810	0	1.72	300	1.0	-	1.0	-	-
5525	0.09	-	350	1.3	1.0	2.6	2.54	3.4
5526	0.09	-	250	0.4	0.9	2.8	2.61	0.7
4838	0.19	1.55	350	1.1	1.1	3.2	2.98	-0.7
4835	0.31	1.50	350	2.4	1.3	5.2	3.26	2.7
4837	0.41	1.41	350	5.9	2.5	4.6	3.50	4.4
5445	0.44	-	400	9.2	5.3	3.7	3.60	4.0

In Figs. 11 and 12, we show the initial and light-degraded properties of the a-SiGe:H solar cells with different germanium contents. Included for comparison are the values of Q_0 from the SAXS. In an attempt to compare films with similar bonded hydrogen contents, we include in the figures only values for films prepared at substrate temperatures of 350 °C except for the a-Si:H film which was deposited at 300 °C. Several points emerge. There is a decrease in V_{oc} and a corresponding increase in J_{sc} as the germanium content increases. This is expected since the optical gap decreases with increasing Ge content. All of the initial photovoltaic parameters shown appear to change smoothly with X with no indication of a sharp change above X = 0.2 where the Q_0 values rise significantly. This indicates that other changes are taking place in the material when Ge is added which are not detected by SAXS. It has been demonstrated that addition of Ge increases the width of the conduction band tail, presumably caused by alloy disorder.[22] This would, of course, not be detected by SAXS. Increase of isolated dangling bond density caused by introduction of germanium would cause a reduction in fill factor but will not be detected by SAXS. Moreover, since the sensitivity in the SAXS measurement for the film thickness used here (~ 1 μm) is on the order of $\pm$ 0.5 x 10^{-6} nm^{-2} and the magnitude of SAXS signal measured for the X = 0.19 sample is only 1.1 x 10^{-6} nm^{-2}, we cannot rule out a systematic decrease in SAXS as the Ge content is lowered below X = 0.2, which cannot be detected with the sensitivity realized in these measurements.

The lack of any definite enhanced deteriorations in the initial photovoltaic properties when the SAXS increases dramatically at X around 0.3-0.4 suggests that, for at least this set of films, the role of the SAXS detected microstructure is perhaps relatively minor. If the columnar-like microstructure detected by SAXS does not affect the initial solar cell properties, two points of interest can be made. First, it has been shown that a sharp decrease in the photoconductivity-to-dark conductivity ratio and increase in the sub-bandgap absorption detected by photothermal deflection spectroscopy accompany the sudden increase in Q_0 at around X = 0.2-0.3,[17] suggesting that the appearance of columnar-like microstructure can alter the photoelectronic properties. This result would seem to contradict the lack of correlation of Q_0 with the a-SiGe:H solar cell properties. However, the photoconductivity measurements were done with the electrodes in the co-planar configuration, in contrast to the solar cell sandwich design. One could envision that in the solar cell a majority of the conduction of electrons and holes takes place in the high density, less defective column regions without the carriers passing through the low density regions which comprise a relatively small volume fraction of the material. In contrast, for the carriers to reach the co-planar electrodes, they must move parallel to the film surface and likely pass through low density material lying between the columns. Second, while no definite correlations can be made between the SAXS and the solar cell properties for a-SiGe:H, a clear dependence of the initial solar cell efficiency on the SAXS-detected microstructure in a-Si:H was noted.[19] But the nature of the scatterers in these two cases is quite different. In contrast to anisotropic, columnar-like microstructure in the alloys, the scatters detected in the a-Si:H with the poor cell properties were spherical and/or randomly oriented and smaller (~ 1 nm) than those which appear in the alloys. Therefore, the effect of microstructure on the solar cell properties may depend on details such as void size, shape and orientation.

Finally, note that the fractional degradation characteristics shown in Fig. 12 suggest larger amounts of degradation for X $\geq$ 0.2 (except V_{oc}), and this may correlate with the SAXS-detected microstructure. However, more data is needed before a definite conclusion can be reached, and detailed discussion is warranted.

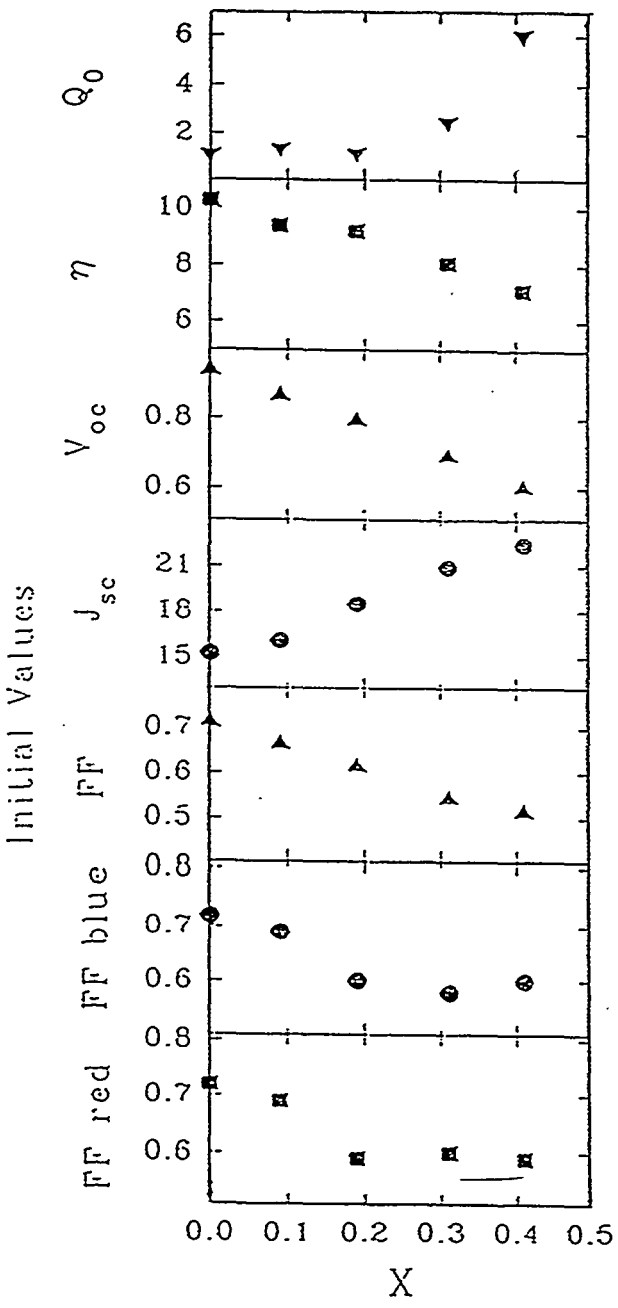

Figure 11. **Initial solar cell performance and microvoid density as function of germanium content.**

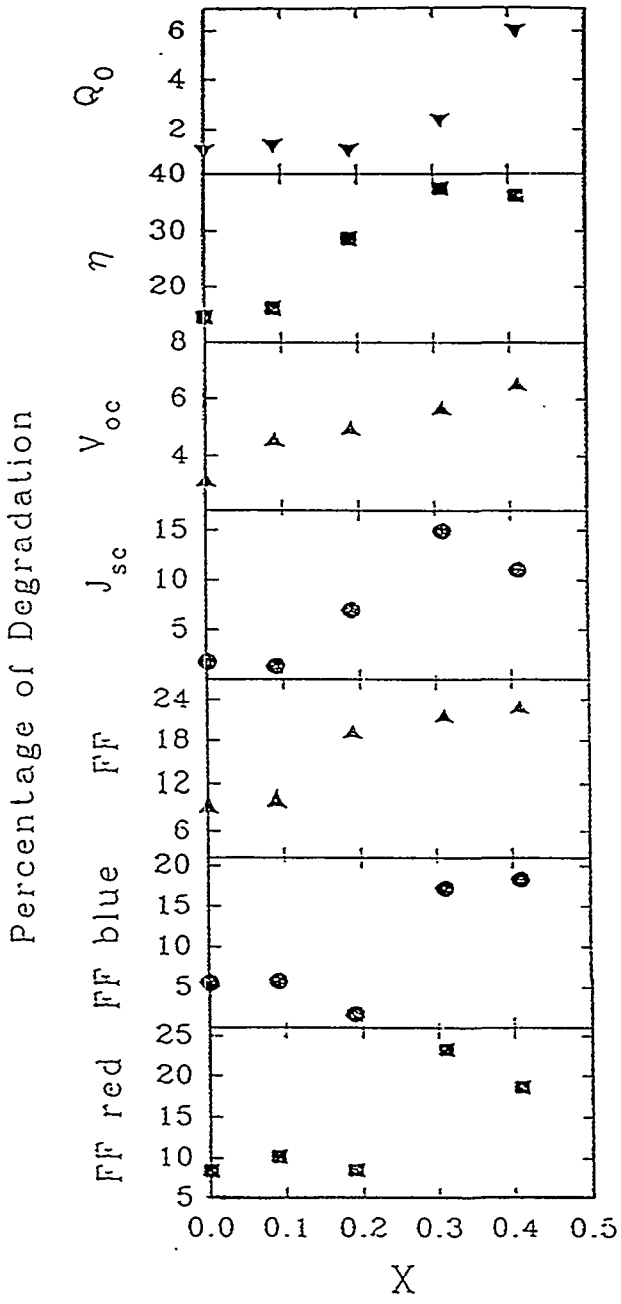

Figure 12. **Fractional degradation as a result of light soaking of solar cell performance and microvoid density as a function of germanium content.**

Correlation Between Film Property and Cell Performance

It is generally agreed that the degradation in efficiency of solar cells is predominantly caused by deterioration of the material quality. A great deal of effort, therefore, has been made to investigate material properties before and after light-induced degradation to obtain the best material for optimized solar cell performance.

The most commonly used techniques to evaluate material properties are the measurement of photoconductivity and sub-bandgap absorption. Using uniformly absorbing monochromatic light to measure the photocurrent, one can obtain the majority carrier $\mu\tau$ product in the material. Measurement of sub-bandgap absorption by photothermal deflection spectroscopy (PDS) or by constant photocurrent method (CPM) gives information about the valence band tail and the near mid-gap deep states. Integration of the sub-bandgap absorption can be correlated to the spin density in the material[23] and has been used to predict solar cell performance.[24]

The applicability of the use of defect density obtained from CPM to predict the solar cell performance, however, merits careful scrutiny. It is widely recognized[25] that the accuracy of the defect density obtained from sub-bandgap absorption measurement depends critically on several factors such as the precision of matching the sub-bandgap CPM or PDS data to absorption values measured at higher than bandgap energy and also on the accuracy of determining the slope of Urbach edge. An uncertainty of a factor of 2 to 3 in the estimated value is easily expected. A change in the defect density by a factor of 2, however, will substantially affect the solar cell performance.

In order to determine the degree of correlation that exists between material properties and solar cell performance, we have studied the material properties of a-SiGe alloy films and also the performance of cells with the intrinsic layers deposited under nominally identical conditions. The results are reported in this report.

a-SiGe alloy films, typically 1 μm thick, were deposited on crystalline silicon wafer and 7059 glass substrates from a dilute mixture of disilane and germane.[26] The germane flow was varied to obtain films with three different bandgaps. Single-junction *p i n* solar cells were made on stainless steel with predeposited textured Ag/ZnO back reflector. The intrinsic layers of the cells, typically 300 nm thick, were grown under conditions nominally identical to those for the films deposited on glass.

The films on glass substrates were characterized by measurement of dark and photoconductivity, above-bandgap optical absorption and reflection and sub-bandgap absorption by photothermal deflection spectroscopy and constant photocurrent method. Infrared absorption measurement was used to determine the hydrogen content of the films deposited on silicon wafers. The solar cell performance was measured under global AM1.5 illumination and also under red and blue illumination. In Table 4 we show the properties of three films with different germanium contents. The mobility-lifetime ($\mu\tau$) product for electrons is measured with 750 nm light of an incident flux of 5×10^{14} cm^{-2} sec^{-1}. The Urbach edge (E_u) was obtained from PDS measurement, and the defect density is calculated from integrated sub-bandgap absorption below the Urbach edge as measured by CPM. We notice that the Urbach edge remains constant with increasing Ge-content; the $\mu\tau$ product, however, decreases with increasing Ge-content. The defect density for the three samples is in the range from 3.1 to $5.6 \times 10^{15}/cm^3$. Also shown in Table 4 are the properties after one-sun light soaking at 50 °C for 600 h. The $\mu\tau$-products decrease for all the three samples as a result of the light soaking. The defect density increases by about a factor of 2 for the films with lesser Ge-content. For the film with 41% Ge, however, the defect density remains essentially unchanged from the as-deposited condition.

Table 4. Properties of a-SiGe Alloys with Different Ge Content.

Sample	Ge-Content (%)	Optical Gap (eV)	Eu (meV)	$\mu\tau$ ($cm^2V^{-1}S^{-1}$)		Defect Density (cm^{-3})	
				Init.	Degraded	Init.	Degraded
4827	19	1.55	51	$8x10^{-7}$	$2.7x10^{-7}$	$5.1x10^{15}$	$1.2x10^{16}$
4830	30	1.50	52	$3x10^{-7}$	$1.5x10^{-7}$	$3.1x10^{15}$	$6.6x10^{15}$
4829	41	1.41	49	$1x10^{-7}$	$4.0x10^{-8}$	$5.6x10^{15}$	$6.5x10^{15}$

In Fig. 13 we show the initial and light-degraded efficiencies of cells where the *i*-layers are about 3000 Å thick and have been grown under nominally identical conditions to those for the films shown in Table 4. All the cells show typical light-induced degradation between 30% to 40%. In Table 5, we tabulate the performance of the cells under global AM1.5, blue and red illumination. We notice that the maximum degradation is in the fill factor of the cells. For the cell with the largest bandgap, the blue fill factor remains unchanged, whereas the red fill factor degrades by a small amount. For the cells with lower bandgap, both the red and the blue fill factors show larger degradation. The fill factor of a solar cell is essentially governed by the ease with which the photogenerated carriers can be collected at the electrodes. For the highly absorbing blue photons, the fill factor is determined by the electron transport, whereas for the more uniformly absorbing red photons, the carrier with the poorer transport property will determine the fill factor. For example,[19] in high quality a-Si alloy single-junction cells, the blue fill factor is much better than the red fill factor because the $\mu\tau$ product for electrons is much higher than that for the holes. It is interesting to note that for all the three a-SiGe alloy cells shown in Table 5, the red and the blue fill factors are very similar in the undegraded state even though the $\mu\tau$ product for electrons drops down drastically with increasing Ge-content. What is more interesting is the fact that even though the defect density as measured by CPM hardly changes after light soaking in the lowest bandgap alloy, the corresponding cell shows a large degradation in both the red and the blue fill factors. We should also point out the lack of correlation between the $\mu\tau$ value and the defect density in the a-SiGe alloys. This is partly due to the fact that even if the defect density remains the same, with increasing Ge-content, the electron mobility decreases, which would cause the $\mu\tau$ product to be lower.[22] It is interesting, however, that for the lowest bandgap alloy, even though the $\mu\tau$ product degrades after light soaking, the defect density does not change much. The dark conductivity of the sample is about the same in the degraded and the annealed states, and a shift in the Fermi level cannot explain this anomaly. As we have pointed out earlier, there can easily be an error by a factor of 2 in the estimate of defect density of different samples. On the same sample, however, the accuracy is much better. There must be, therefore, other changes taking place after light soaking which affect the solar cell performance, but cannot be detected by CPM. New states may be created above the Fermi level; the capture cross-section of the light-induced states also could be different. CPM would be insensitive to these changes.

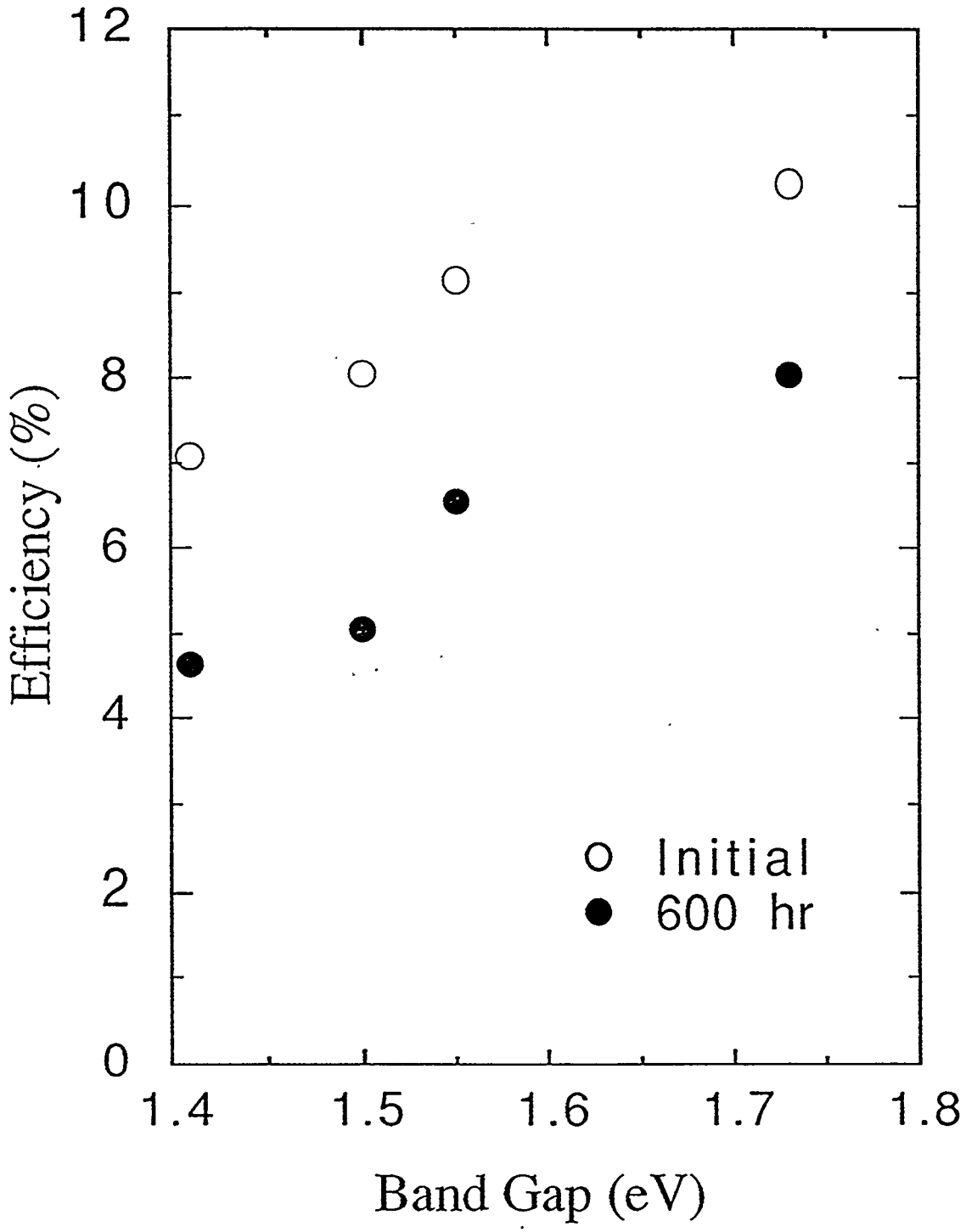

Figure 13. **Initial and light-degraded efficiencies of single-junction solar cells as a function of bandgap of the intrinsic layer.**

Table 5. Performance of Single-junction a-SiGe Alloy Solar Cells before and after Light Soaking for 600 Hours under One-sun Illumination at 50 °C.

i-layer Bandgap	State	AM1.5 Performance J_{sc} (mA/cm^2)	V_{oc} (V)	FF	η (%)	Fill Factor Blue	Red
1.55 eV	Initial	18.50	0.80	0.62	9.18	0.60	0.59
	Degraded	17.21	0.76	0.50	6.54	0.59	0.54
1.50 eV	Initial	20.93	0.70	0.55	8.06	0.58	0.60
	Degraded	17.81	0.66	0.43	5.05	0.48	0.46
1.41 eV	Initial	22.39	0.61	0.52	7.10	0.60	0.59
	Degraded	19.92	0.57	0.40	4.54	0.49	0.48

We would like to emphasize that the observed lack of correlation does not imply that measurement of film property cannot give general ideas about the solar cell performance. If the $\mu\tau$ product is very low or the defect density very high, the solar cell will also perform poorly. However, with the current accuracy of CPM measurements, it is not possible to distinguish between high-quality materials where the defect densities differ by a factor of 2 or less. Moreover, as discussed earlier, factors other than the density of deep states also affect solar cell performance.

In conclusion, we have studied the performance of a-SiGe alloy single-junction solar cells both before and after light soaking. The intrinsic layers of the cells have different Ge-contents. a-SiGe alloy films were grown on glass with parameters nominally identical to those for the cells, and the film properties were measured. We do not find good correlation between cell performance and film properties for these high-quality materials.

Effect of High Hydrogen Dilution on a-Si Alloy Cells

Hydrogen dilution is known[27,28] to improve the material quality of a-Si:H by controlling the growth kinetics. Guha et al.[29] observed that films grown using 10% silane (SiH_4) and 90% hydrogen (H_2) exhibited improved stability against prolonged light exposure when compared with films grown using 100% SiH_4. With increasing hydrogen coverage, it is believed that the impinging species take a longer time to be incorporated in the film, which should lead to a denser material with less defects. We have used a wide dilution range of SiH_4-H_2 and Si_2H_6-H_2 mixtures, and the results from the latter mixture are reported here.

Films were grown on 7059 glass and crystalline silicon for constant photocurrent measurement (CPM) and infrared spectroscopy (IR). Single-junction *p i n* devices were deposited onto stainless steel substrates without a back reflector for solar cell characterization. We used two Si_2H_6/H_2 ratios and two deposition temperatures. We shall report the solar cell results first.

Table 6 lists J-V characteristics of four *p i n* devices measured under AM1.5 illumination. These devices have similar intrinsic layer thicknesses of ~500 nm. It is interesting to note that for a given temperature, cells with higher hydrogen dilution exhibit lower short-circuit current density (J_{sc}), but higher open-circuit voltage (V_{oc}), and fill factor (FF). In addition, the difference in V_{oc} and FF becomes larger at 175 °C. Since FF is indicative of carrier transport properties and reflects the quality of the intrinsic layer, we see that devices made with higher hydrogen dilution possess better quality. To understand the difference in V_{oc}, we calculated the optical bandgap by measuring the quantum efficiency and reflection of the solar cells and employing an optical model.[1] We found that for a given temperature, cells with higher H_2 dilution exhibit higher optical bandgap. The calculated values are listed in Table 6. Since these samples have similar intrinsic layer thicknesses, the higher V_{oc} and lower J_{sc} for higher dilution can be explained by the difference in the bandgap.

To study the degradation behavior of the cells, we used a metal-arc lamp with its intensity adjusted to one-sun. The cells were kept at open circuit and the temperature maintained at 50 °C. Figure 14 plots the normalized efficiency versus light-soaking time for the four cells. It is observed that the difference in degradation is not very large for high temperature samples, while the low temperature ones displayed substantial difference. In fact, the low-dilution, low-temperature sample showed a severe degradation of more than 40%. The degraded J-V characteristics and the percentage of degradation are also given in Table 6.

It is interesting to note that for a given temperature, cells made with high dilution exhibit not only higher initial FF and V_{oc} but also higher stabilized values. Furthermore, the percentage of degradation is also less for high dilution cells. The higher stabilized FF certainly is a good indication of higher quality material. Moreover, as we have reported[30] previously, the drop in V_{oc} is associated primarily with the bulk property rather than any interfacial effect. Therefore, from solar cell results, one may conclude that high H_2 dilution gives rise to better cell performance. In fact, we have made thin *p i n* cells with J_{sc} ~7 mA/cm^2 which exhibit initial V_{oc} of 1.023 volts and FF of 0.77, suitable for the top cell in a high-efficiency triple-junction structure.[31] The initial J-V characteristic of the cell is shown in Fig. 15. After 1500 hours of one-sun light soaking at 50 °C, the cells maintain a V_{oc} of 0.98 volt and a FF of 0.71.

Table 6. Solar Cell Performance for the Four *p i n* Devices.

Description	J_{sc} (mA/cm^2)	V_{oc} (volts)	FF	P_{max} (mW/cm^2)	Eg (eV)
L6100					
Initial (300 °C Low Dilution)	12.3	0.94	0.65	7.5	1.72
Degraded	11.6	0.91	0.55	5.8	
Degradation (%)	5.7	3.2	15.4	22.7	
L6192					
Initial (300 °C High Dilution)	11.6	0.96	0.68	7.6	1.74
Degraded	11.2	0.94	0.61	6.4	
Degradation (%)	3.5	2.1	11.3	15.8	
L6156					
Initial (175 °C Low Dilution)	11.4	0.96	0.64	7.0	1.77
Degraded	9.5	0.91	0.46	4.0	
Degradation (%)	16.7	5.2	28.1	42.9	
L6186					
Initial (175 °C High Dilution)	10.9	1.00	0.69	7.5	1.79
Degraded	10.5	0.97	0.60	6.1	
Degradation (%)	3.7	3.0	13.0	18.7	

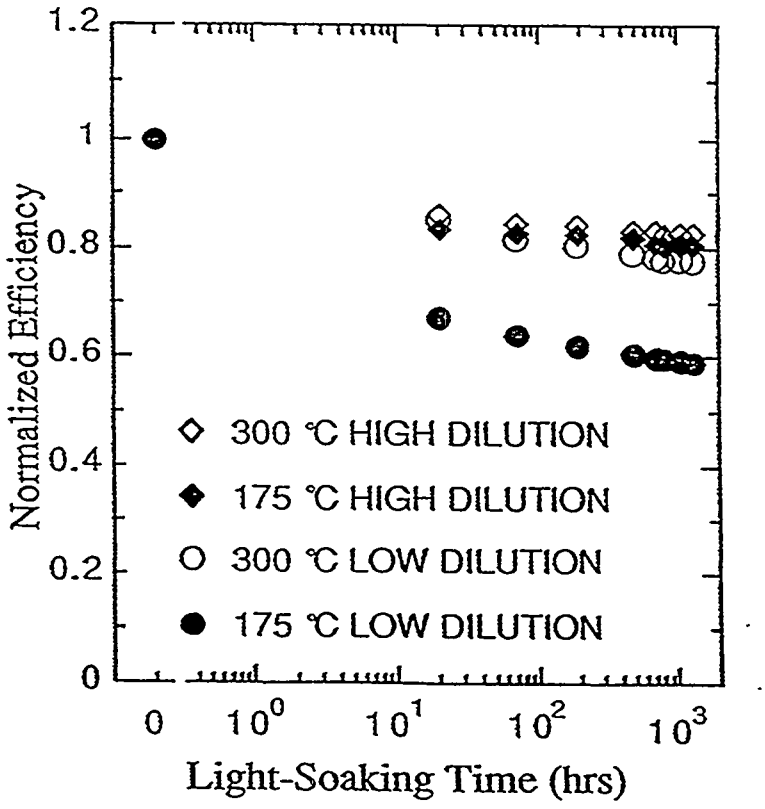

Figure 14. Normalized efficiency versus light-soaking time for the four *p i n* cells.

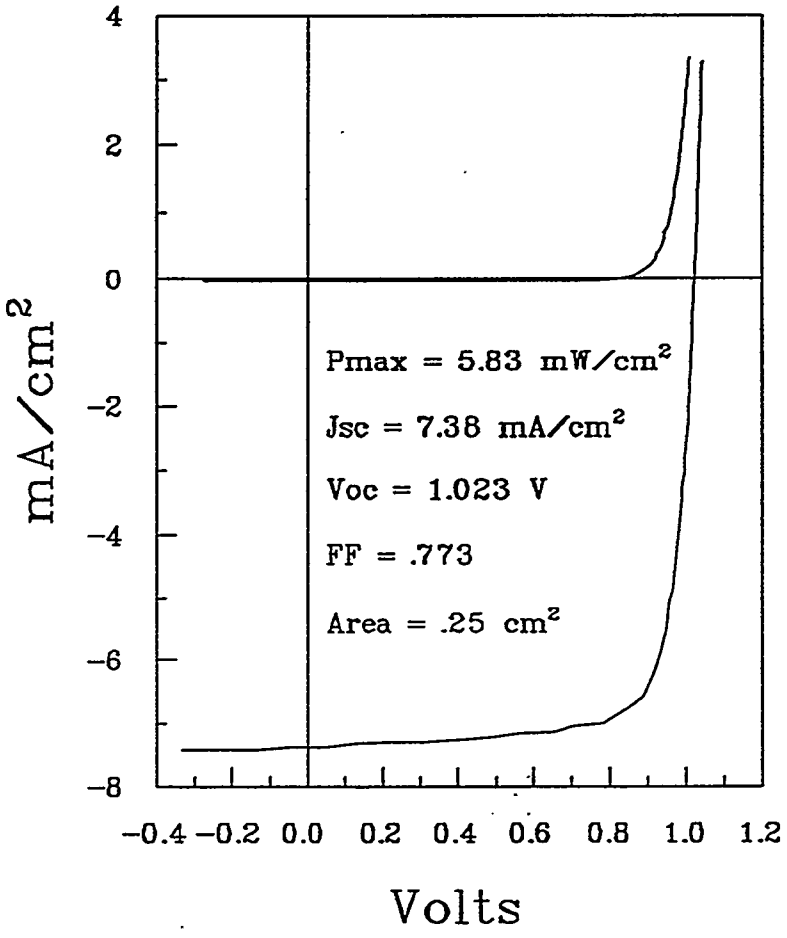

Fig. 15. **Initial J-V characteristic of a thin *p i n* cell with hydrogen dilution.**

In order to study any correlation between film property and solar cell performance, intrinsic films of ~ 2 μm thickness were grown on crystalline silicon and 7059 glass for IR and CPM measurements using the four deposition conditions.

IR absorption was used to find out if samples grown by high hydrogen dilution contain more hydrogen. Analyses on IR data reveal that there are similar concentrations of bonded hydrogen for a given temperature. Films deposited at 300 °C with high and low dilutions exhibit ~9% and ~8% bonded hydrogen, respectively, while 175 °C films show ~12% and ~13% bonded hydrogen for high and low dilutions, respectively. Whereas there is no significant difference in the hydrogen concentrations, one may recall from Table 6 that optical calculations indicate a 20 meV difference in bandgap for different dilutions.

CPM measurements were carried out on the four samples deposited on glass both before and after light soaking. It was observed that all four samples had similar Urbach energy of 47 to 49 meV. The sub-bandgap absorption data are listed in Table 7. In the initial state, the defect density for a given temperature is within a factor of 2 from each other; the values are even closer for the degraded state. CPM data, therefore, are not at all consistent with what was observed for the solar cell performance. One may recall that the cell prepared with low dilution and at low temperature suffered much larger degradation than the rest, but this information is not reflected in the CPM data. We have previously reported[32] on the lack of correlation between film properties and solar cell performance for amorphous silicon germanium alloys; it is once again shown here in this study. Since the a-Si:H films for CPM measurement were deposited on glass substrates and solar cells were deposited on stainless steel substrates, the effect of different substrates on material quality can not be excluded. Moreover, there is a fundamental issue involving the relevance of measurement in a coplanar configuration (CPM) for obtaining information of transport in transverse direction (solar cell). Therefore, it is important to characterize intrinsic a-Si:H quality in a solar cell configuration.

Primary photocurrent (PPC) measurements have been used to measure the quantum efficiency of a-Si:H solar cells. We report our experimental results of PPC measurement on the same four a-Si:H alloy solar cells listed in Table 6. Quantum efficiency in the red and infrared range of these four cells in degraded states is shown in Figs. 16 and 17, respectively, for two pairs of cells deposited at 175 and 300 °C. QE in the range of 1.4 ~ 1.7 eV is mainly contributed by carrier transitions between valence band tail states and conduction band, while QE < 1.4 eV provides information of optical absorption coefficients due to defect states in the gap. It is clearly shown in Fig. 16(a) that in the degraded state, the cell made at 175 °C with low hydrogen dilution (L6156) has higher QE than the cell made at the same temperature but with high hydrogen dilution (L6186), and the ratio of QE is about 2.5 for photon energies less than 1.4 eV (see Fig. 16(b)). The difference in QE for the other pair of cells made at 300 °C is smaller (see Fig. 17), the wavy shape of the ratio shown in Fig. 17(b) is due to a small difference in the thickness of the samples. Note that the sub-bandgap QE measured by PPC agrees well with the cell performance listed in Table 6; namely, degradation is higher for cells with low hydrogen dilution, specially for cells deposited at 175 °C.

The fact that the cell made with high hydrogen dilution shows lower sub-bandgap QE than that made with low hydrogen dilution indicates that less defect is created in the intrinsic layer of the cell made with high hydrogen dilution after light soaking, hence better stability.

Small angle X-ray scattering (SAXS) experiments were carried out at Colorado School of Mines on samples deposited on thin Al-foil using nominally identical conditions as those listed in Table 7. The result is summarized in Table 8. It is surprising to note that all four samples show similar microvoid volume fraction as well as scattering characteristics, while corresponding solar cells show different degradation behavior as discussed before and shown in Table 6. One may recall that we had previously observed correlation between microstructure and solar cell performance for cells deposited at different rates. No apparent correlation is found for cells deposited with different hydrogen dilution.

In conclusion, we have studied the effect of hydrogen dilution on a-Si:H film property and solar cell performance for two different deposition temperatures. We found that cells with high hydrogen dilution gave rise to better performance both before and after light soaking. However, film properties obtained from IR, SAXS, and CPM experiments do not correlate well with cell performance.

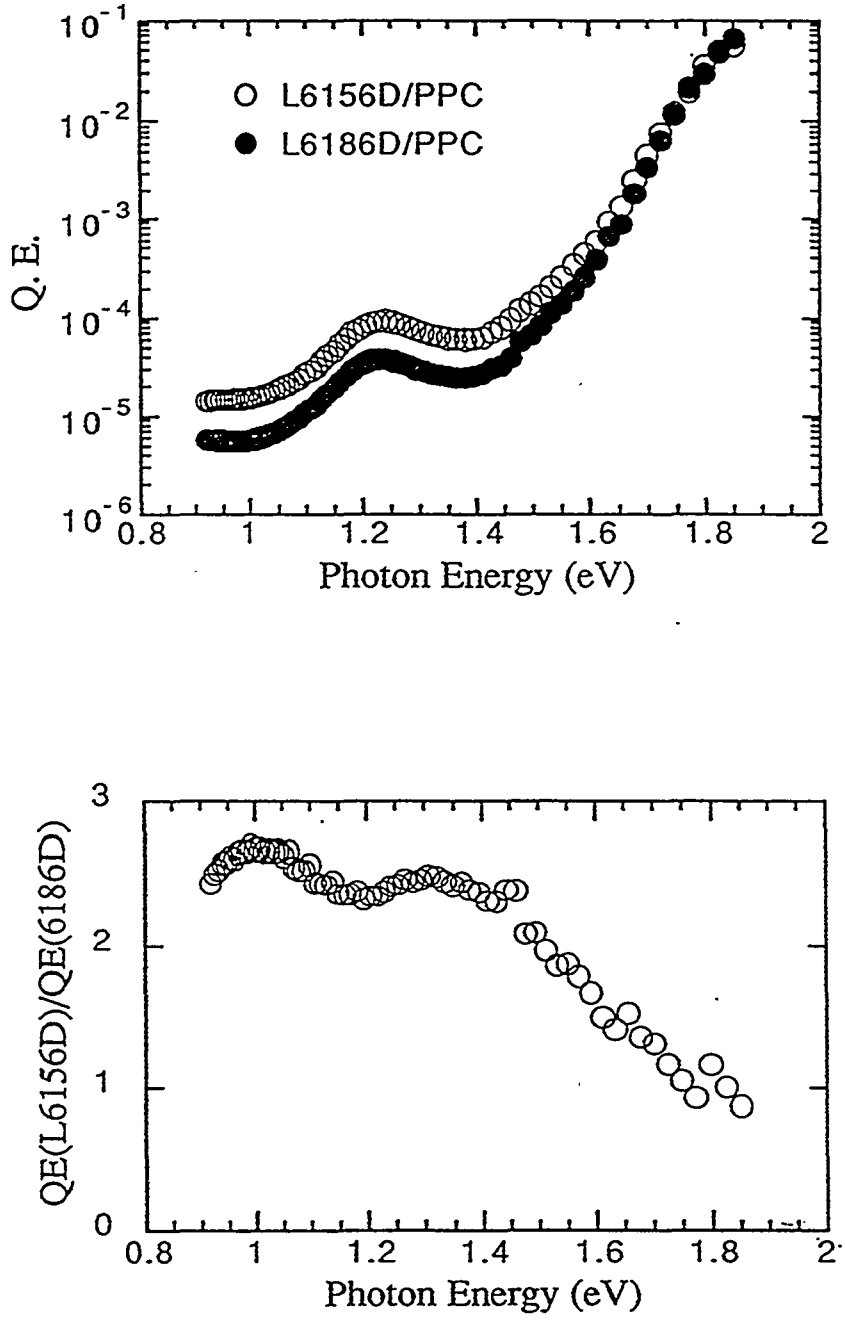

Figure 16. **(a) Quantum efficiency, and (b) the ratio of quantum efficiency in degraded state for the a-Si:H cells deposited at 175 °C.**

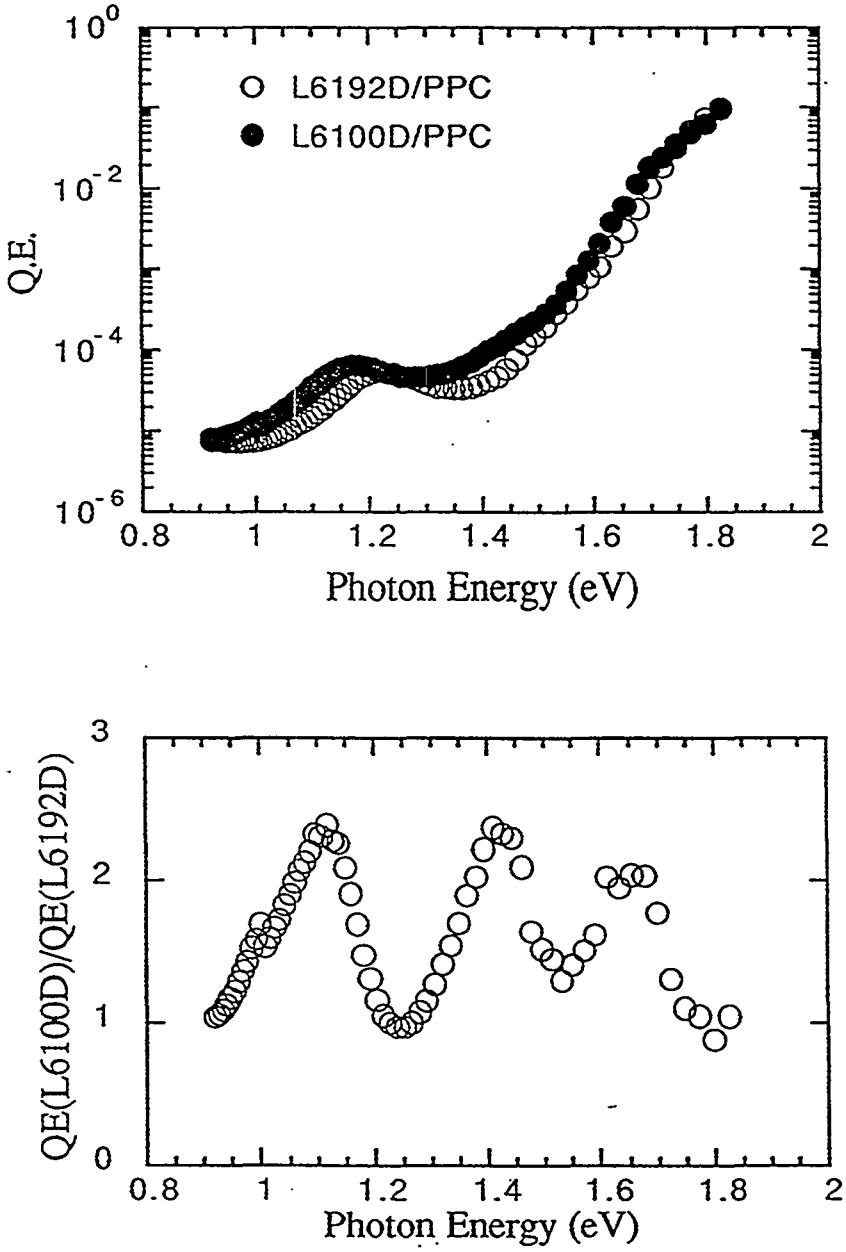

Figure 17. **(a) Quantum efficiency, and (b) the ratio of quantum efficiency in degraded state for the a-Si:H cells deposited at 300 °C.**

Table 7. CPM Data on High and Low Hydrogen Dilution Films.

Description	Initial Defect Density (cm^{-3})	Degraded Defect Density (cm^{-3})
300 °C Low Dilution	2.9×10^{15}	2.9×10^{16}
300 °C High Dilution	4.4×10^{15}	3.0×10^{16}
175 °C Low Dilution	7.9×10^{15}	3.0×10^{16}
175 °C High Dilution	5.0×10^{15}	2.5×10^{16}

Table 8. SAXS Data on High and Low Hydrogen Dilution Films.

Sample	Ts(°C)	H-dil.	thickn. (micr.)	Q_0 ($10^{-6}nm^{-2}$)	Q_0/Q_{45} (%)	max V_f (10^{-7})	I(alloy) (g/cc)	D(flot.)
6403	300	low	2.34	0.37	>1	0.1	0.93	2.244
6407	300	high	1.99	0.74		0.2	0.79	2.225
6405A	175	low	1.56	0.86	~1	0.2	1.5	2.219
6405B	175	high	1.56	0.83		0.2	0.93	2.218

Effect of High Hydrogen Dilution on a-SiGe Alloy Cells

We have previously reported that high hydrogen dilution with optimized deposition conditions results in improved performance of a-Si alloy solar cells in both the initial and degraded states. Primary photocurrent (PPC) studies on a-Si cells reveal that after light soaking less defects are created in the cell made with high hydrogen dilution than the cell made with low hydrogen dilution. In order to see the effect of hydrogen dilution on amorphous silicon germanium alloys, we have extended the study to a-SiGe alloy solar cells.

Two sets of a-SiGe alloy cells with different intrinsic layer thicknesses, i.e., ~190 nm and 375 nm, were deposited on stainless steel substrates without back reflector. To avoid complexity, the intrinsic layer of all the samples was made without bandgap profiling. The characteristics of these a-SiGe:H cells are listed in Table 9 for both the initial and degraded states. The light soaking conditions are one-sun, 50 °C in open-circuit mode. It is clear that not only do the cells deposited with high hydrogen dilution show better cell performance in the initial state, but also degrade less after 500 hours of light soaking. The high hydrogen diluted cells also show a tendency of saturation in degradation after 200 hours.

Primary photocurrent (PPC) measurements have been made on these cells in both the initial and degraded states. The increase of quantum efficiency (QE) in a range of 0.9 to 1.2 eV was observed after light soaking. The ratio of QE (1.1 eV) after 500 hour light soaking to that of initial state is 2.2 for high hydrogen diluted cells and 2.9 for lower hydrogen diluted ones. It is interesting to note that although PPC data of a-SiGe cells can qualitatively explain the better stability for high hydrogen diluted samples, the relative increase of QE in the sub-bandgap region for a-SiGe cells is much smaller than that for a-Si cells.

Table 9. Hydrogen Dilution Effect on a-SiGe Cells.

Sample #	State	H_2 Dilution	Thickness (nm)	P_{max} (mW/cm^2)	J_{sc} (mA/cm^2)	V_{oc} (V)	FF
L6616	Initial	High	375	7.96	18.0	0.74	0.59
	70 hrs			5.88	17.0	0.70	0.48
	200 hrs			5.42	16.5	0.70	0.47
	500 hrs			5.23	16.3	0.69	0.46
L6619	Initial	Low	375	7.09	17.6	0.72	0.55
	70 hrs			5.12	16.3	0.67	0.47
	200 hrs			4.50	15.5	0.66	0.43
	500 hrs			4.13	15.0	0.65	0.42
L6613	Initial	High	190	7.63	15.7	0.75	0.65
	70 hrs			6.46	15.3	0.71	0.59
	200 hrs			5.89	15.0	0.70	0.56
	500 hrs			5.87	15.1	0.70	0.56
L6620	Initial	Low	195	7.13	15.6	0.72	0.64
	70 hrs			5.74	15.2	0.68	0.56
	200 hrs			5.08	14.8	0.66	0.52
	500 hrs			4.78	14.7	0.65	0.49

Thermal Annealing Study

It has been recently shown[21] that a-SiGe:H alloy films with Ge-content > 20% show a sharp increase in microvoid density measured by small angle X-ray scattering (SAXS). In a-Si:H films with large microvoid density, light-induced defects have been found to be more difficult to anneal out, and this has resulted in lack of saturation of the cell degradation, even after long light exposure time.[33] Saturation of light-induced degradation is extremely important for commercialization of a-Si:H alloy solar cells. We have therefore carried out studies of the saturation behavior and thermal annealing recovering of light-induced degradation in a-SiGe:H cells with different Ge-content.

Since the light-induced defects in a-Si:H alloys with large microvoid density are more difficult to be annealed out, one may expect that light-induced defects in a-SiGe:H alloys are also more difficult to be annealed out due to higher microvoid densities (when Ge-content > 0.2). However, we find that the light-induced defects in a-SiGe:H cells can be thermally annealed out at almost the same rate as in a-Si:H with low density of microvoids.

Annealing recovery data for four a-SiGe:H alloy cells are listed in Table 10 along with two a-Si:H cells with different microvoid densities. η_i is the initial efficiency, η_{D1} is the efficiency after one-sun light soaking for 600 hours at 50 °C, and η_{A1} is the efficiency after subsequent recovery after 150 °C 90-minute annealing. The cells were next fully annealed and degraded again under intense illumination. η_{D2} is the efficiency after 30-sun degradation, and η_{A2} is the efficiency after subsequent annealing recovery. Special attention was paid to ensure that the level of degradation after accelerated light soaking is similar to that after one-sun soaking for 600 hours. Among four a-SiGe:H cells, three have flat bandgaps, 1.65, 1.50, and 1.42 eV, respectively. The fourth one has a profiled bandgap similar to the bottom cell of our triple-junction cells. We can see from Table 10 that for all four a-SiGe:H cells, 90-minute annealing at 150 °C can recover the cell performance up to 90-95%, while the same annealing process can only recover the efficiency to about 80% for a-Si:H cell with large microvoid density. Note also that thermal annealing recovery behaves similarly after one-sun or accelerated (~30 suns) light soaking, which is quite different from the annealing behavior of a-Si:H cells.[33]

Table 10. **Annealing Behavior of Degraded a-Si:H and a-SiGe:H Alloy Solar Cells.** D1 designates the degradation under one-sun 600 h 50 °C condition and A1 the subsequent recovery after 150 °C 90-minute annealing. D2 represents 30-sun degradation and A2 the subsequent annealing recovery.

Sample #	4625	4675	5203	6382	6363	6362
Ge (at.%)	0	0	profiled	10	30	40
η_i (%)	7.78	6.31	8.89	6.90	7.10	5.41
η_{D1}/η_i(%)	84.3	53.2	71.4	79.0	65.9	68.0
η_{A1}/η_i(%)	96.1	79.9	96.4	94.4	89.5	90.2
η_{D2}/η_i(%)	83.9	53.6	71.9	72.6	68.3	72.5
η_{A2}/η_i(%)	100	89.4	94.8	96.6	94.5	90.2
E_{opt} (eV)	1.72	1.78		1.65	1.50	1.42

Optimization and Stability of Component Cells in Multijunction Structure

In order to obtain improved performance of both double- and triple-junction modules, we have made component cells for the two cases and have studied their performance both in initial and light-soaked conditions. In our study, a-Si alloy was used for the top cells, and the bottom cells used amorphous silicon germanium (a-SiGe) alloy. For middle cells, both a-Si and a-SiGe alloys were used. The thicknesses of the cells were chosen so as to provide short-circuit current density as appropriate for the multijunction structure. The top and middle cells were deposited on textured substrate without any back reflector, since in the multijunction configuration these cells do not see much reflected light. The bottom cells were deposited on our conventional silver/zinc oxide (Ag/ZnO) textured back reflector.

Typical initial performances for state-of-the-art component cells for the triple-junction structure are shown in Table 11.[31] Also shown are the values after filtered one-sun (metal-arc lamp), 50 °C, 600 h light soaking. In this experiment, component cells were degraded under open-circuit condition at 50 °C for 600 h and measured at 25 °C. The top cell was degraded under one sun and measured under AM1.5 illumination; the middle cell was degraded under one sun with a 530 nm cut-on filter and measured under AM1.5 illumination with the same filter; the bottom cell was degraded under one sun with a 630 nm cut-on filter and measured under AM1.5 illumination with the same filter. We should mention that one can improve the initial performance by making the component cells thicker, but this results in larger degradation and lower light-degraded efficiency.

Table 11. **Present Status at United Solar of Typical Initial and Degraded Cell Parameters for Component Cells Degraded and Measured under Conditions Described in the Text.** The high- and the mid-bandgap cells use Cr as back reflector. Use of Ag/ZnO as back reflectors for these cells increases J_{sc} by 30% to 40%.

			J_{sc} (mA/cm^2)	V_{oc} (V)	FF	P_{max} (mW/cm^2)
a-Si	high-bandgap cell	initial	7.3	1.01	0.75	5.53
		degraded	7.2	0.98	0.71	5.01
		degradation (%)	1.4	3.0	5.3	9.4
a-Si	mid-bandgap cell	initial	6.44	0.90	0.70	4.02
		degraded	6.22	0.87	0.61	3.29
		degradation (%)	3.4	3.3	12.9	18.2
a-SiGe	mid-bandgap cell	initial	7.02	0.77	0.65	3.51
		degraded	6.85	0.74	0.57	2.89
		degradation (%)	2.4	3.9	12.3	17.7
a-SiGe	low-bandgap cell	initial	7.8	0.67	0.64	3.34
		degraded	7.7	0.65	0.56	2.80
		degradation (%)	1.3	3.0	12.5	16.2

We note that the component cells degrade between 9% to 18%. Similar studies[30] done on component cells for double-junction structure show a top cell degradation of 12% and a bottom cell degradation of 18%. However, the top cell of the triple-junction structure degrades by only 9% as compared to 12% for that of the double-junction structure. If one designs the multijunction structure in a way so as to make the operation limited by the top cell current, one would expect to see a lower degradation in triple-junction cells than that in double-junction ones.

As mentioned earlier, top cell in our structure does not use any carbon. By using hydrogen dilution to improve the quality of the *i* layer and incorporating high conductivity microcrystalline *p* layer[34] to improve built-in potential, we have obtained for the top cell an initial open-circuit voltage (V_{oc}) of 1.023 V, a fill factor (FF) of 0.77 and a short-circuit current density (J_{sc}) of 7.4 mA/cm^2. This is the best performance of the top cell as reported in the literature.

We should also mention that all the component cells in this study show true saturation in efficiency after prolonged light exposure. A typical example for the top and the bottom cell is shown in Fig. 18. The degradation is much lower than those obtained under intense light illumination, demonstrating the importance of thermal annealing of defects under normal operating conditions.

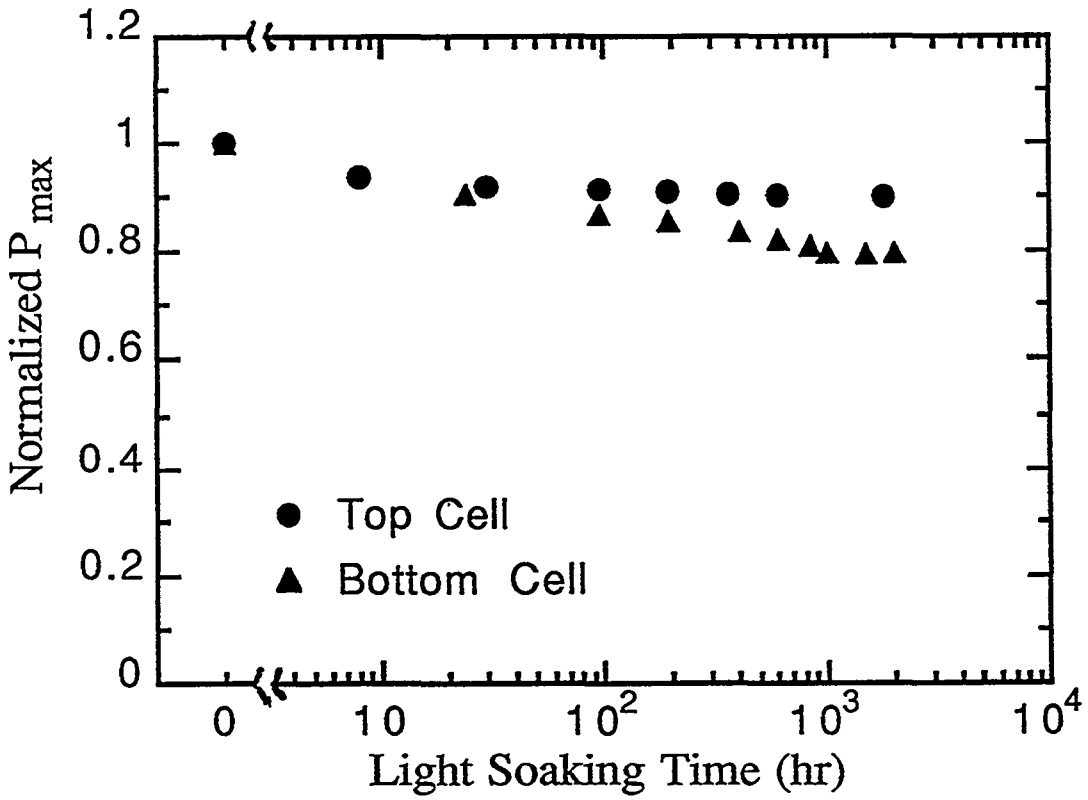

Figure 18. **Saturation in light-induced degradation of component cells in a dual-junction structure.**

Stability Study on Double-junction Cells

We have previously reported[35] that initial conversion efficiencies of ≥ 13% can be achieved in amorphous silicon-based multijunction solar cells. Here we report the results of our stability study on various dual-bandgap, double-junction devices in which the top and bottom cells were made from hydrogenated amorphous silicon (a-Si:H) and hydrogenated amorphous silicon-germanium (a-SiGe:H) alloys, respectively.

To obtain a high-performance, double-junction cell, the component cells should have high efficiency and stability. However, the quality of the narrow bandgap a-SiGe:H material is usually poorer than that of a-Si:H. One can get better results by mismatching the cells so that the limiting cell is the a-Si:H cell, which has a better fill factor.

We have fabricated various double-junction 0.25 cm^2 devices in which the bottom a-SiGe:H cells have bandgaps ranging from 1.41 to 1.55 eV. We have studied the effect of bandgap variation and current-mismatching on the stability of the double-junction devices. Most of the devices investigated stabilized at an active-area efficiency of about 10% while the best performance was obtained from incorporating a profiled bandgap in the bottom cell having a bandgap of 1.41 eV at the narrowest region. A stabilized active-area efficiency of 11.16% was observed after 600 hours of one-sun illumination at 50 °C. This is believed to be the highest stabilized value reported to date on amorphous silicon-based double-junction solar cells.

To study the effect of bandgap variation, we made three double-junction samples in which the bottom cells have a *constant* bandgap of 1.55 eV (L4781), 1.50 eV (L4786), and 1.41 eV (L4801), respectively, and the top cells were made from 1.75 eV a-Si:H material using the same deposition parameters. These samples were deposited onto stainless steel/textured silver/zinc oxide substrates using the conventional RF glow discharge technique. The thickness of the top cells was made small so that the fill factor is high and the current of the double-junction device is limited by the top cell. This would allow us to evaluate the effect of the bottom cell on the stability of the double-junction structure. The initial performance of these devices measured under a global AM1.5 solar simulator is listed in Table 12. It is noted from the quantum efficiency data that the current is limited by the top cell, and the mismatch between the top and bottom cells ranges from 1.5 to 3 mA/cm^2.

We have also made a double-junction device (L4808) in which the thickness of the top cell was made larger such that the top cell current is nearly the same as that of the bottom cell. In this case, we have used the 1.55 eV a-SiGe:H cell in the bottom cell. The initial performance of the double-junction device is also listed in Table 12. The quantum efficiency data confirms that the two currents are nearly matched.

These samples were then light-soaked with one-sun illumination at 50 °C under open-circuit condition for 600 hours. Their degraded J-V characteristics and quantum efficiency data are also listed in Table 12.

Table 12. Initial and Stabilized Photovoltaic Characteristics of Various Dual-gap, Double-junction Devices.

Sample	State	J_{sc} (mA/cm^2)	V_{oc} (V)	FF	η (%)	Q (mA/cm^2)
L4801	Initial	9.60	1.60	0.73	11.21	9.35/12.27
(1.41 eV)	600 hrs	9.52	1.55	0.68	9.97	9.21/11.71
L4786	Initial	9.70	1.65	0.74	11.84	9.47/11.42
(1.50 eV)	600 hrs	9.70	1.59	0.67	10.36	9.46/10.86
L4781	Initial	9.67	1.68	0.74	12.02	9.43/10.89
(1.55 eV)	600 hrs	9.66	1.61	0.66	10.24	9.29/10.65
L4808	Initial	10.05	1.66	0.70	11.68	10.24/10.49
(1.55 eV)	600 hrs	9.98	1.60	0.62	9.88	10.07/10.38

Each sample consists of several 0.25 cm^2 active-area devices. The measurements were made using a single-source AM1.5 solar simulator at 25 °C. The Q-values refer to the top cell and the bottom cell, respectively.

One can readily make the following observations:

1. On the initial performance of L4781, L4786, and L4801:

   a. As the bandgap of the bottom cell decreases, V_{oc} also decreases as expected. Sample L4801, which has the narrowest bandgap in the bottom cell, exhibits the largest current mismatch between the component cells.

   b. J_{sc} and fill factor are similar for the three devices because of the same deposition parameters used for the current-limiting top cells.

   c. The initial efficiency of the double-junction devices is hence essentially dependent on V_{oc}. Sample L4781, which has the least Ge in the bottom cell, shows the highest initial efficiency.

2. The initial performance of sample L4808, which has the same bottom cell as L4781, exhibits a higher J_{sc} value because of the thicker top cell. However, the fill factor of the devices is lower than the other three samples due to the closer match. Its V_{oc} is also slightly smaller than L4781 due to the thicker top cell.

3. On the degraded J-V characteristics of samples L4781, L4786, and L4801:

   a. Sample L4801, which has the narrowest bandgap in the bottom cell, shows the lowest V_{oc}, consistent with the initial performance.

   b. Sample L4801 has a slightly better fill factor due to the larger current mismatch.

   c. J_{sc} remains similar for the three samples.

   d. The percentage of degradation and stabilized efficiencies are similar for the three samples.

4. The degraded performance of sample L4808, which has a thicker top cell than L4781, shows a lower fill factor due to closer matched component cells, and J_{sc} remains higher due to the thicker top cell.

From the above analysis, one can see that in order to achieve a higher stabilized efficiency, one should current-limit the top cell. The desired amount of mismatch depends on the performance of the bottom cell. If the performance of the bottom cell is improved, the mismatch can be reduced, and one can then take advantage of a thicker top cell for higher J_{sc} without losing too much on the fill factor.

We have designed a double-junction device in which we have incorporated a *profiled* bandgap structure in the bottom a-SiGe:H cell which we have previously shown to improve solar cell performance.[36] The bandgap in the narrowest region is 1.41 eV, and the top cell is 1.75 eV a-Si:H. The initial performance of this device is listed in Table 13. After 600 hours of one-sun illumination at 50°C, the stabilized active-area efficiency as measured under global AM1.5 single-source simulator at 25 °C is 11.16%, which we believe is the highest value reported to date on double-junction amorphous silicon alloy solar cells.

Table 13. Initial and Stabilized Photovoltaic Characteristics of a Dual-gap, Double-junction 0.25 cm² Device with Profiled Bandgap in the Bottom Cell.

Sample	State	J_{sc} (mA/cm²)	V_{oc} (V)	FF	Active Area (cm²)	η (%)
L4789	Initial	10.67	1.650	0.716	0.2465	12.61
	600 hrs	10.61	1.606	0.655	0.2465	11.16

Cell Stability Under Different Light Spectrum and Temperature

We have been carrying out light-induced degradation studies using a metal arc lamp which has a different spectrum from global AM1.5 (Fig. 19). In order to ascertain the effect of this difference in spectrum on cell stability, we have carried out degradation studies on both double- and triple-junction cells using the metal arc source and also a global AM1.5 simulator. The samples used are small-area cells obtained in the same deposition run. The results for double- and triple-junction cells are shown in Figs. 20 and 21, respectively. We find virtually no difference in the cell degradation using the two light sources. Light soaking under the metal arc lamp can therefore be used to ascertain the degradation under global AM1.5 condition.

We have reported that degradation after prolonged light soaking at 50 °C for double- and triple-junction a-Si alloy solar cells are 12-16% and 11-14%, respectively. To study the effect of the temperature at which light soaking experiments are performed, we have degraded double- and triple-junction a-Si alloy solar cells at two different temperatures, i.e., 50 and 30 °C.

Characteristics of double-junction (L5023) and triple-junction (L6064) a-Si alloy cells in original and degraded states (after 1360 hours of light soaking) are listed in Table 14. The samples were illuminated under the same light source with the same intensity but at different temperatures. It is very encouraging to note that the difference in degradation between 30 and 50 °C for our multijunction cells is only 4%, which is less than what we observed on thick a-Si single-junction cells in a previous study. Degradation appears to slow down after 400 hours of light exposure.

Table 14. Characteristics of Double-junction (L5023) and Triple-junction (L6064) a-Si Alloy Solar Cells Both in Original and Degraded States (at 30 and 50 °C, respectively).

Sample #	State	P_{max}	J_{sc}	V_{oc}	FF
Line 5023	Original	10.86	10.2	1.61	0.66
50 °C	1360 hr	9.50	9.81	1.58	0.61
	%	87.5	96.2	98.1	92.4
30 °C	1360 hr	9.06	9.81	1.57	0.61
	%	83.4	96.2	97.5	92.4
Line 6064	Original	11.87	7.05	2.39	0.71
50 °C	1360 hr	10.49	6.76	2.33	0.66
	%	88.4	95.9	97.5	93.0
30 °C	1360 hr	10.01	6.80	2.30	0.65
	%	84.3	97.6	96.2	91.5

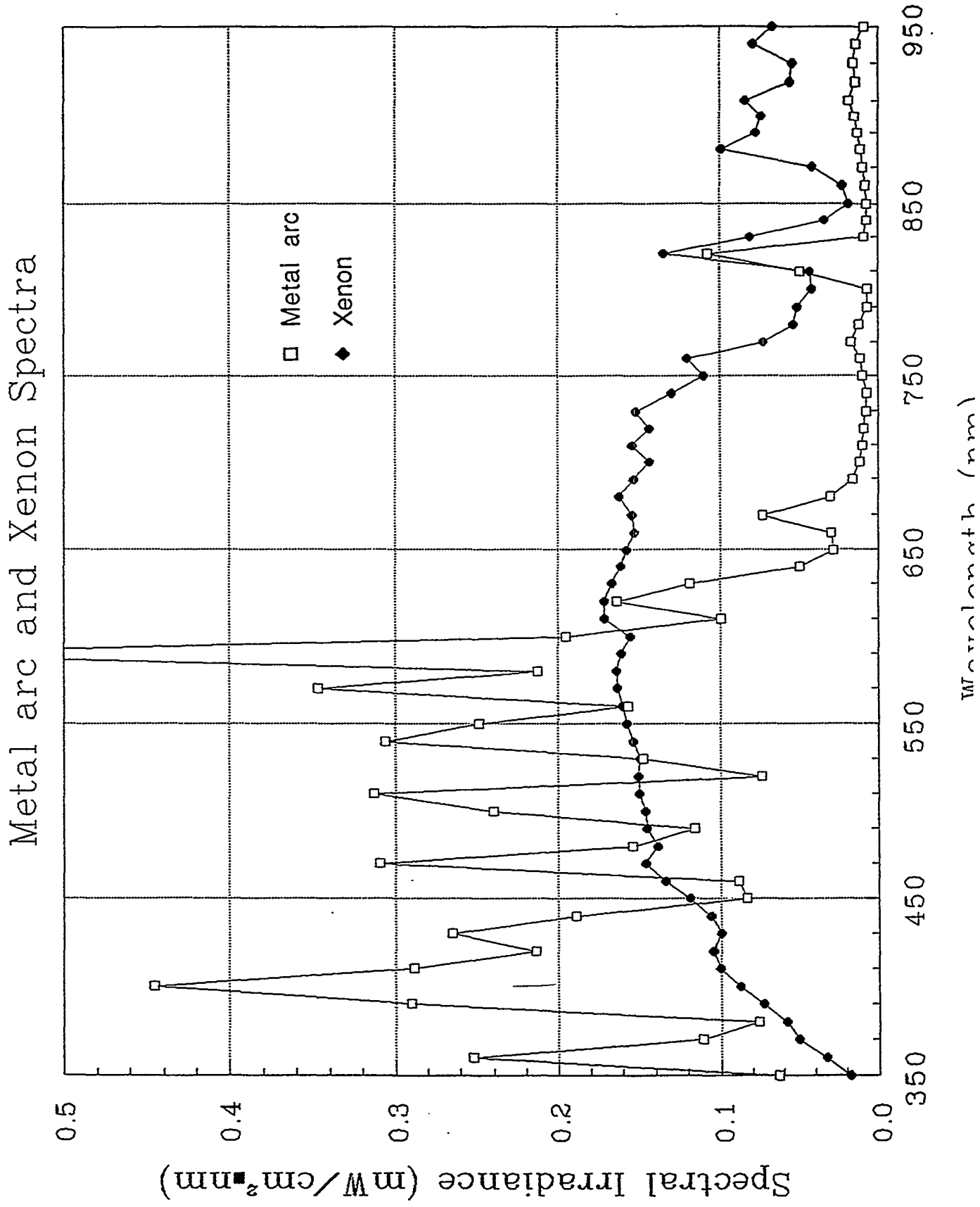

Figure 19. Spectrum of the metal arc lamp source and global AM1.5 simulator.

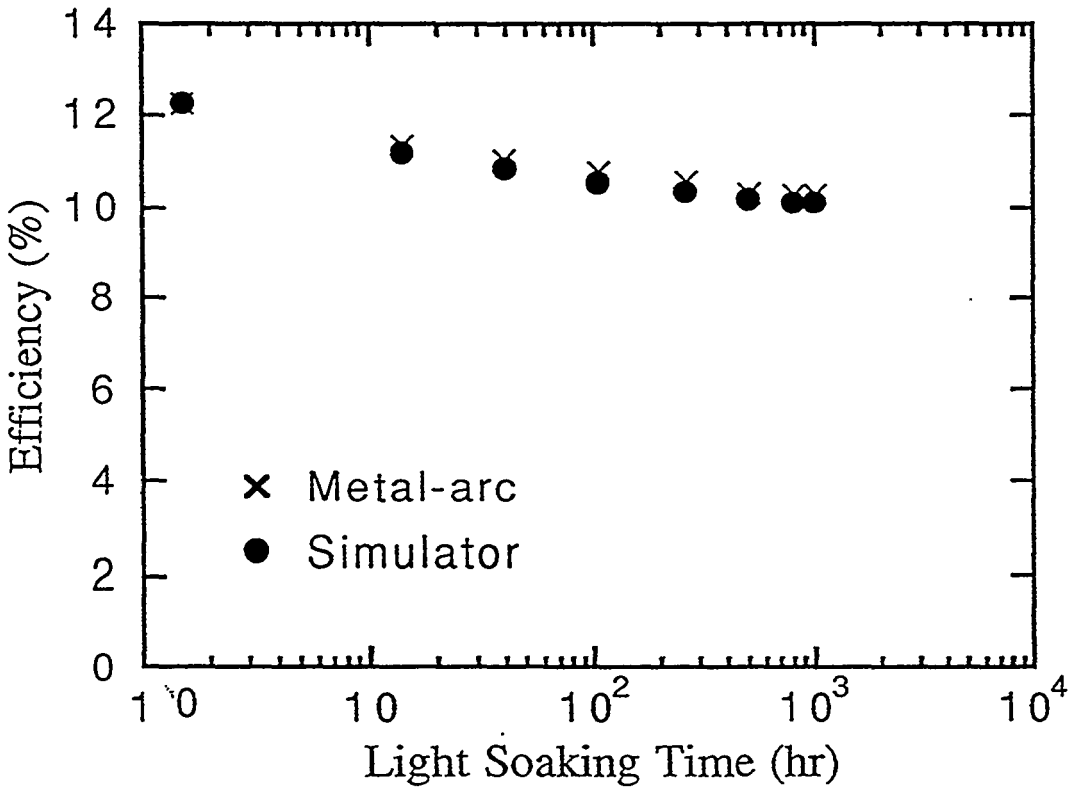

Figure 20. Degradation of double-junction cells after light soaking under the metal arc lamp and global AM1.5 simulator.

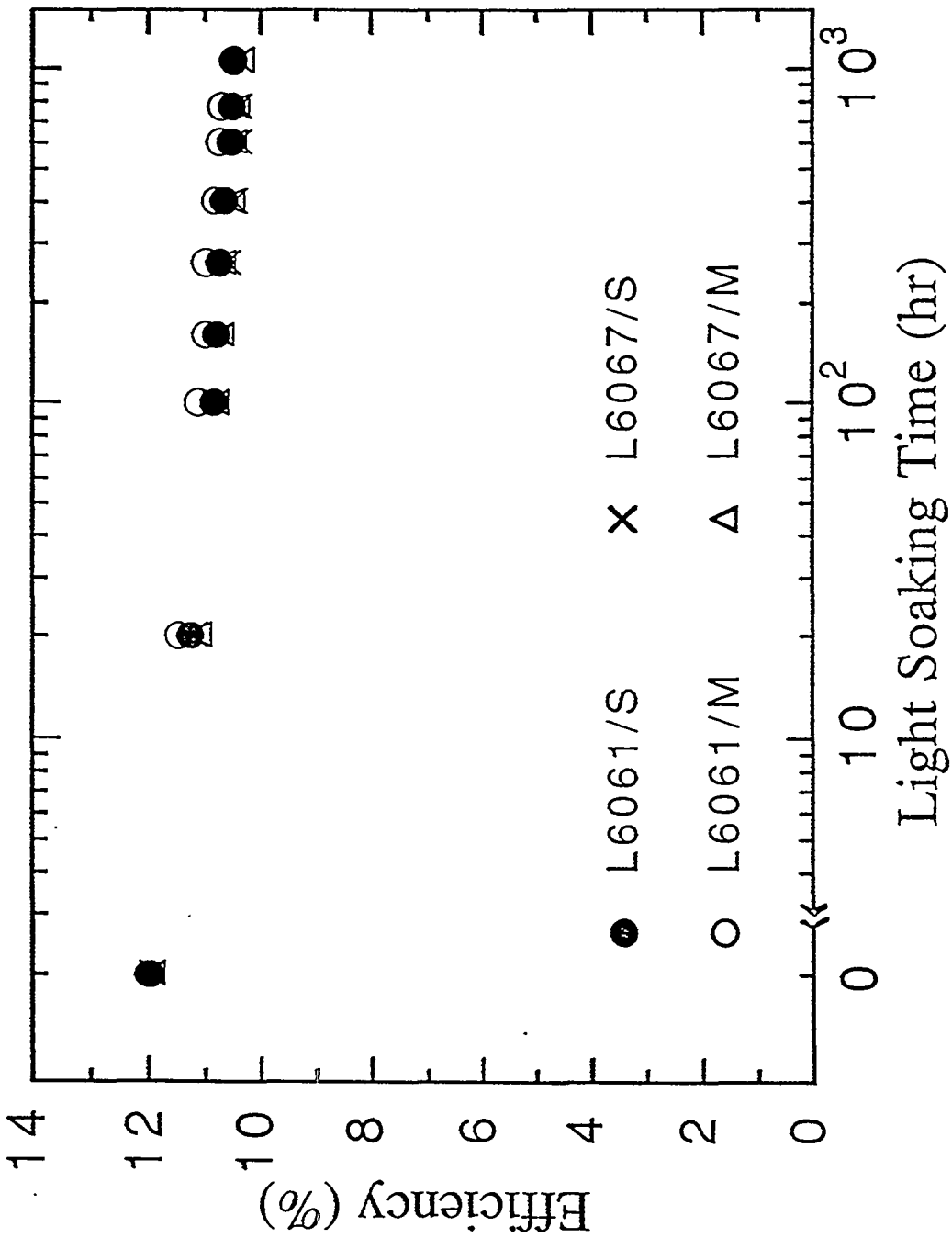

Figure 21. Degradation of triple-junction cells after light soaking under metal arc lamp (M) and global AM1.5 simulator (S).

Section 4

Large-area Deposition and Module Research

Introduction

Significant progress has been made on both module and small-area device results since the inception of the contract and especially during Phase III. The 2B machine has been used to prepare cells for large-area (~ 900 cm^2) module fabrication. Both dual-bandgap, double-junction and triple-bandgap, triple-junction structures have been studied. The top cell in both cases consists of an a-Si:H *i* layer, and the middle and bottom cells have a-SiGe:H alloy *i* layers. The back reflector consists of a textured Ag/ZnO film on a stainless steel substrate.

The cell fabrication procedure consists of first preparing the back reflector using a sputter deposition technique. The coated area is greater than 900 cm^2. The *n, i, p* layers are then deposited in the 2B machine. This is followed by an antireflection coating of ITO and top grid contact. The module is fabricated by appropriate encapsulation using EVA and Tefzel.

In this report, we present the results on both double-junction and triple-junction modules. Initial and stabilized module efficiencies as high as 11.8% and 10.2% have been confirmed[37] by NREL. The high efficiency has been attained as a result of careful and systematic analysis and optimization of component cells, "tunnel" junction between the top and bottom cells, and uniformity over an area of 900 cm^2.

Small-area Component Cells

In order to obtain high module efficiency, it is first necessary to obtain high efficiency small-area devices. The typical active area for the devices is in the range of 0.25-0.82 cm^2. The small-area devices have been fabricated by either depositing the top ITO films through a mask or by delineating small-area devices by appropriately etching the ITO film. Optimization of multijunction cells especially triple-junction cells is a complex process. Preliminary optimization of the component cells fabricated on suitable substrates is a helpful first step. The top and middle cells are prepared on stainless steel (s.s.) substrates and the bottom cell on Ag/ZnO back reflector. The measurements include the current-voltage (I-V) characteristics under AM1.5 illumination and in conjunction with appropriate optical filters and quantum efficiency (Q) versus wavelength curve.

The intrinsic layers used in the top, middle, and bottom cells are a-Si, intermediate bandgap a-SiGe, and narrow bandgap a-SiGe films, respectively. The J-V characteristics under AM1.5 illumination and Q curves of the top, middle, and bottom component cells of the triple-junction structure are shown in Figs. 22, 23, and 24, respectively. The value of current-density, J_{sc}, is determined in all cases from the integrated Q curve. Likewise, the corrected efficiency is calculated using the corrected J_{sc} from Q measurements. The values of maximum power, J_{sc}, short-circuit, V_{oc}, and FF of the three component cells are summarized in Table 15.

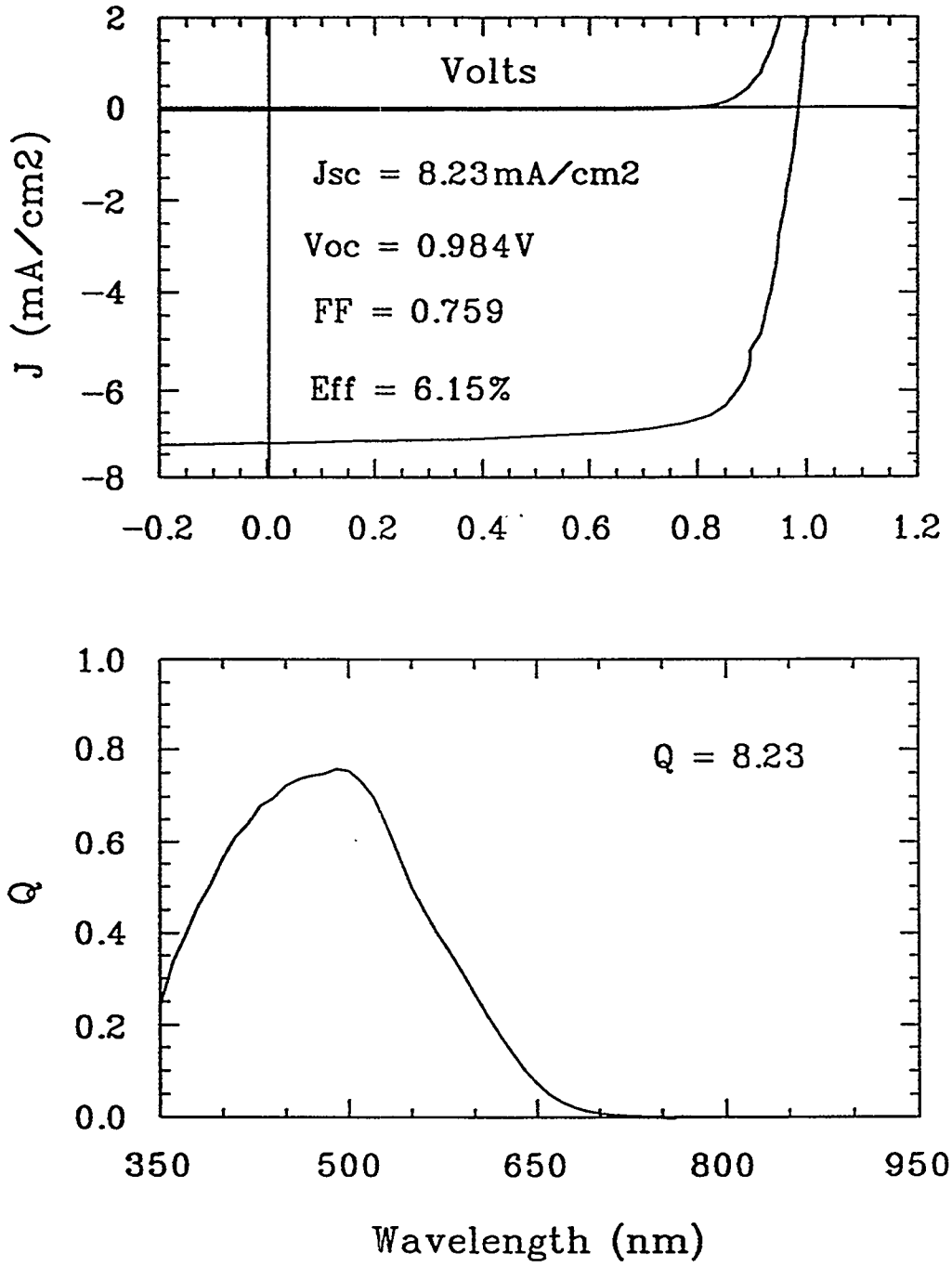

Figure 22. J-V characteristics and Q curve of the top component cell of a triple-junction structure.

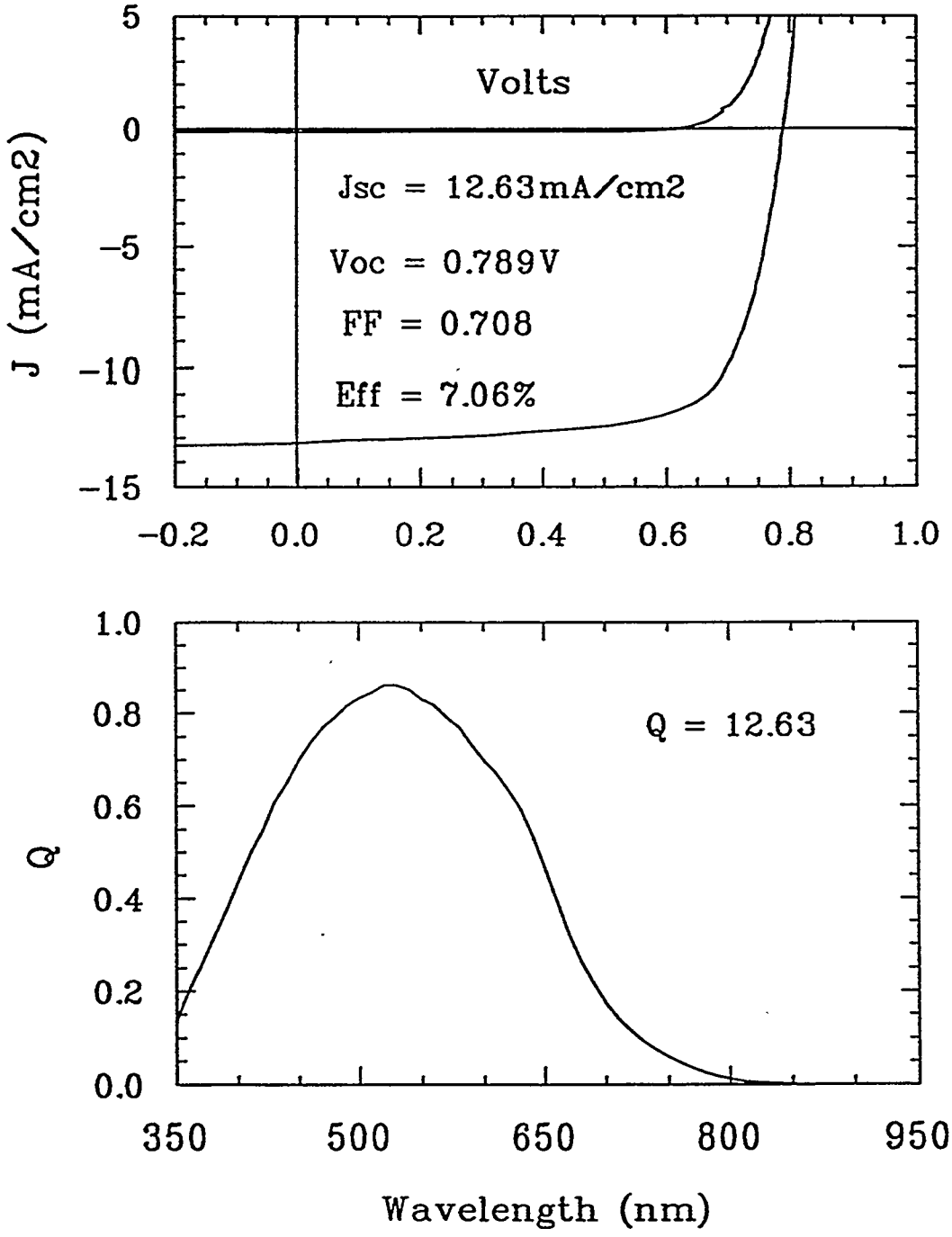

Figure. 23. **J-V characteristics and Q curve of the middle component cell of a triple-junction structure.**

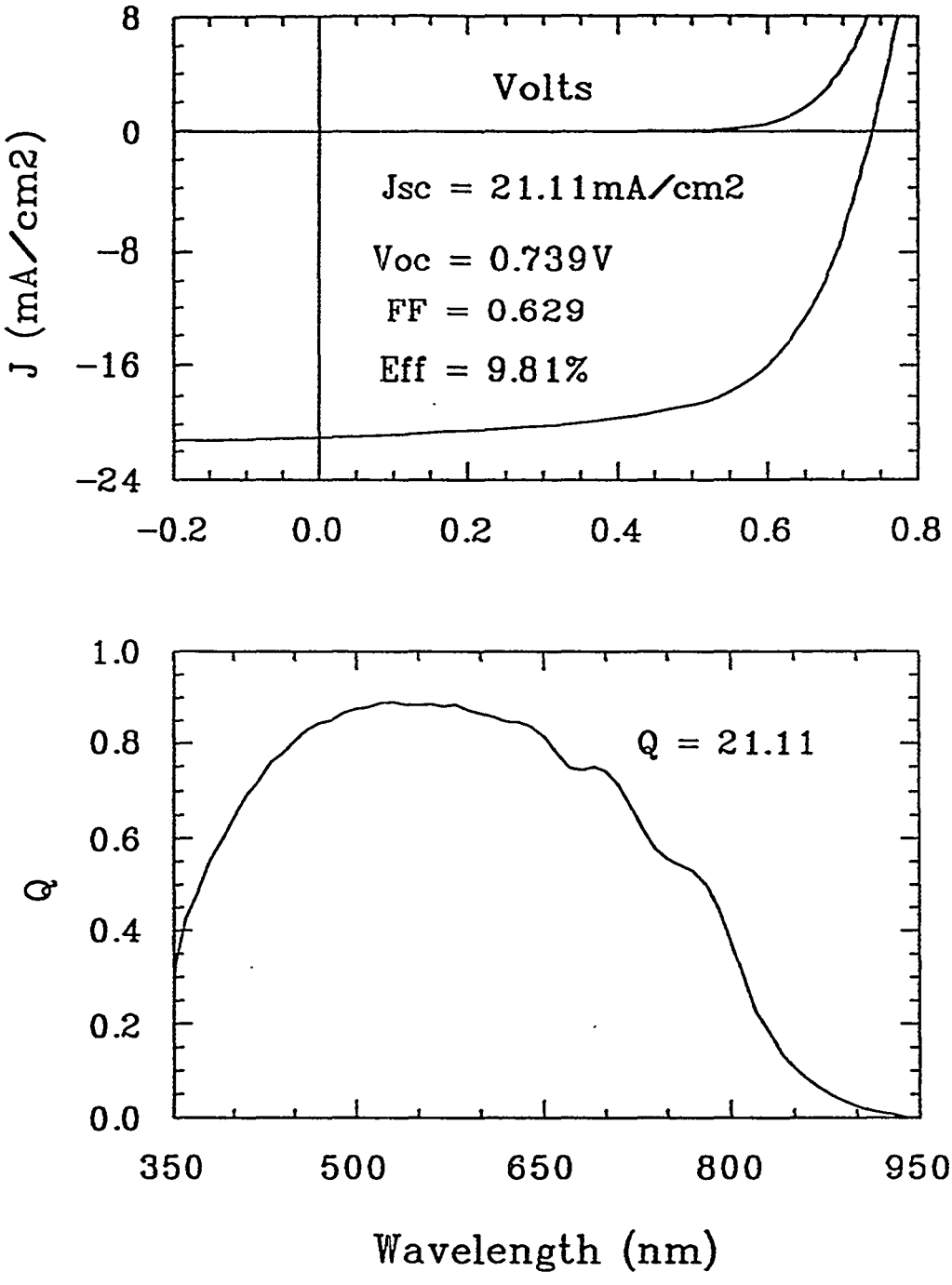

Figure 24. **J-V characteristics and Q curve of the bottom component cell of a triple-junction structure.**

Table 15. **Summary of Cell Characteristics of the Component Cells of a Triple-junction Structure under AM1.5 Illumination.**

Component Cell	Substrate	V_{oc} (V)	J_{sc} (mA/cm^2)	FF	Power (mW/cm^2)
Top	s.s.	0.984	8.23	0.759	6.15
Middle	s.s.	0.789	12.63	0.708	7.06
Bottom	Ag/ZnO	0.739	21.11	0.629	9.81

Tunnel-Junction Studies and Multijunction Cells

Since the inception of the project, considerable progress has been made in improving the efficiency of different types of devices made in the 2B machine. The methodology used was to compare the performance of the top cell, the bottom cell and the multijunction cells with the corresponding cells made in the LINE machine. In the past, the LINE machine had consistently outperformed the 2B machine in terms of both material quality and devices. Careful evaluation and analysis of the devices made in the two machines elucidated the shortcomings in the 2B machine. One problem was found to be in the internal "tunnel" junction of multijunction cells made in the 2B machine. Major changes were made both in the hardware and the deposition parameters of the 2B machine to fix the problem.

A new technique was developed[38] to characterize the internal "tunnel" junction of a multijunction cell. The device structure used for this purpose, hereby referred to as the NIPN structure, consists of the bottom n_1-i_1-p_1 cell followed by the n_2 layer. The NIPN device is coated with ITO dots for measurement. The current-voltage (I-V) characteristics of the NIPN structure have been found to be sensitively dependent on the quality of the p_1/n_2 "tunnel" junction. Evaluation of the NIPN device, therefore, provides a powerful way to investigate the quality of the internal junctions in a multijunction cell.

We should mention that so long as the n_2 layer is thick enough to screen the charge, the physics of transport at the *p/n* junction in the NIPN structure is the same as in the double-junction case. For the same incident radiation, however, the NIPN structure carries more current than the double-junction cell, and hence the effect of any limitation in the performance of the *p/n* junction for this structure is more pronounced on the current-voltage characteristic.

The NIPN studies have been used to investigate the effect of thickness of the *p* layer on the quality of the "tunnel" junction. For this purpose, NIPN devices of active area 0.25 cm^2 incorporating a-Si:H *i* layer were fabricated employing different thicknesses of the *p* layer. A corresponding set of a-Si:H *n-i-p* cells were also fabricated for comparison. Figure 25 shows a plot of V_{oc} and FF of both the NIPN and *n-i-p* devices as a function of *p* layer deposition time. Typical deposition rate is 0.1 nm/sec. The values of both V_{oc} and FF initially increase with deposition time and finally saturate in both cases. For the *n-i-p* structure, the values of V_{oc} and FF are higher than those for the NIPN structure at low deposition time. A deposition time for the *p* layer of as low as 20 s is found to give V_{oc} of 0.92 V; only a 5 s deposition time is adequate to give a FF of 0.72. In contrast, much thicker *p* layers with deposition time greater than 40 s are required to give comparable values of V_{oc} and FF for the NIPN structure. The highest values of V_{oc} and FF, corresponding to the longest *p* layer deposition time of 80 s, are similar for both cases and are 0.95 V and 0.75, respectively. The study shows that relatively thick *p* layers are required to form good quality "tunnel" junctions. Thus, a multijunction cell requires thicker *p* layers for efficient operation of the internal junctions than that required on the top for the *p*/ITO junction.

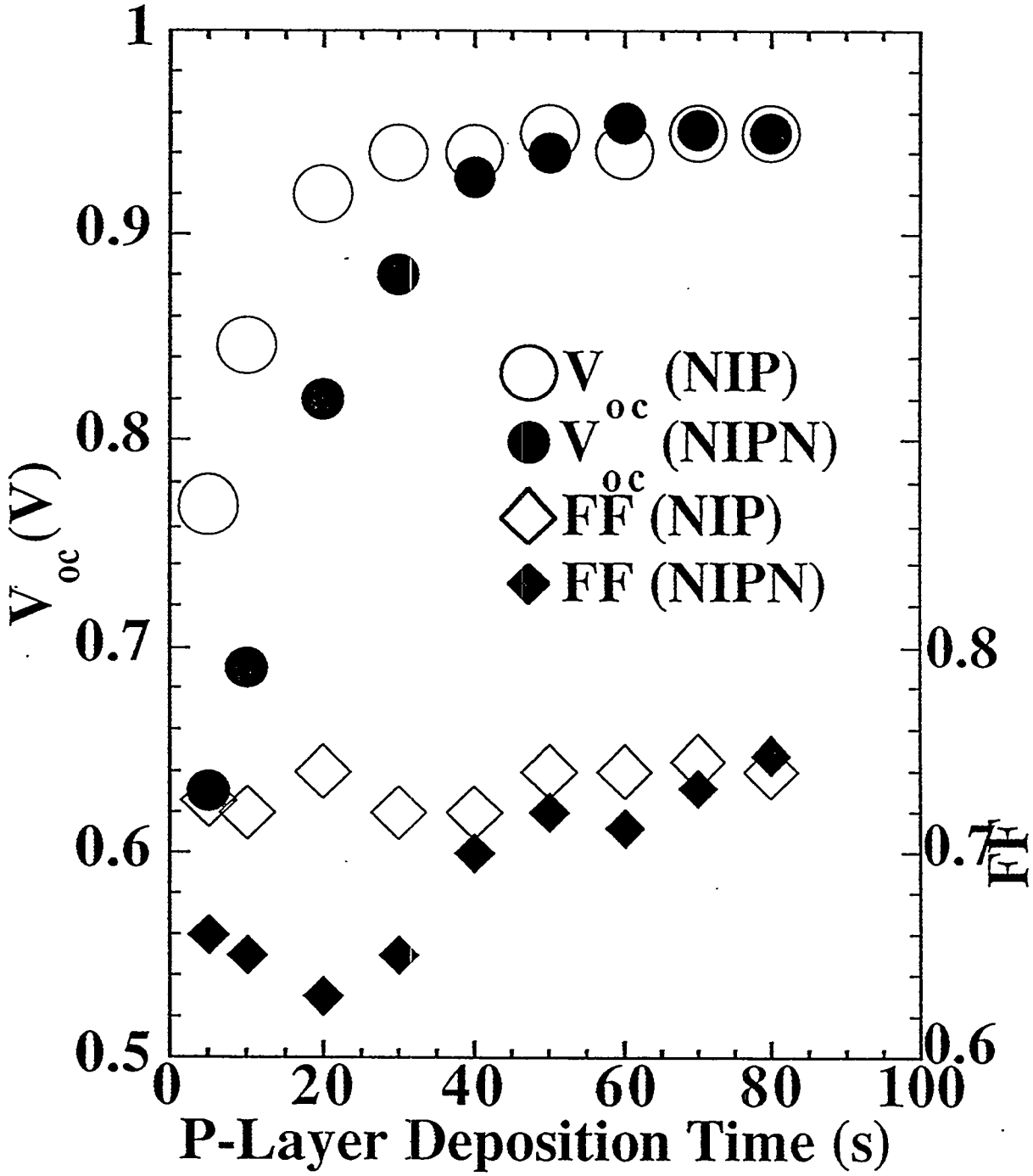

Figure 25. V_{oc} and FF of *n-i-p* and NIPN devices as a function of *p* layer thickness.

In order to investigate the qualitative aspect of the *p* layer at the "tunnel" junction, two types of *p* layers have been used to fabricate NIPN devices incorporating a-SiGe:H alloy *i* layers. The first one, referred to as Type A, consists of the conventional microcrystalline *p* layer deposited by 13.56 MHz rf glow discharge. Type B is also microcrystalline but prepared by 47 kHz low frequency glow discharge. The current density-voltage (J-V) characteristics of the two NIPN devices incorporating the Type A and Type B *p* layers are shown in Figs. 26(a) and 26(b), respectively. The devices do not have metal grid lines on top of the ITO. There is a sharp contrast in the quality of the two J-V characteristics under illumination. For Type B *p* films [Fig. 26(b)], the J-V curve has a pronounced "kink" and the dark and light J-V curves "cross-over" in forward bias; the fill factor is low 0.487 and the series resistance is high 21.2 ohm cm^2. Type A films result in good characteristics [see Fig. 26(a)]; the fill factor is high 0.558 and the series resistance is low 9.6 ohm cm^2. It is clear that Type A films are better suited for multijunction device application.

Single-junction *n-i-p* cells were fabricated using both Type A and Type B *p* layers. Interestingly, there is no observable difference in cell performance between the two cases for both a-Si:H and a-SiGe:H cells. It may, therefore, be concluded that the Type A *p* layer passes both the single-junction as well as the "tunnel" junction test. Type B film passes the single-junction test but is inadequate for "tunnel" junction application. The results again show that the requirements on the quality of the *p* layer for the internal junction in a multijunction cell are more stringent than for the top *p* layer at the *p*/ITO interface.

We should mention that the top junction at *p*/ITO interface is also a "tunnel" junction since ITO is a degenerate n^+ semiconductor. The difference in the requirement for the *p* layer for *p*/ITO top junction and p/n internal junction, therefore, merits some discussion. We have shown[39] that the solar cell characteristics also depend on the properties of the *p*/ITO junction. The junction characteristics can be changed by varying the film properties of the ITO and *p* layers. For the internal junction, a recombination process is considered to be necessary for the electrons to move from the conduction band to the valence band. Phosphorus diffusion from the *n* layer to the *p* layer can also affect the junction characteristics significantly. The difference in behavior between *p*/ITO and *p*/*n* junction suggests the possibility of intermixing of phosphorus with boron in the *p*-type layer for the latter case. The intermixing is perhaps more serious for the Type B *p*-type films. Such an intermixing can be facilitated if the Type B films are more porous, thereby aiding phosphorous diffusion from the adjacent *n* layer. The higher porosity of Type B films may be attributed to the lower frequency of deposition which is accompanied by enhanced ion bombardment during the deposition process.

Dual-bandgap, double-junction cells employing Type A and Type B *p* films have been fabricated. The results show that the efficiency of the cells incorporating the Type A films is expectedly higher. The difference in efficiency of the corresponding small-area ~ 0.25 cm^2 cells is approximately 6%-8%.

Double-junction and triple-junction small-area devices have been fabricated using the improved internal junction characteristics. The J-V characteristics and Q curve of a small-area ~ 0.25 cm^2 optimized double-junction cell are shown in Fig. 27. The initial efficiency is 12.77%, which is the highest obtained on a 2B machine-fabricated device. The values of J_{sc}, V_{oc}, and FF are 10.8 mA/cm^2, 1.691 V, and 0.699, respectively. The contributions to J_{sc} from the top and bottom cells (see Q curve of Fig. 27) are 10.59 and 10.9 mA/cm^2, respectively, which translates to a total current density of 21.49 mA/cm^2.

The initial J-V characteristics and Q curve of a small-area ~0.82 cm^2 optimized triple-junction cell are shown in Fig. 28. The J_{sc} contribution from the top, middle, and bottom component cells is 7.39, 7.81, and 8.52 mA/cm^2, respectively. The J_{sc} of the device is, therefore, limited by the top cell at 7.39 mA/cm^2. Using the corrected value of J_{sc} of 7.39 mA/cm^2, the corrected efficiency of the triple-junction cell is 13.19%. This is the highest value obtained to date on cells made in the 2B machine and is close to the highest value of 13.7% reported by us on cells made in the LINE machine. The values of V_{oc} and FF are 2.356 V and 0.757, respectively.

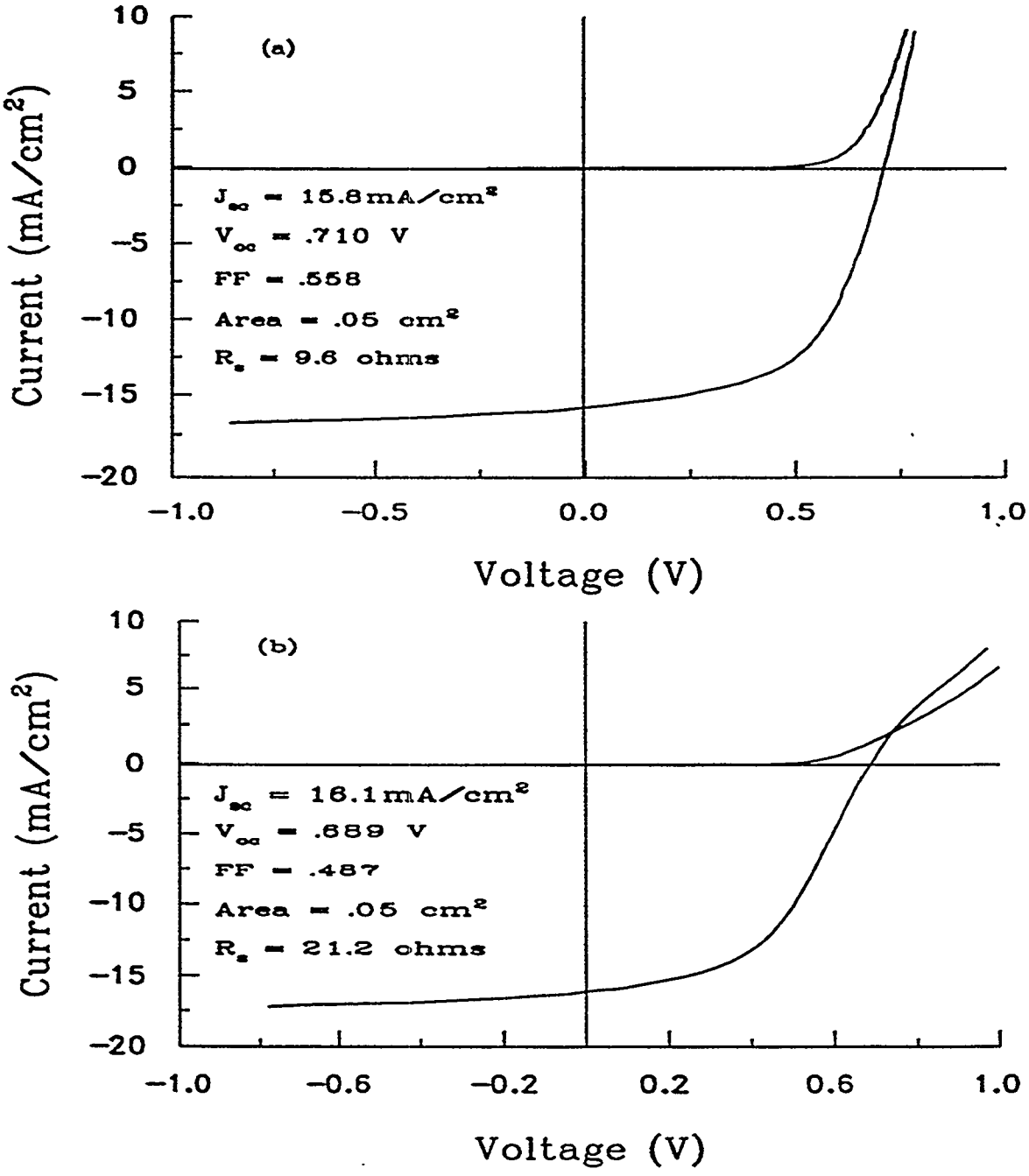

Figure 26. J-V characteristics of NIPN devices using (a) type A films and (b) type B films.

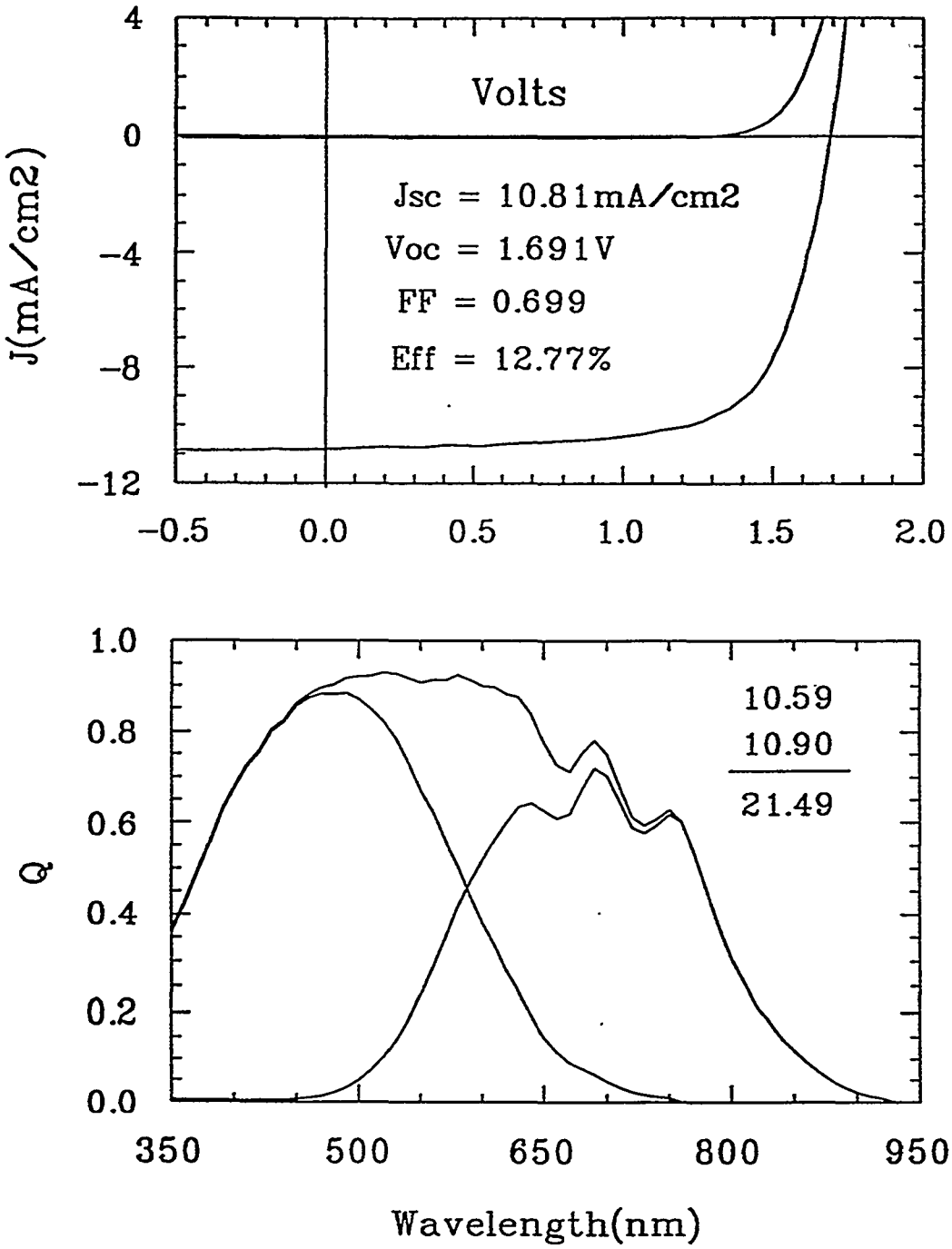

Figure 27. Initial J-V characteristics and Q curve of a double-juncton device.

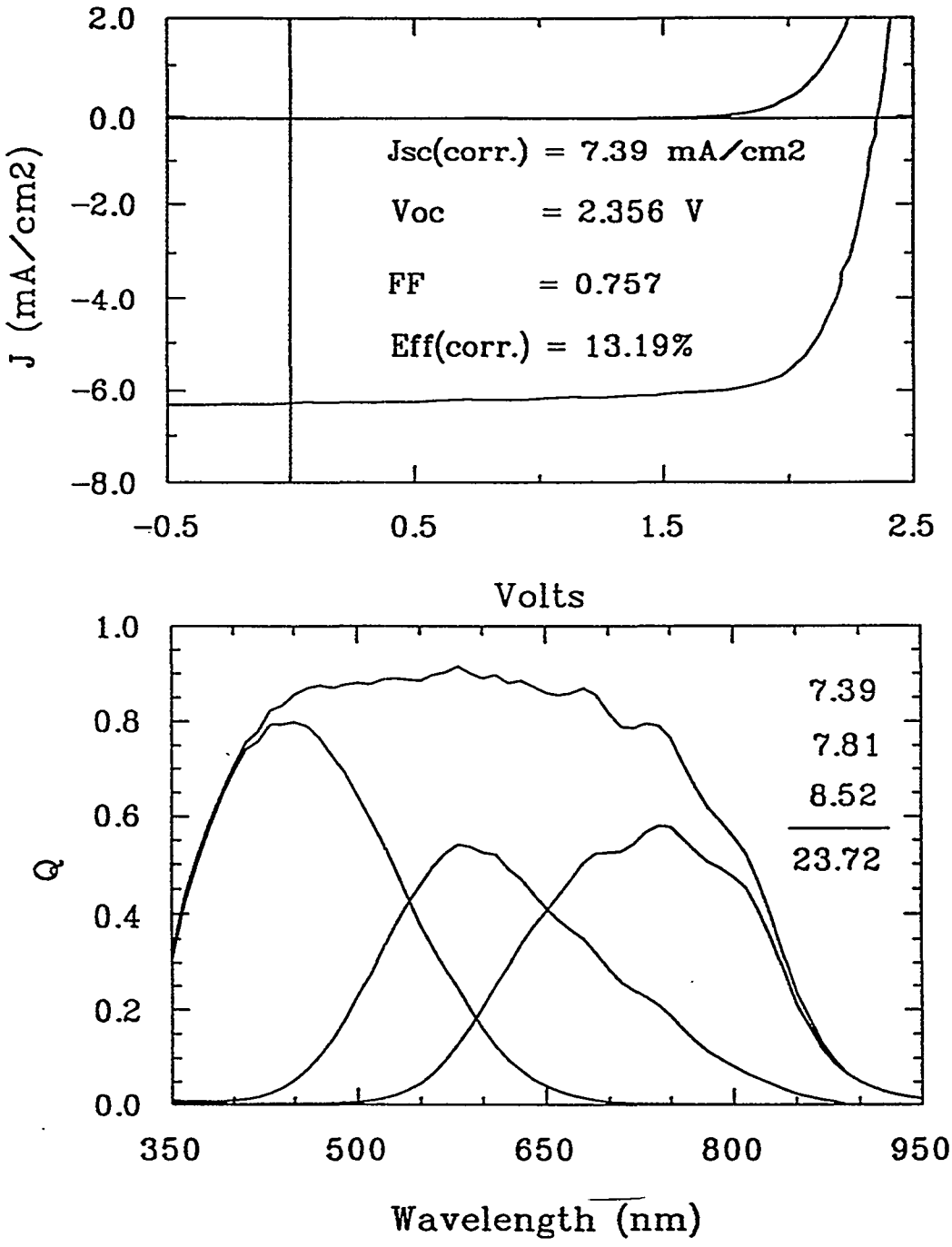

Figure 28. Initial J-V characteristics and Q curve of a triple-juncton device.

Uniformity Studies

In order to obtain high module efficiency, it is important to get good uniformity of the high efficiency devices over the entire module area. The uniformity studies have been carried out by delineating an array of 132 devices arranged in a matrix of 12 x 11 over the 900 cm^2 area and measuring the performance on all the cells. Equal value contour plots of V_{oc}, FF, J_{sc}, and efficiency of a triple-junction device are shown in Figs. 29-32. The efficiency contour plot of the triple-junction cell (see Fig. 32) shows that the nonuniformity over the entire 900 cm^2 area is within 5% between the highest and lowest values. The corresponding contour plots for the double-junction cell are shown in Figs. 33-36.

Module Results

Several double-junction modules have been fabricated. The initial results on four modules as measured by NREL are summarized in Table 16. The indoor measurements were made using a Spire solar simulator Model 240A with a peak detector circuit board. The indoor measurements show that the highest aperture-area initial module efficiency is 11.4%. The outdoor measurements have not been corrected for spectral mismatch, and the small discrepancy between the indoor and outdoor measurements is attributed to this fact.

Table 16. Summary of Initial Double-junction Module Results as Measured by NREL.

Module No.	Aperture Area (cm^2)	V_{oc} (V)	J_{sc} (A)	FF	Efficiency (%)	Outdoor Uncorrected Efficiency (%)
1944	902.9	1.665	9.395	0.634	10.99	10.57
2178	899.9	1.675	9.680	0.633	11.40	10.92
2180	899.9	1.679	9.463	0.643	11.34	10.85
2185	902.9	1.683	9.186	0.666	11.41	10.96

A number of triple-junction modules have been fabricated. Two unexposed modules were sent to NREL for measurement. The NREL results for both indoor and corrected outdoor measurements are summarized in Table 17. The two sets of measurements are in good agreement. The highest initial aperture area efficiency as measured indoors is 11.75%.

The initial double-junction efficiency of 11.4% and the initial triple-junction efficiency of 11.75% correspond to the highest values as confirmed by NREL for any amorphous silicon based photovoltaic module.

The progress in initial module efficiency during the course of the subcontract has been impressive. Figure 37 shows the graph of initial module efficiency as a function of month and year. Modules were fabricated whenever some improvements were made in the processing. The progress attained at various stages has been reported[31,37-41] in journals and conferences.

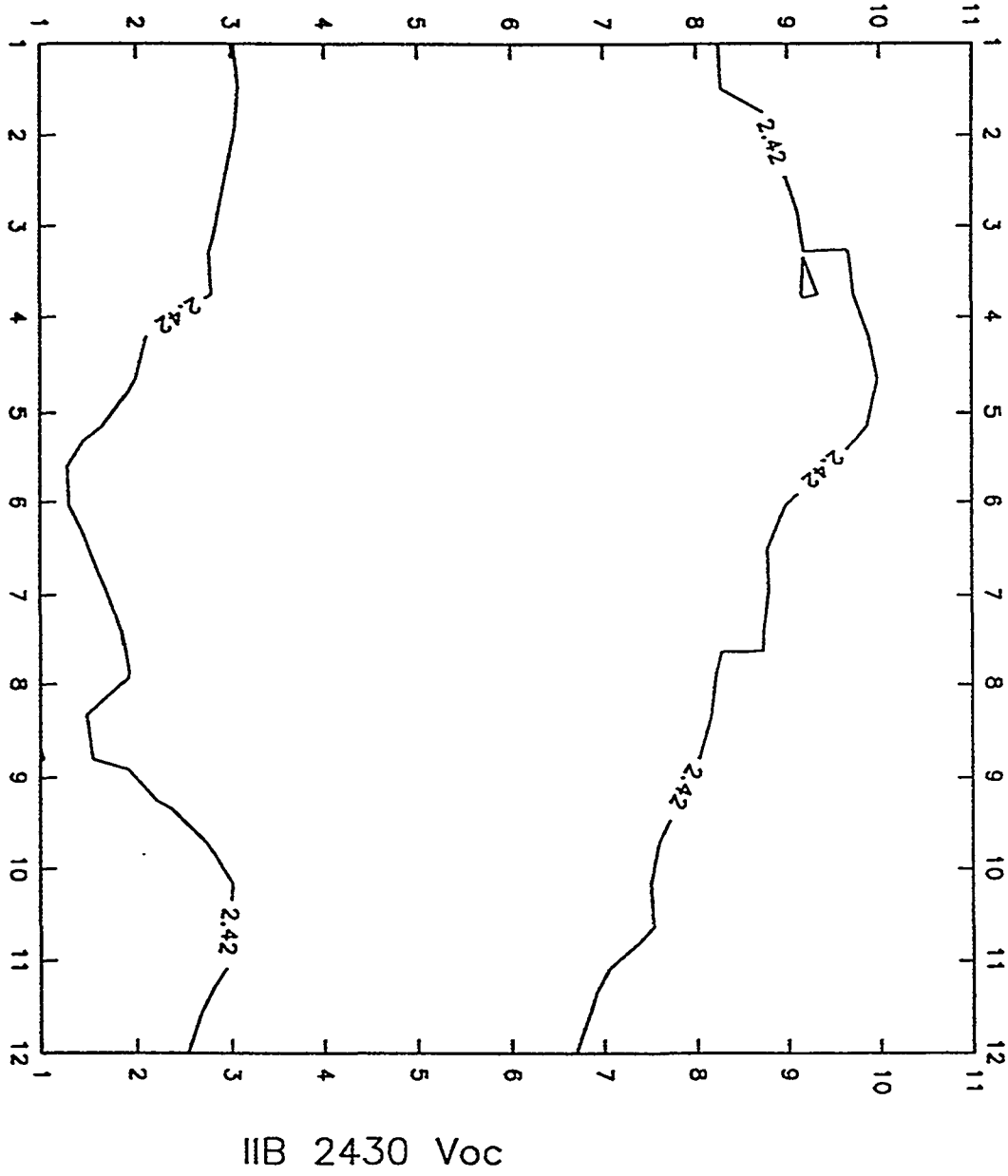

Figure 29. V_{oc} contour plot of a triple-junction cell over 1 ft x 1 ft area.

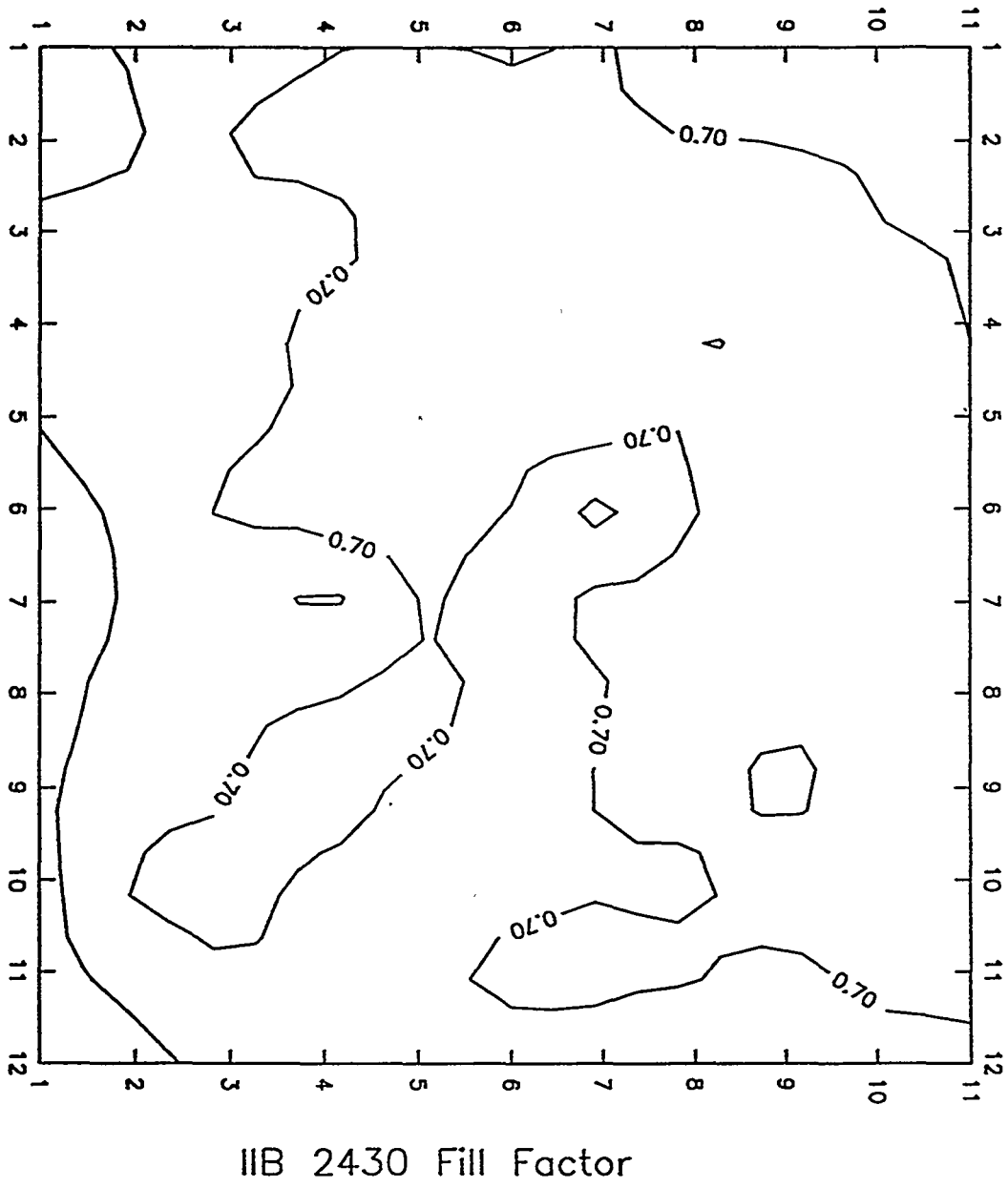

Figure 30. FF contour plot of a triple-junction cell over 1 ft x 1 ft area.

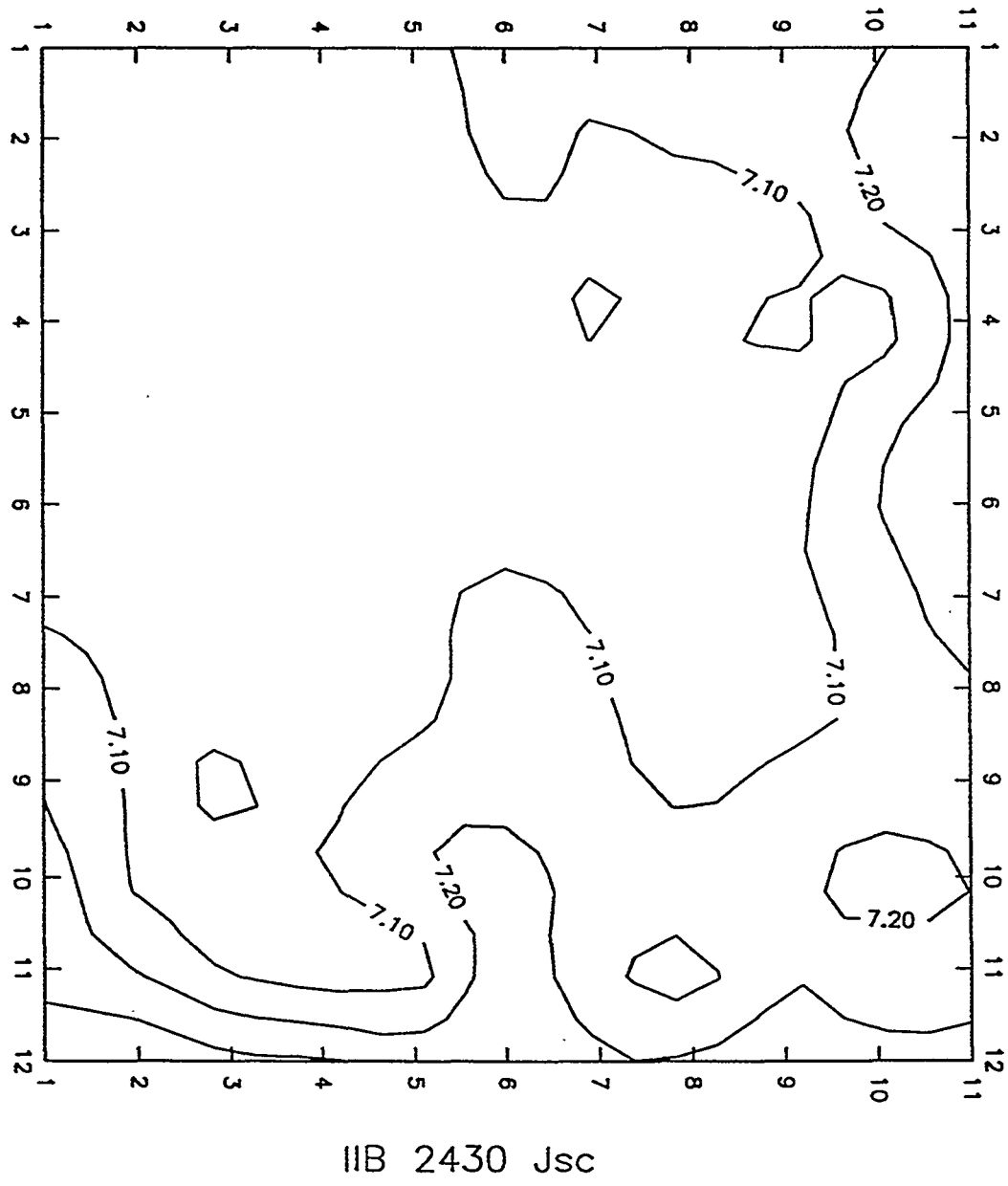

Figure 31. J_{sc} contour plot of a triple-junction cell over 1 ft x 1 ft area.

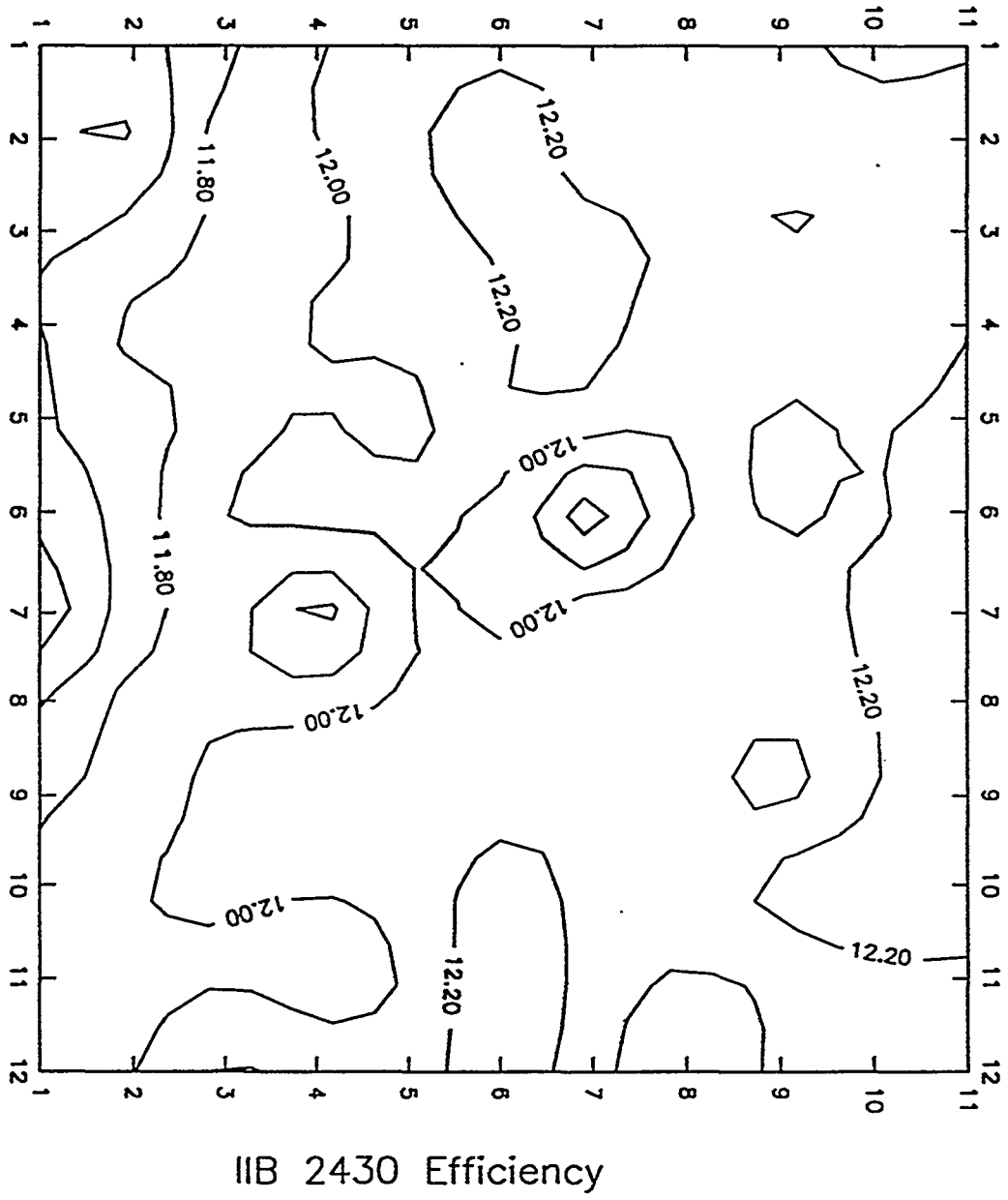

Figure 32. Efficiency contour plot of a triple-junction cell over 1 ft x 1 ft area.

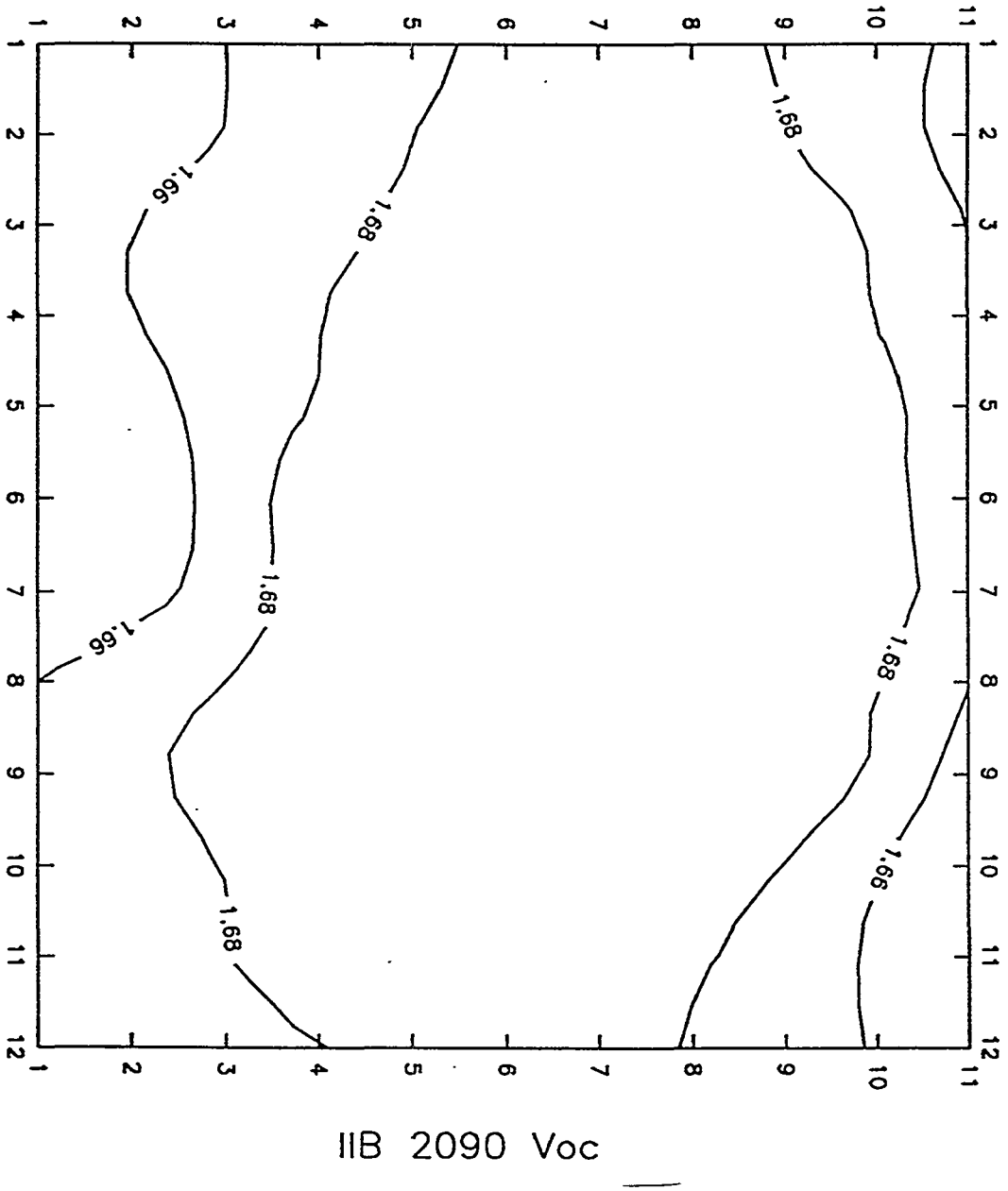

Figure 33. V_{oc} **contour plot of a double-junction cell over 1 ft x 1 ft area.**

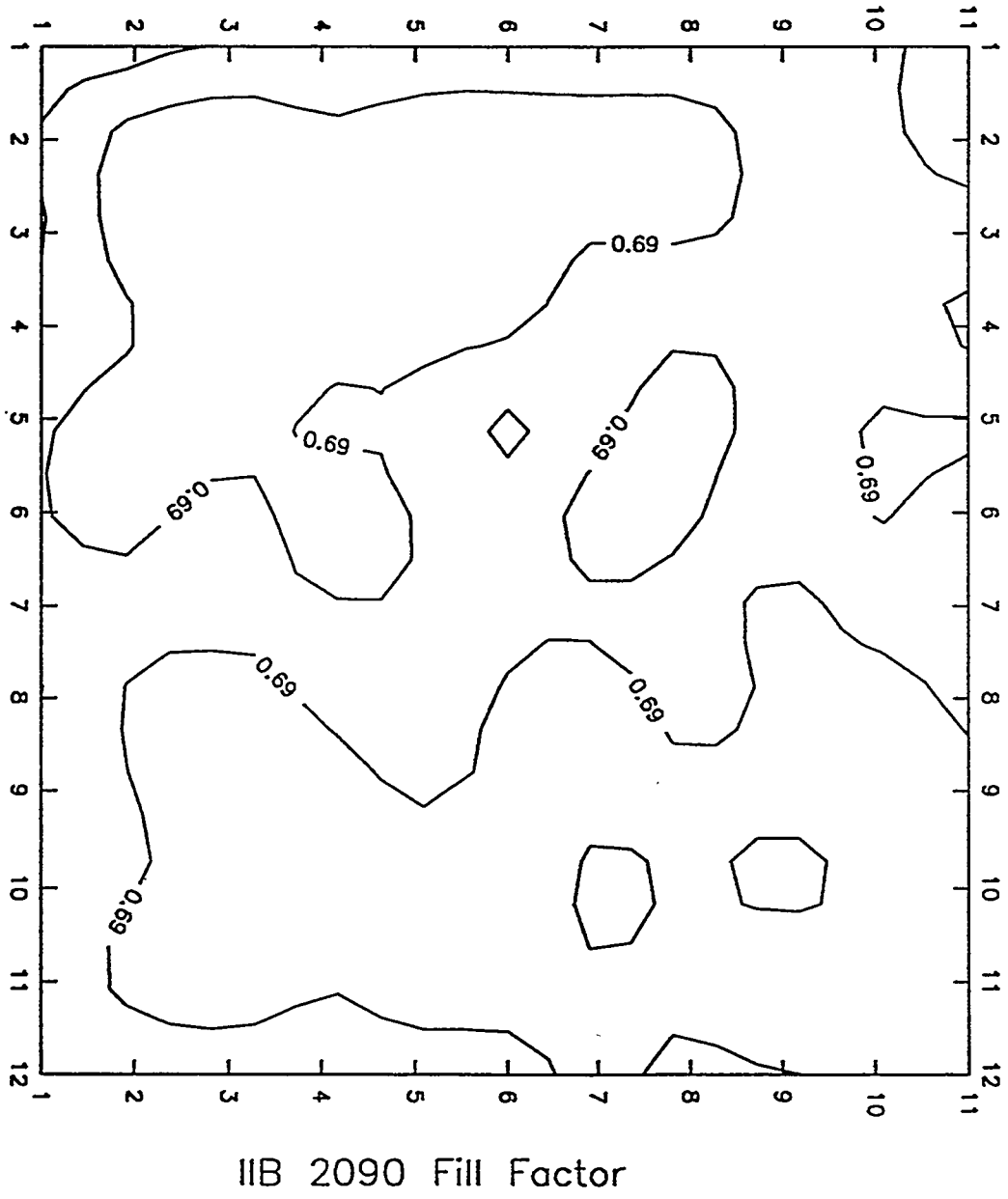

Figure 34. FF contour plot of a double-junction cell over 1 ft x 1 ft area.

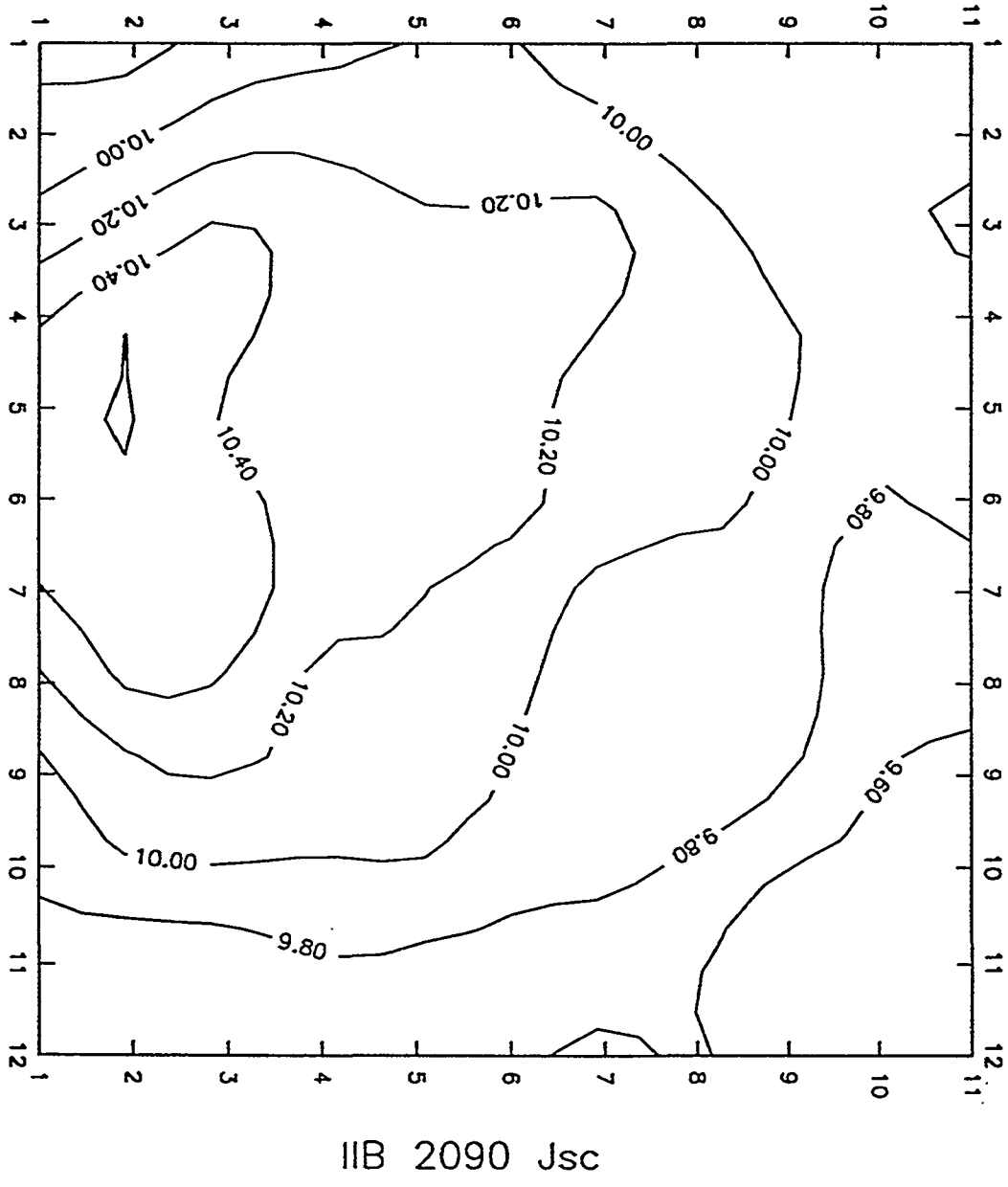

Figure 35. J_{sc} contour plot of a double-junction cell over 1 ft x 1 ft area.

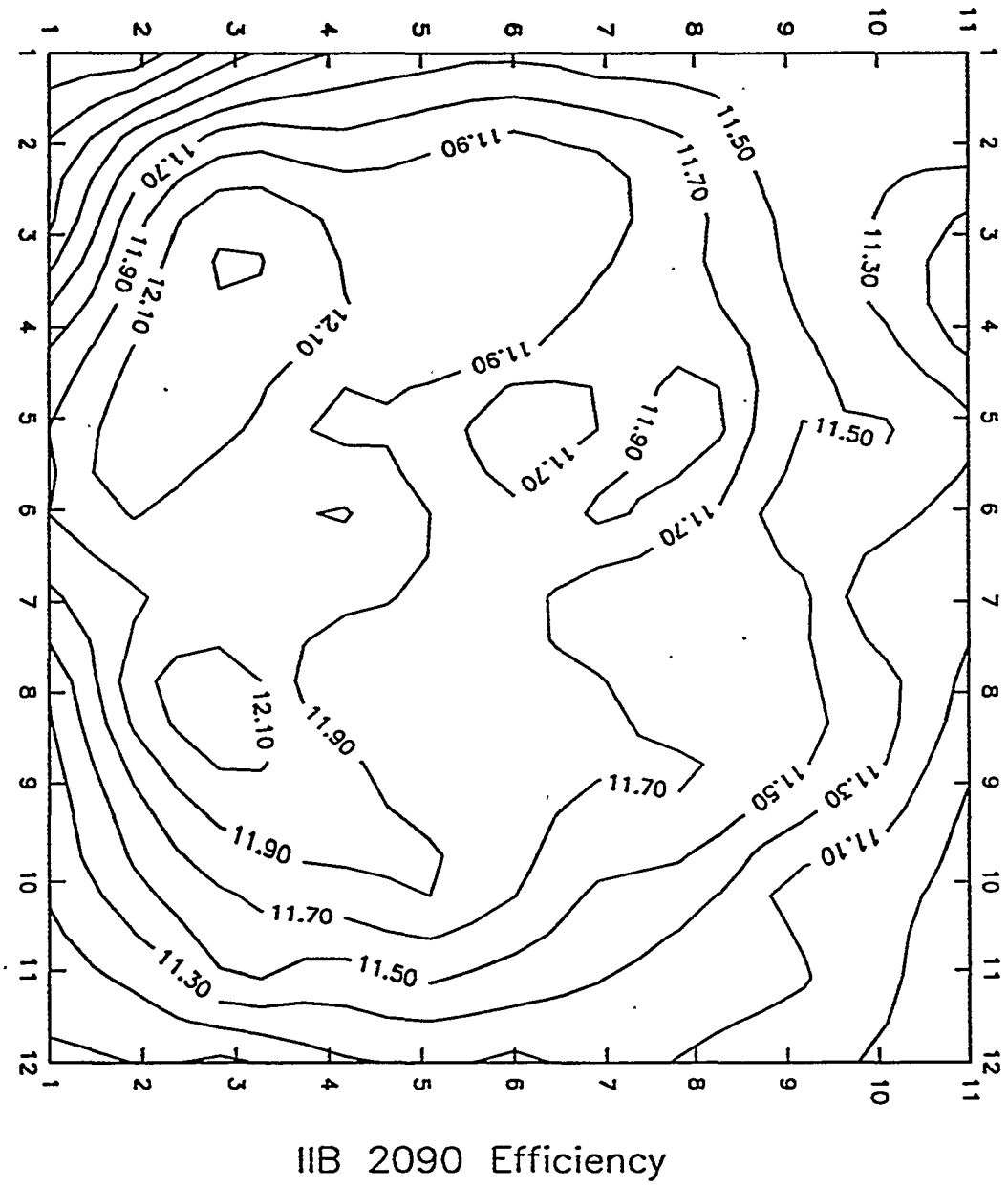

Figure 36. Efficiency contour plot of a double-junction cell over 1 ft x 1 ft area.

Table 17. Summary of Triple-junction Module Results as Measured by NREL.

Module No.	Exposure Condition	Aperture Area (cm^2)	V_{oc} (V)	J_{sc} (A)	FF	Efficiency (%)	Outdoor Corrected Efficiency (%)
2452	Unexposed (Initial)	905.9	2.400	6.568	0.675	11.75	11.6
2465	Unexposed (Initial)	902.9	2.395	6.757	0.652	11.69	11.9
2437	1000 hours (Stabilized)	902.9	2.354	6.196	0.629	10.16	10.4
2445	1000 hours (Stabilized)	899.9	2.349	6.337	0.607	10.04	10.2
2447	1000 hours (Stabilized)	902.9	2.318	6.470	0.612	10.17	10.3

Module Stability

Both the double-junction and triple-junction modules have been subjected to light-induced degradation under one-sun, 50 °C, and maximum power point loaded conditions for 1000 hours. the efficiency versus exposure time for the double-junction module is shown in Fig. 38. The initial efficiency was ~11.1%. The module exhibits saturation at an efficiency of 9.5%.

Three triple-junction modules (Nos. 2437, 2445, and 2447) light soaked for 1000 hours were sent to NREL for measurements. The indoor and corrected outdoor measurements at NREL are summarized in Table 17. Both sets of measurements are in good agreement. All three modules exhibit a stabilized indoor efficiency greater than 10%. The highest saturated efficiency is 10.17%. These are the highest values of stabilized efficiency for any amorphous silicon based module as confirmed by NREL.

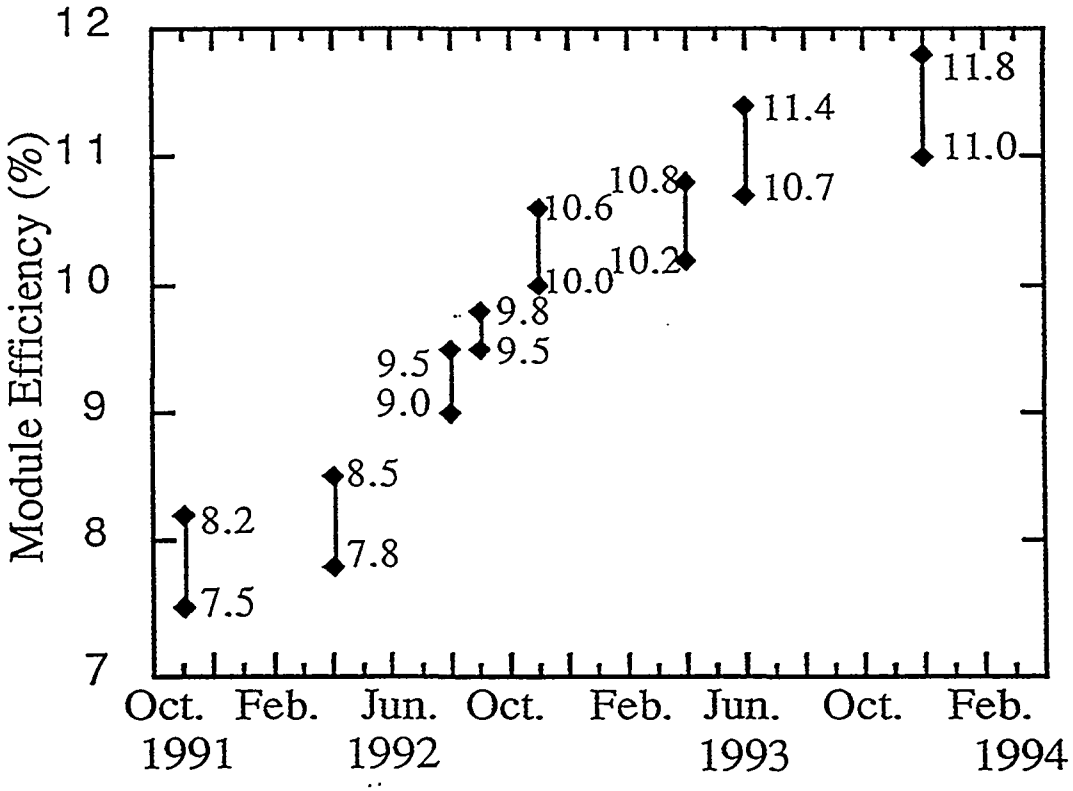

Figure 37. Initial module efficiency as a function of month and year.

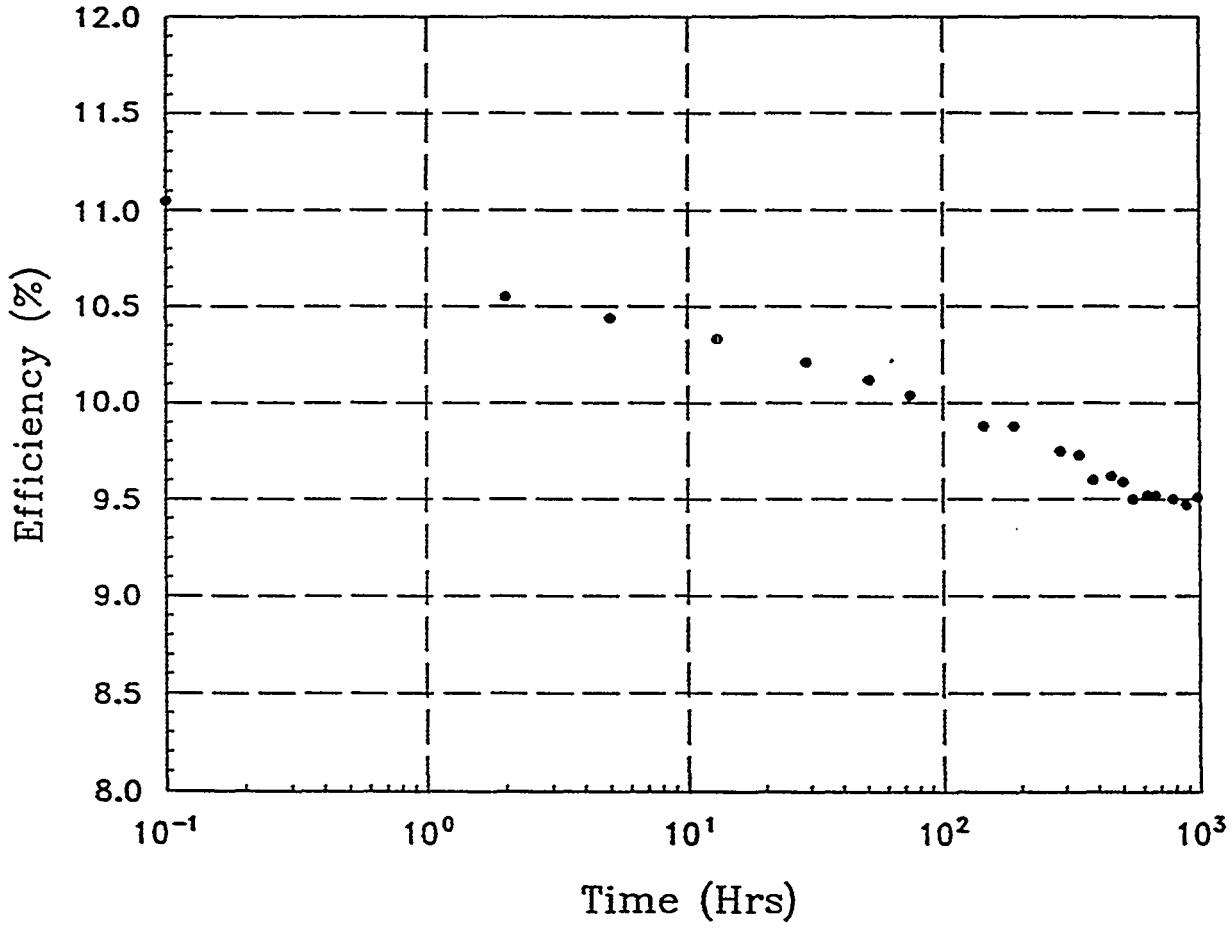

Figure 38. Double-junction module efficiency as a function of one-sun exposure time.

Module Reliability Studies

We have recently made substantial improvements in the reliability of the square-foot modules. These improvements were realized by several process-related modifications in the module fabrication procedures. We previously had observed large degradation after thermal cycling of these modules. On some occasions, module degradation was observed for modules left in the dark under ambient room conditions.

Table 18 shows the module I-V parameters before and after 50 thermal cycles and subsequently 20 humidity-freeze cycles. As can be seen, there was no degradation after 50 thermal cycles and only 2-3% degradation after 20 humidity-freeze cycles. The integrity of the lamination was uncompromised as determined from visual inspection.

Table 18. The J-V Parameters for Two Modules Measured before and after 50 Thermal Cycles and 20 Humidity Freeze Cycles.

	V_{oc}	I_{sc}	FF	P_{max}
Sample A				
Initial	1.71	6.22	.624	6.64
50 TC	1.73	6.11	.631	6.67
Change (% of initial)	+1.2	-1.8	+1.1	+0.5
20 HF	1.73	6.07	.616	6.47
Change (% of initial)	+1.2	-2.4	-1.3	-2.6
Sample B				
Initial	1.71	6.26	.617	6.60
50 TC	1.72	6.15	.620	6.56
Change (% of initial)	+0.6	-1.8	+0.5	-0.6
20 HF	1.72	6.11	.609	6.40
Change (% of Initial)	+0.6	-2.4	-1.3	-3.0

Section 5

Outdoor Efficiency Measurement

We have performed an analysis comparing module efficiency measurements made under a Spire 240A pulsed simulator and outdoors under prevailing conditions. These outdoor conditions were uncorrected for spectrum or temperature and used a global pyronometer to evaluate the total input irradiance. The indoor measurements were performed at United Solar and outdoor measurements at NREL. These measurements took place over a 17-month period from spring of 1992 to August 1993.

We had found over this period of time that results evaluated on the Spire simulator showed significant and steady progress in module efficiency [Fig. 37]. At the same time, the efficiency measured on the same set of modules outdoors did not necessarily correlate with the indoor measurement, and, in fact, showed very erratic progress [Fig. 39]. Furthermore, we found that the two measurements agreed quite well in the summer and disagreed considerably in the winter. During one six-month period, the panel efficiency increased by 10% on the simulator, while the outdoor measurement showed no difference at all.

Figure 40 shows a graph of the ratio of the module efficiency measured outdoors to module efficiency measured indoors plotted versus calendar time. The squares represent control module #1 which was measured on several occasions and stored in between calendar measurements. The stars represent control sample #2. The solid dots each represent a different test module. It is quite obvious that there is a very large seasonal variation in this ratio. This ratio peaks in August at a value near unity and has a minimum in December with values well below 90%. There was, therefore, a 15% variation in outdoor efficiency measurements with respect to simulator efficiency measurements.

Three possible explanations for the above data were considered. The first is that the Spire simulator measurement was not at all repeatable. After analyzing control sample data measured at United Solar over the same period of time, it was found that the variation in output of these modules was within ± 1% of constant [Fig 41]. Therefore, the Spire simulator was indeed repeatable and was not responsible for the variation.

The second hypothesis was that the test modules were optimized differently for each set of modules. We do not believe this to be the case for two reasons: First, the control samples exhibited the same variation as the test modules, and, secondly, the variation was cyclical with season over this 17-month period.

The last hypothesis was that the outdoor prevailing conditions were fluctuating with season. To test this idea, we analyzed the spectral data measured outdoors at the time of each module measurement. What was found was that there was a large difference between the prevailing spectra and the standard spectrum for many of the measurements. What was needed then was a method to correct the outdoor data for this discrepancy in spectral distribution.

The challenge had now become what was the best correction to apply to these multijunction devices. The multijunction device inherently does not allow for a single correction to be applied. The reasoning for this is that each junction has a different spectral response, and that junction has a voltage operating point that also depends on the other junctions. Hence, even if one particular junction has been corrected properly, the relationship between junctions may result in an incorrect fill factor. This was the basis for developing the multisource spectral approach which enables all junctions to be properly corrected simultaneously. This obviously cannot be performed outdoors and is quite difficult to apply indoors over large areas.

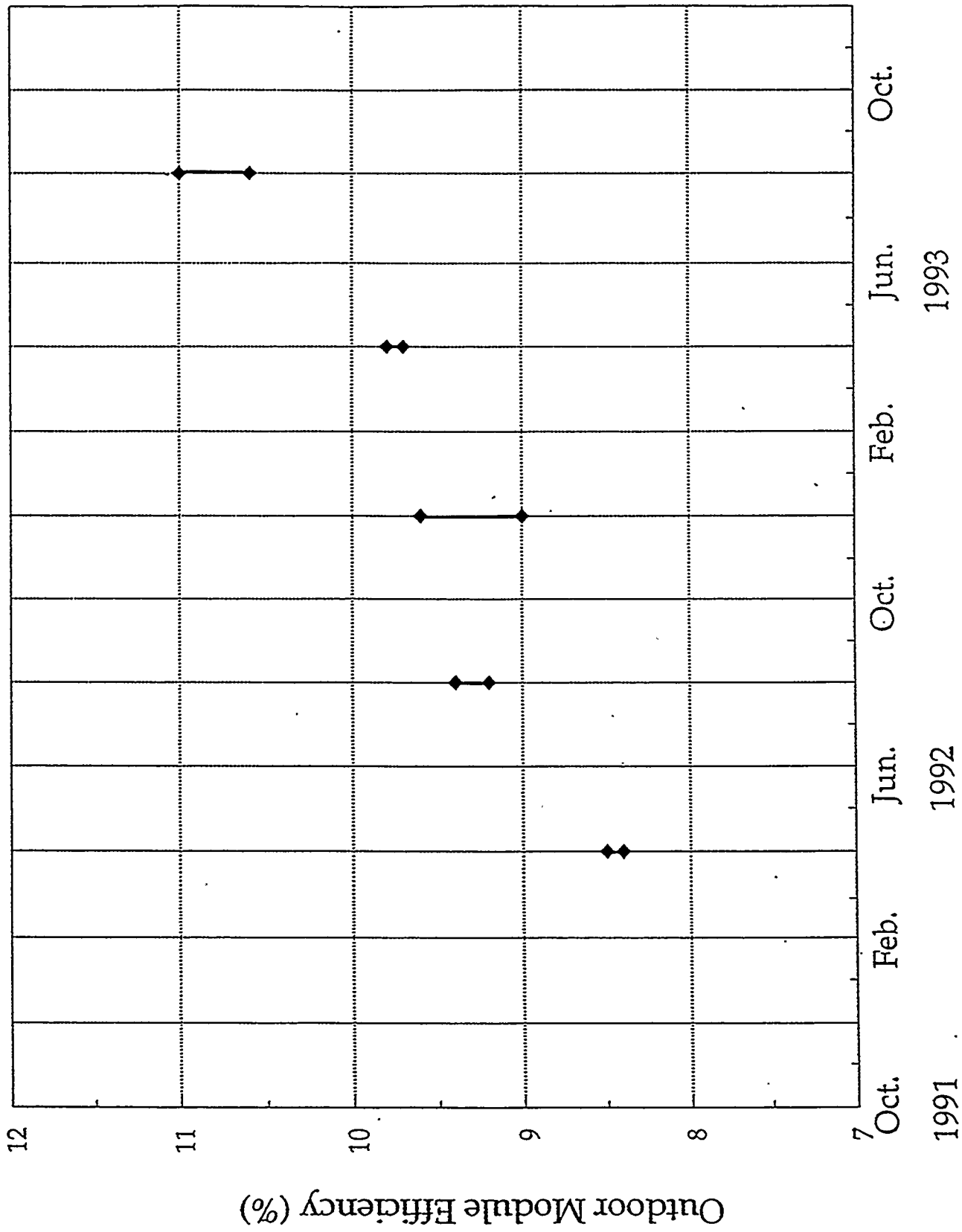

Figure 39. Progress of outdoor initial module efficiency versus time. Bars indicate range of efficiencies for several panels.

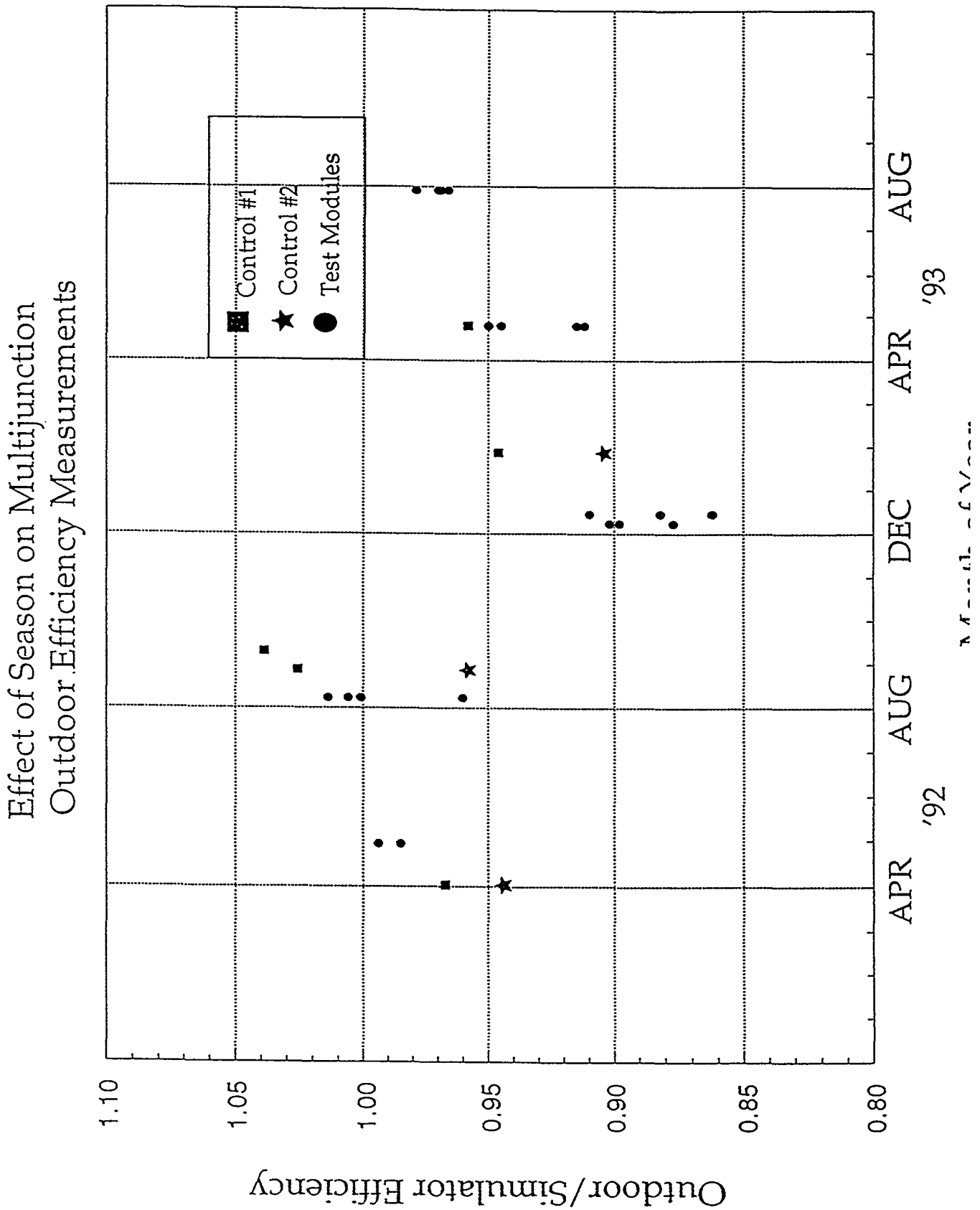

Figure 40. **Plot of the ratio of outdoor to indoor module efficiency versus time of year. Squares represent control sample 1, stars control sample 2, and dots individual test modules.**

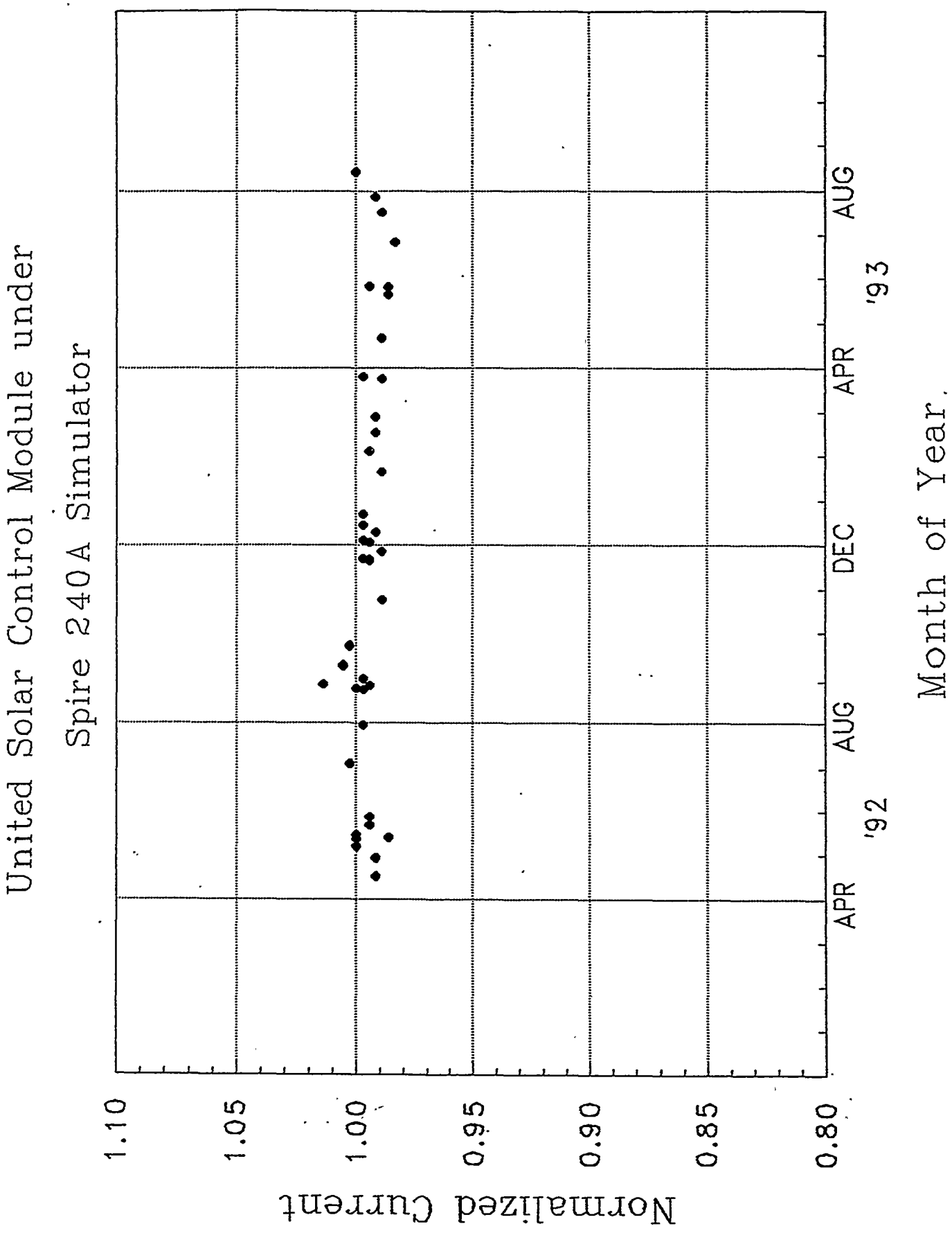

Figure 41. Output of a control module evaluated on the United Solar spire simulator versus time.

The most accurate correction, as we will show, was to apply a spectral mismatch to a single-cell device that most accurately represented the response of the overall multijunction response. This was identified to be a single a-Si:Ge device with a bandgap of approximately 1.5 eV. Figure 42 shows the response of an a-Si:Ge single cell with the envelope of the multijunction response. What this achieved was that the average corrected junction current, under outdoor conditions, would now be equivalent to the average junction current under the standard spectrum. For example, the uncorrected ratio of junction current under prevailing conditions (for a December 1992 data point) to reference conditions was 0.87 and 0.91 for the top and bottom junctions, respectively. The spectral mismatch using the a-Si:Ge single-cell, for this case, was 0.89. If we correct the junction current by this mismatch, we arrive at corrected ratios of 0.98 and 1.02 for top and bottom, respectively. This gives an average for both junctions of 1.00.

It is still apparent that there is a mismatch between the two junctions, in the above example, with respect to the reference spectrum. This junction mismatch, with respect to the reference spectrum, will result in a different fill factor for the multijunction device under the prevailing conditions. Since the quantity of the fill factor difference will be less than the junction mismatch, we would expect the prevailing-conditions fill factor to be well within 2% of the reference fill factor. In fact, based on studies performed on a multisource simulator, the maximum change in fill factor that could be expected was 0.4 percent per percent of mismatch. As was observed, the spectral correction in this example was greater than 10% -- well in excess of the maximum 2% fill factor error. The largest ratio deviation for any point and any junction for the data in Fig. 40 after correction was ± 2.5%. Therefore, the largest error in the outdoor fill factors would be less than 2.5%.

The procedure, then, was to use the spectral irradiance measured at the time of module measurement to evaluate the spectral mismatch. The mismatch was calculated using the pyronometer as the reference device, the a-Si:Ge single-cell as the test device, the prevailing conditions spectrum as the source spectrum and the standard AM 1.5 global spectrum as the reference spectrum. The current obtained outdoors for the module was then divided by this spectral mismatch value, and efficiency subsequently calculated with this adjusted current.

In Fig. 43, we show the same plot as in Fig. 40 with the spectral correction also plotted. The control samples were not included in this graph because spectral data could not be obtained for these points. The solid circles are the "as-measured" ratios, and the open circles are the ratios corrected for the outdoor spectral data. It is quite apparent that these corrections have completely eliminated any seasonal variation in this comparison. The largest correction in this data of 12% was made in December, while the smallest correction was a small negative correction in the summer data.

There were still two questions to be answered. The first was why is the correction factor for the prevailing conditions so large and what was it due to? The second question was if using the pyronometer produces such a large correction, what would be the best reference cell to use in order to minimize this correction?

In order to properly evaluate the spectral considerations, it was first necessary to expand the wavelength range of the spectral irradiance. The spectrum was obtained using a silicon-based spectral radiometer. This meant that actual data was only obtained for a wavelength range of 300-1100 nm. The desired range for the pyronometer is from 300 to 2500 nm. To achieve this range, we fit the measured data to an atmospheric spectral model. This is a valid procedure since all parameters in the model may be obtained from the experimental data. This allowed us to calculate a spectral mismatch factor involving a pyronometer which has a response range to 2 microns. Figure 44 shows the quality of the modeled to measured fit.

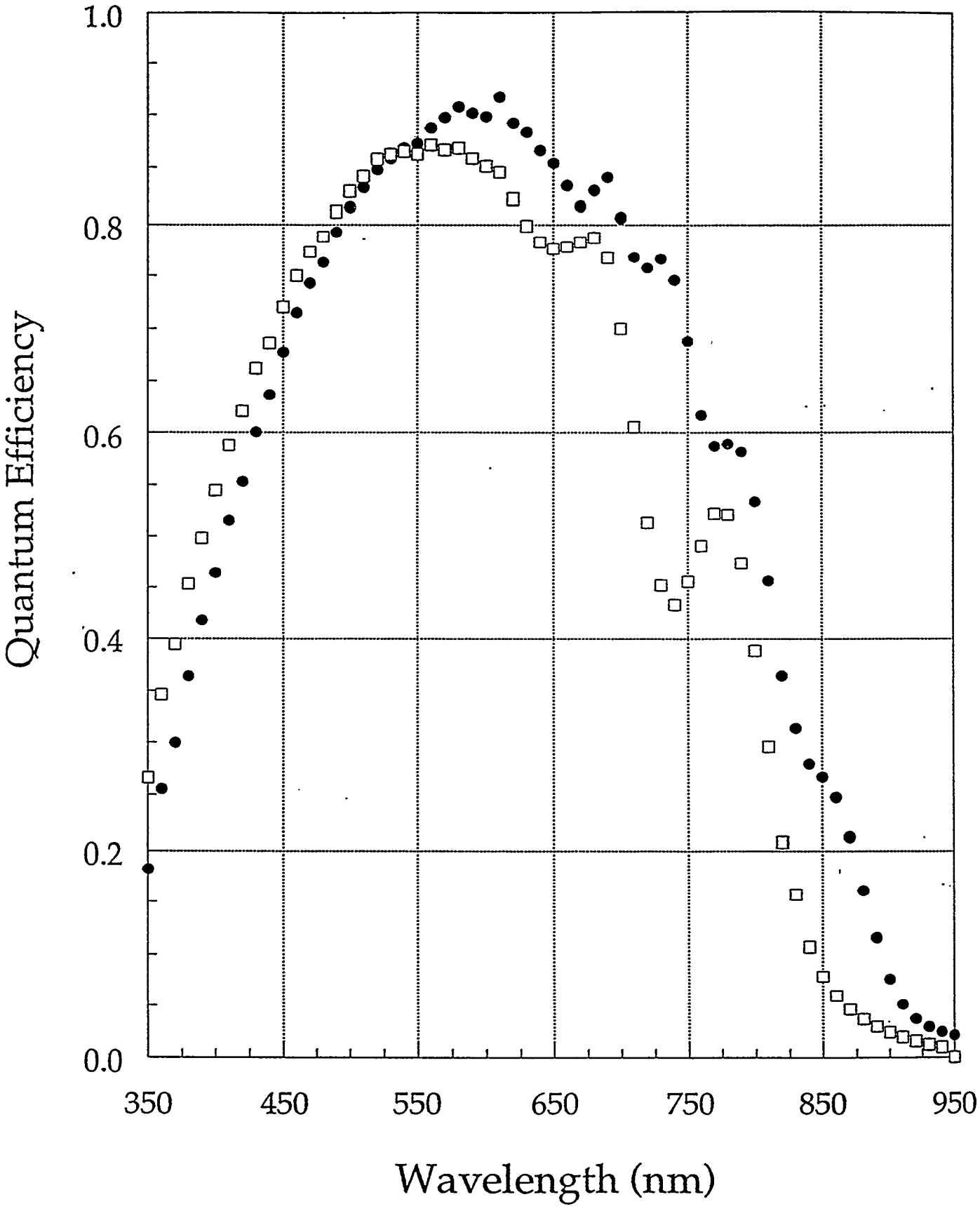

Figure 42. Comparison of the quantum efficiency of a single a-Si:Ge device (□) used in spectral mismatch calculation to the envelope a double junction device (●).

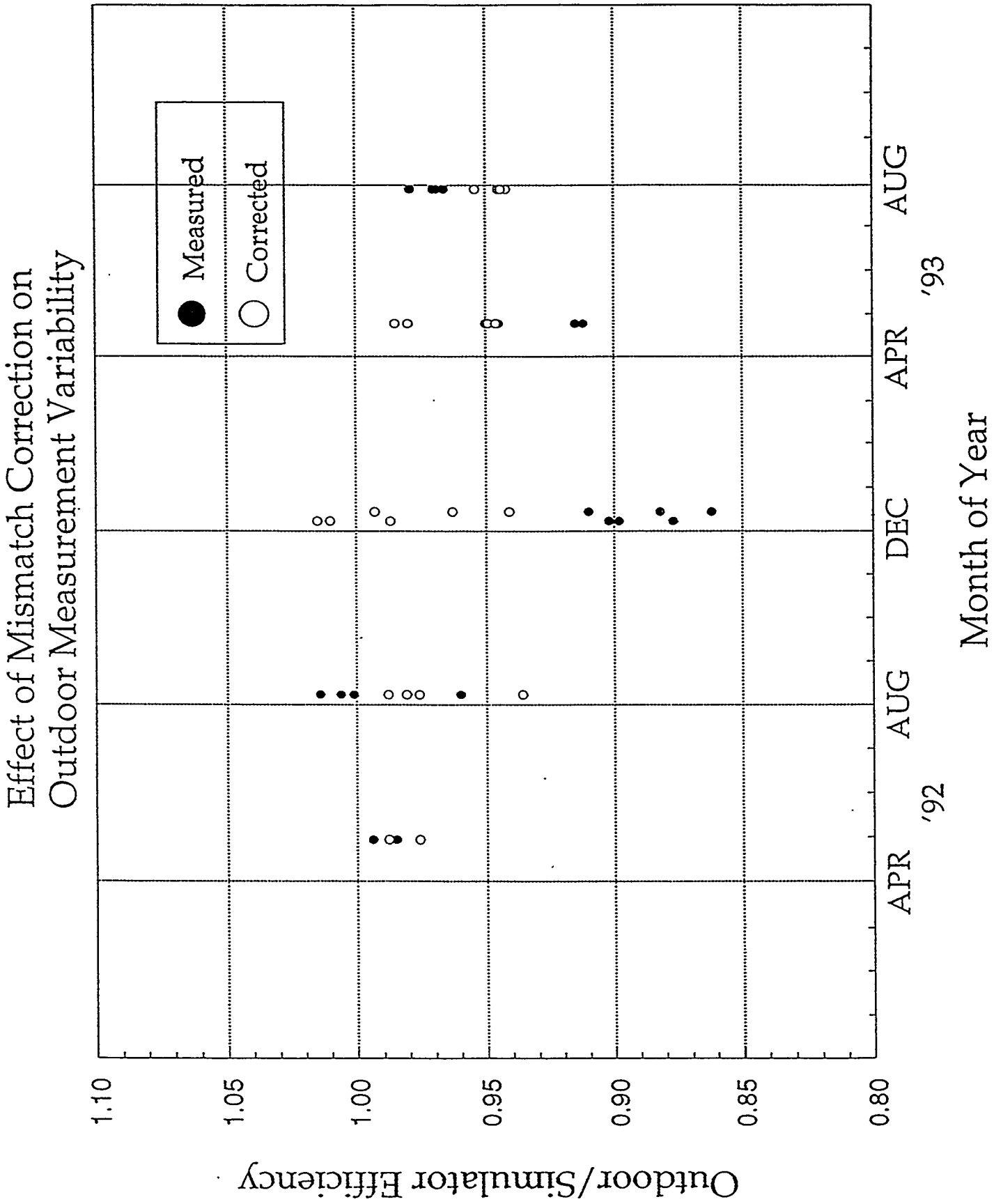

Figure 43. Plot of the ratio of outdoor to indoor module efficiency versus time of year. Solid dots represent as measured, and open dots represent spectral corrected outdoor measurements.

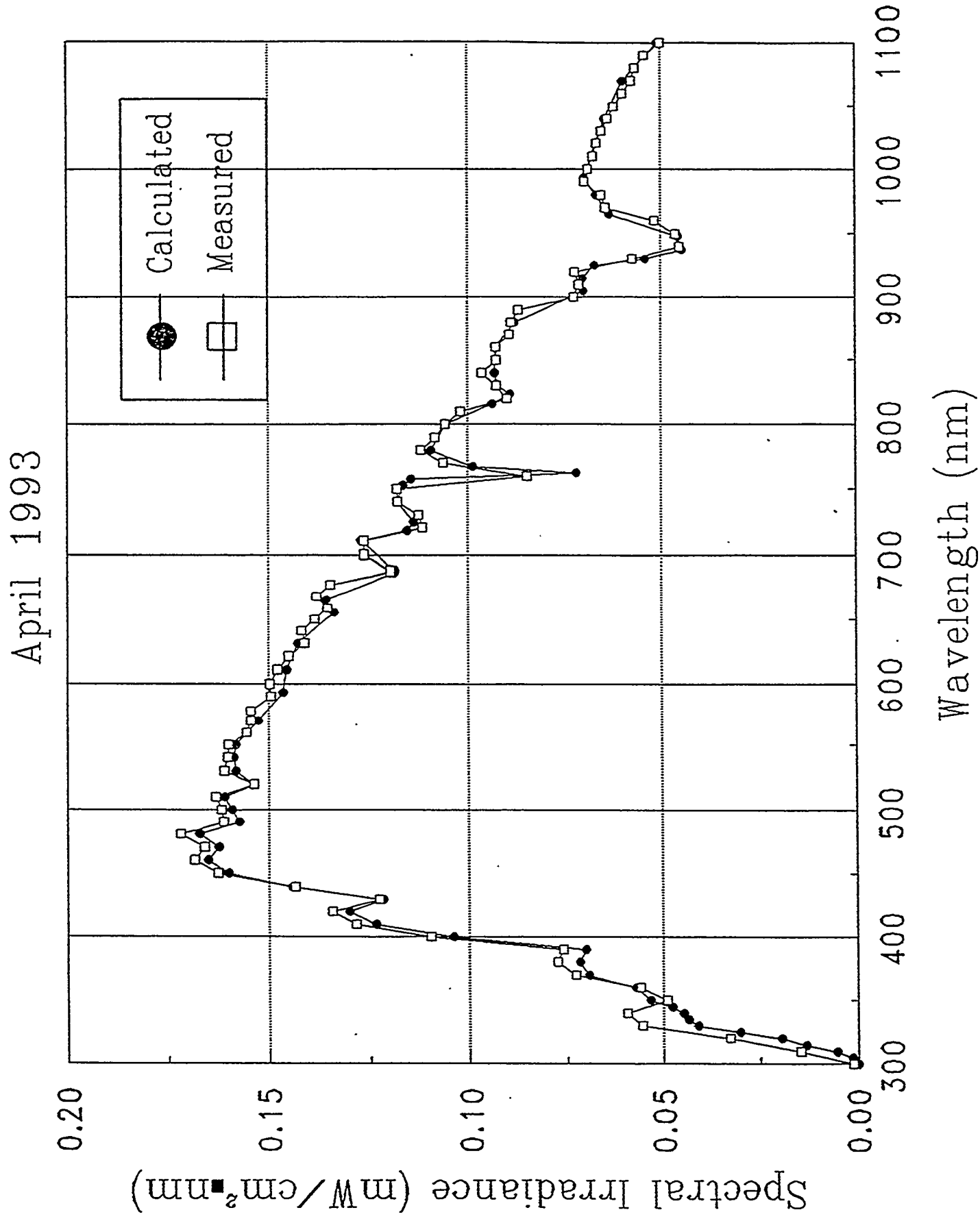

Figure 44. Comparison of the measured and curve fit spectral irradiance measured outdoors.

Figure 45 shows a plot of the standard spectrum and the prevailing spectrum taken in April of 1992. This spectrum produced a correction factor of only 1%. It is apparent that the prevailing spectrum is a good match to the standard spectrum in this case. Figure 46 shows a plot of the standard spectrum and the prevailing spectrum taken in December of 1992. This spectrum produced a large correction factor of 12%. It is also apparent that the prevailing spectrum is a poor match to the standard spectrum primarily in the infrared portion of the spectrum. This difference is due to water vapor absorption bands and not a difference in air mass. Since these absorption bands appear only in the infrared, the pyronometer sees an additional 9% irradiance level over that of the standard spectrum, whereas the a-Si module, since it responds only to the visible, sees almost no difference between the prevailing and standard spectra. This results in a greatly underestimated efficiency for the a-Si module with respect to the global standard spectrum.

Returning to the second question, what reference device should be used in place of the pyronometer to reduce this large spectral mismatch error? To investigate this we tried five different cases, the results of which are displayed in Table 19. In each of these cases, we applied the mismatch correction to the outdoor data and calculated the mean and standard deviation for the outdoor/indoor ratio over the entire time period. The first, labeled pyronometer, was to apply no mismatch to the outdoor data of Fig. 40 (uncorrected) and use a pyronometer as the reference detector. This resulted in the average ratio of outdoor to indoor efficiency, over this time period, being 0.945 with a large standard deviation of 5.0%. The second case, labeled x-Si, was again applying no mismatch and using a x-Si module as a reference device. This resulted in a mean of the outdoor to indoor ratio of 0.942 with a larger deviation of 5.7%. The third case, labeled a-Si single, was to correct the outdoor efficiency by the spectral mismatch between the pyronometer and a single a-Si device. The mean ratio for this case was 0.970 with an improved deviation of 3.0%. The next case was to correct the outdoor measurement by the mismatch between the pyronometer and a single a-SiGe device. This turned out to give the smallest standard deviation of 2.1% in the ratio, while the mean was 0.970. In the final case, we adjusted the outdoor measurement by the mismatch between the pyronometer and the top cell of a double-junction device. This would have the effect, since the top cell typically limits, of only correcting for the multijunction current. This resulted in a higher deviation of 4.3% as compared to 2.1% using a single a-SiGe device.

Table 19. Effect of Reference Device on Outdoor Efficiency Correction.

Reference Cell Type	Mean	Deviation
Pyronometer	0.945	5.0%
x-Si	0.942	5.7%
a-Si single	0.970	3.0%
a-SiGe single	0.970	2.1%
a-Si top tandem cell	0.961	4.3%

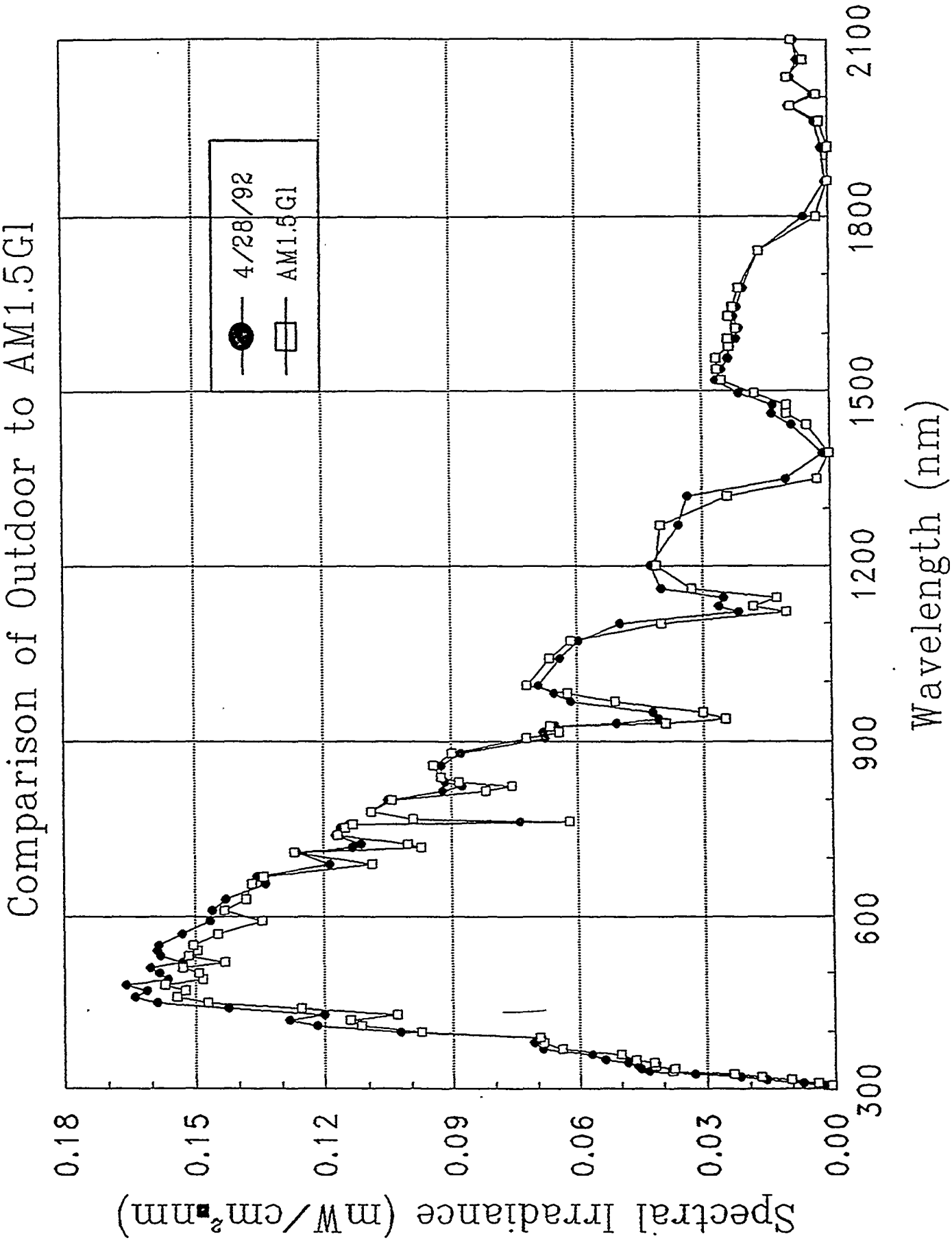

Figure 45. Plot of the standard spectrum and the prevailing spectrum taken in April of 1992.

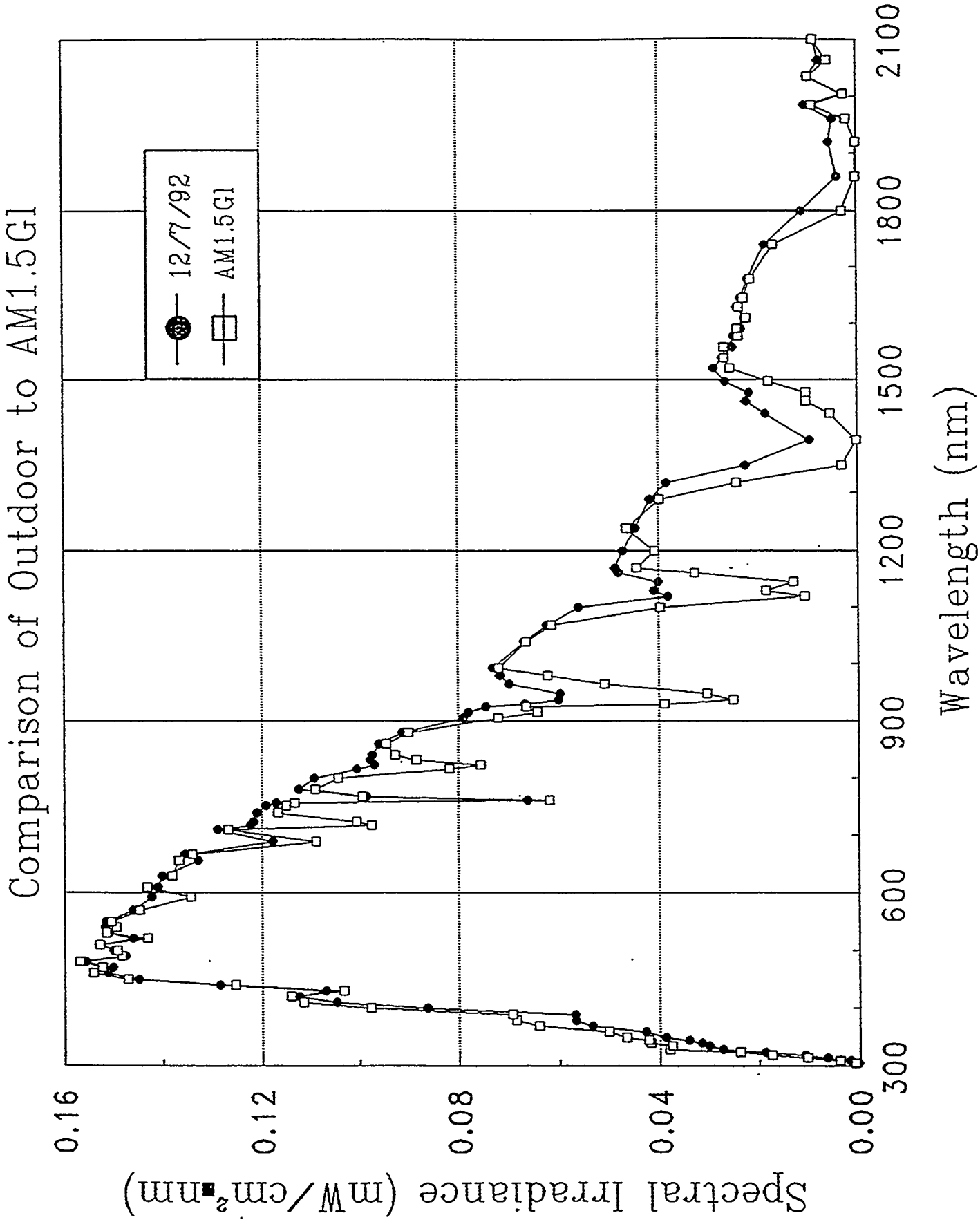

Figure 46. Plot of the standard spectrum and the prevailing spectrum taken in December of 1992.

We therefore found, from our spectral analysis, that the most appropriate reference device to evaluate the total irradiance would be an a-SiGe cell with a bandgap of about 1.5 eV. This device best matches the overall response of the multijunction module as can be seen from Fig. 42. We found that by using this device, we were able to reduce the scatter in the outdoor measurement from a standard deviation of ± 5% for the pyronometer to just ± 2% for the a-SiGe cell. In other words, if an a-SiGe reference device had been used to determine the original total input irradiance instead of the pyronometer, there would have been no need to correct the outdoor data in the first place.

In conclusion, we found by applying spectral mismatch corrections to outdoor efficiency measurements, we were able to reduce the standard deviation in those measurements from ± 5% to ± 2% for a-Si based multijunction modules. We also found the maximum range of spectral corrections applied to the outdoor modules efficiencies was + 12.5% for the December measurements to - 2.6% for the August measurements. Most of this correction was simply due to insufficient water vapor absorption in the prevailing spectra. We believe that it is vital that this correction procedure be applied to outdoor measurements since it both reduces the deviation significantly and is the most accurate method to date for measuring multijunction modules outdoors.

As we have discussed above, possible errors involved in outdoor module measurements without spectral correction can be large. We did a spectral correction calculation using actual outdoor spectra provided by NREL and arrived at a corrected stabilized efficiency of 10.3% for our modules.

Recently, NREL also applied spectral correction calculations (see attached memo) and obtained stabilized efficiency for Modules #2437, #2445, and #2447. It is remarkable that the corrected efficiency for indoor (using Spire) and outdoor (on three different days) all lie between 10.1% to 10.4%. In addition, the two undegraded modules also exhibit corrected indoor and outdoor efficiencies of nearly 12%, the highest reported initial efficiency for any thin film module confirmed by NREL.

To: W. Luft
From: Keith Emery
Date: Feburary 17, 1994
Subject: Spectral error calcuations for test report #9420

This memo documents the spectral analysis that I performed on the USSC record module data.

sample	date/time	Isc (A)		efficiency (%)		M top	M mid	Mbot
		as is	corrected	as is	corrected assuming top cell limited			
2437	12/22/93 Spire	6.196	6.25	10.2	10.3	0.991	1.035	1.148
	1/10/94 13:25	5.394	5.93	9.23	10.2	0.909	0.959	1.000
	1/12/94 12:04	5.492	5.91	9.62	10.4	0.929	0.961	0.991
2b2445	12/22/93 Spire	6.470	6.40	10.0	10.1	0.991	1.035	1.148
	1/10/94 13:38	5.439	6.04	9.17	10.2	0.900	0.958	1.004
	1/12/94 11:42	5.658	6.09	9.48	10.2	0.929	0.961	1.008
2b2447	12/22/93 Spire	6.470	6.53	10.2	10.3	0.991	1.035	1.148
	12/29/93 11:53	5.927	6.34	9.55	10.2	0.935	0.975	1.001
	1/10/94 13:28	5.894	6.51	9.36	10.3	0.906	0.959	1.002
	1/12/94 11:58	5.942	6.41	9.56	10.3	0.927	0.961	0.992
2452	12/22/93 Spire	6.470	6.63	11.8	11.9	0.991	1.035	1.148
	1/10/94 12:43	5.654	6.09	10.4	11.2	0.929	0.961	0.992
	1/12/94 11:32	5.905	6.36	10.8	11.6	0.928	0.962	0.993
2465	12/22/93 Spire	6.470	6.81	11.7	11.8	0.991	1.035	1.148
	1/10/94 13:33	5.887	6.53	10.7	11.9	0.901	0.959	1.003
	1/12/94 11:49	5.977	6.43	10.9	11.7	0.929	0.961	1.008

Section 6

Conclusions and Future Directions

During the program, significant advances have been made in obtaining higher efficiency in multibandgap, multijunction modules. A large number of one-square-foot modules have been fabricated with initial efficiencies exceeding 11%. **The highest initial efficiency reached is 11.8%, as confirmed by NREL. This is the highest efficiency confirmed by NREL for any thin film module.** The improvement in efficiency has been obtained through a combination of i) optimization of the individual intrinsic layers, ii) reduction in the losses at the "tunnel" junction, iii) lowering the grid and encapsulation losses and iv) better uniformity of the deposited layers over one-square-foot area.

The highest stabilized efficiency of the triple-junction modules obtained to date after light soaking for 1000 h is 10.2%. We have shown earlier that triple-junction cells not only have higher initial efficiency, but they have better stability too. High hydrogen dilution has been shown to improve component cell performance in both the initial and light-soaked states. Further understanding of growth kinetics and role of impurities as well as optimization of deposition conditions should lead to even higher stabilized module efficiencies.

References

1. K. Hoffman and T. Glatfelter, Proceedings of 23rd IEEE Photovoltaics Specialists Conference, 986 (1993).

2. S. Guha, Annual Report, ZM-1-19033-2 (National Renewable Energy Laboratory, Golden, CO, 1993).

3. A. Smith, A. Rohatgi, and S. Neel, Proceedings of 21st IEEE Photovoltaic Specialists Conference, 426 (1990).

4. E. Yablonovitch and G. Cody IEEE Trans. Ed-**29**, 300 (1982).

5. T. Sawada, H. Tarui, N. Terada, M. Tanaka, T. Takahama, S. Tsuda, and S. Nakano, Proceedings of 23rd IEEE Photovoltaics Specialists Conference, 803 (1993).

6. A. Banerjee and S. Guha, J. Appl. Phys. **69** (2), 1030 (1991).

7. For recent publications on this subject, see *Amorphous Silicon Materials and Solar Cells*, edited by B. L. Stafford (American Institute of Physics Conf. Proc. 234, New York, 1991).

8. S. Guha, J. Yang, W. Czubatyj, S. J. Hudgens, and M. Hack, Appl. Phys. Lett. **42**, 588 (1983).

9. C. R. Wronski and N. Maley, in *Amorphous Silicon Materials and Solar Cells*, edited by B. L. Stafford (American Institute of Physics Conf. Proc. 234, New York, 1991), p. 11.

10. D. L. Williamson, A. H. Mahan, B. P. Nelson, and R. S. Crandall, J. Non-cryst. Solids **114**, 226 (1989).

11. A. H. Mahan, D. L. Williamson, B. P. Nelson, and R. S. Crandall, Phys. Rev. B **40**, 12024 (1989).

12. A. H. Mahan, D. L. Williamson, B. P. Nelson, and R. S. Crandall, Solar Cells **27**, 465 (1989).

13. S. Guha, Final Report, SERI/TP-211-3918 (Solar Energy Research Institute, Golden, Colorado, 1990).

14. D. L. Williamson, A. H. Mahan, B. P. Nelson, and R. S. Crandall, Appl. Phys. Lett. **55**, 783 (1989).

15. A. Guinier, *X-ray Diffraction in Crystals, Imperfect Crystals and Amorphous Bodies* (W. H. Freeman, San Francisco, 1963), p. 264.

16. E. Bhattacharya and A. H. Mahan, Appl. Phys. Lett. **52**, 1587 (1988).

17. A. Langford, M. Fleet, B. P. Nelson, W. A. Lanford, and N. Maley, Phys. Rev. B **45**, 13367 (1992).

18. A. Matsuda, S. Mashima, K. Hasezaki, A. Suzuki, S. Yamasaki, and P. J. McElheny, Appl. Phys. Lett. **58**, 2494 (1991).

19. S. Guha, J. Yang, S. J. Jones, Y. Chen, and D. L. Williamson, Appl. Phys. Lett. **61**, 1444 (1992).

20. S. J. Jones, Y. Chen, D. L. Williamson, R. Zedlitz, and G. Bauer, Appl. Phys. Lett. **62**, 3267 (1993).

21. S. J. Jones, Y. Chen, D. L. Williamson, X. Xu, J. Yang, and S. Guha, Mat. Res. Soc. Symp. Proc. **297**, 815 (1993).

22. Q. Wang, H. Antoniadis, E. A. Schiff, and S. Guha, Mat. Res. Soc. Symp. Proc. **258**, 881 (1992).

23. W. B. Jackson and N. M. Amer, Phys. Rev. B **25**, 5559 (1982); M. Vanecek, J. Kocka, J. Stuchlik, Z. Kozisek, O. Stika, and A. Triska, Sol. Energy Mat. **8**, 411 (1983).

24. X. R. Li, S. Wagner, and M. Bennett, Mat. Res. Soc. Symp. Proc. **258**, 899 (1992).

25. See, for example, N. W. Wang, X. Xu, and S. Wagner, in Ref. 7, p. 186.

26. S. Guha, J. S. Payson, S. C. Agarwal, and S. R. Ovshinsky, J. Non-cryst. Solids **97 & 98**, 1455 (1987).

27. K. Tanaka and A. Matsuda, Mat. Sci. Report **2**, 139 (1987).

28. D.A. Doughty, J.R. Doyle, G.H. Lin, and A. Gallagher, J. Appl. Phys. **67**, 6220 (1990).

29. S. Guha, K.L. Narasimhan, and S.M. Pietruszko, J. Appl. Phys. **52**, 859 (1981).

30. X. Xu, J. Yang, and S. Guha, Proc. of 23rd IEEE Photovoltaic Specialists Conference, 971 (1993).

31. S. Guha, J. Yang, A. Banerjee, T. Glatfelter, K. Hoffman, and X. Xu, PVSEC-7, 43 (1993).

32. X. Xu, J. Yang, and S. Guha, Appl. Phys. Lett. **62**, 1399 (1993).

33. X. Xu, J. Yang, and S. Guha, Mat. Res. Soc. Symp. Proc. **297**, 649 (1993).

34. S. Guha, J. Yang, P. Nath, and M. Hack, Appl. Phys. Lett. **49**, 218 (1986).

35. J. Yang, R. Ross, T. Glatfelter, R. Mohr, and S. Guha, Mat. Res. Soc. Symp. Proc. **149**, 435 (1989).

36. S. Guha, J. Yang, A. Pawlikiewicz, T. Glatfelter, R. Ross, and S. R. Ovshinsky, Appl. Phys. Lett. **54**, 2330 (1989).

37. S. Guha, J. Yang, A. Banerjee, T. Glatfelter, K. Hoffman, S. R. Ovshinsky, M. Izu, H. C. Ovshinsky, and X. Deng, Mat. Res. Soc. Symp. Proc. (San Francisco, April 1994).

38. A. Banerjee, J. Yang, T. Glatfelter, K. Hoffman, and S. Guha. Appl. Phys. Lett. **64**, 1517 (1994).

39. A. Banerjee, Solar Energy Materials and Solar Cells (in press).

40. A. Banerjee, E. Chen, R. Clough, T. Glatfelter, S. Guha, G. Hammond, K. Hoffman, M. Hopson, N. Jackett, M. Lycette, J. Noch, T. Palmer, K. Parker, I. Rosenstein, D. Wolf, X. Xu, J. Yang, and K. Younan, Proc. of 23rd IEEE Photovoltaic Specialists Conference, 795 (1993).

41. S. Guha, J. Yang, A. Banerjee, T. Glatfelter, and X. Xu, AIP Conf. Proc. **268**, 64 (1992).